Alma Mater Studiorum
Università di Bologna

Dottorato di Ricerca in Fisica
Ciclo XXV

Settore Concorsuale di afferenza: 02/A1
Settore Scientifico disciplinare: FIS/04

MEASUREMENT OF THE ZZ PRODUCTION CROSS SECTION AND LIMITS ON ANOMALOUS NEUTRAL TRIPLE GAUGE COUPLINGS WITH ATLAS

Presentata da: Alberto Mengarelli

Coordinatore Dottorato:
Prof. Fabio Ortolani

Relatore:
Prof. Antonio Zoccoli

Correlatore:
Dott. Benedetto Giacobbe

Esame Finale - Anno 2013

Contents

List of Figures

List of Tables

Introduction

The *Standard Model of Particle Physics* (SM) constitutes the most successful achievement in modern physics. In addition, the reliability of the SM theory is reinforced by the recent observation at LHC of a new particle with the feature of the predicted Higgs boson. This particle was, in fact, the last missing building block of the whole framework. As a consequence, the attention of the particle physicists in the last ~ 40 years has been focused on Higgs search and on performing high precision tests of the SM sectors where new physics can be hidden.

In the recent studies, processes involving the electroweak sector of the SM have received much attention as a strong test of the model by the fact that these interactions are intimately related to the gauge group of the model. Among them, Z-boson pair production cross section measurement has a particular importance since it plays a crucial role also in the Higgs boson study. In fact, ZZ dacaying in the four charged leptons channel ($ZZ \to \ell^- \ell^+ \ell^- \ell^+$) is an irriducible background that sorrounds the emergence of the Higgs boson events.

The extraordinary performances reached by the Large Hadron Collider (LHC) in terms of integrated luminosity and center of mass energy in the two early years of running, made possibile accurate study of rare processes such as $ZZ \to \ell^- \ell^+ \ell^- \ell^+$ with a precision superseding and improving the previous LEP and Tevatron results.

The main core of this thesis concerns the measurement of the $ZZ \to \ell^- \ell^+ \ell^- \ell^+$ production cross section using LHC 2011 data collected at $\sqrt{s} = 7$ TeV by the ATLAS detector and resulting in a total integrated luminosity of 4.6 fb^{-1}. The ZZ selection criteria, the reconstruction and identification efficiencies of leptons and the expected signal kinematic are presented together with cross section measurements in different phase space regions. The background data-driven estimate procedure is also discussed. The total cross section is finally compared with the NLO prediction calculated with modern Monte Carlo generators.

In order to give more detailed comparison of theory to measurement, allowing a generic comparison of the kinematic distributions to new theories, an "Unfolding" procedure is also applied. The three differential distributions ($\Delta\phi(l,l), p_T^Z$ and M_{4l}) are shown unfolded back to the underlying distributions using a Bayesian iterative algorithm.

Another foundamental aspect carried by interactions involving pair of Z bosons, is the sensitivity to anoumalus triple gauge couplings (nTGC). In particular, since a direct coupling of three neutrally charged gouge bosons is forbidden in the SM, a deviation of sensitive parameters from the SM prediction would provide important information about new physics beyond it. In this contest, the transverse momentum of the leading Z is used to provide limits on nTGC as discussed in the final chapter of this thesis.

Chapter 1

The Standard Model of Particle Physics

1.1 Introduction

The idea that matter is composed of few elementary building blocks is very ancient in the human history and it is still today a baseline guide in the world of particle physics. During the last sixty years, the discovery of the huge amount of particles in the various scattering experiments, forced physicists in making a big effort to formulate a model in which the large number of particles could be explained as combinations of a (relatively) small number of fundamental particles. This model is currently known as the *Standard Model of Particle Physics*. In the Standard Model (SM) the fundamental constituents of matter are *quarks* and *leptons* with the masses reported in Tab. 1.1, that interact via the exchange of *gauge bosons* in Tab. 1.2.

Generation	Leptons		Quarks	
1	e	ν_e	u	d
	(0.511 MeV)		($\sim$ 2 MeV)	($\sim$ 2 MeV)
2	μ	ν_μ	c	s
	(106 MeV)		(1205 MeV)	(95 MeV)
3	τ	ν_τ	t	b
	(1777 MeV)		(172 GeV)	(4.5 GeV)

Table 1.1: The basic fermions of the Standard Model included approximate observed masses [1]. The neutrinos ν_e , ν_μ and ν_τ are per construction massless in the Standard Model.

Mediator	Interaction	Coupling Strenght
γ	Electromagnetic	$\alpha = e^2/4\pi \simeq 1/137$
$W^{\pm}, Z$	Weak	$G_F \simeq 1.16 \times 10^{-5} \ \text{GeV}^{-2}$
gluon	Strong	$\alpha_s = g_s^2/4\pi \simeq 0.1$

Table 1.2: The Standard Model gauge boson propagators within rispective interaction and coupling strenght.

Since the SM is a quantum field theory an appropriate formalism must be introduced to construct the Lagrangian operator that discribes the particles and the interactions among them. A complete discussion can be found in [2], [3] and [4].

The starting point to build the complex mathematical framework of the SM is the Noether theorem [5] that establishes relation between symmetries and conservation laws. In particular, for every continuous symmetry transformation which leaves the Lagrangian invariant, there's a corresponding divergenceless Noether's current and, therefore, a conserved charge. The selection rules observed in nature, where there exist several conserved quantities (energy, momentum, electric charge...) correspond to dynamical symmetries of the Lagrangian. A special class of internal symmetries, called *gauge*-symmetries, occur when the physical system described by a certain lagrangian is invariant under a *local* phase transformation. Theories that satisfy gauge-symmetries are called gauge theories.

The SM is a gauge theory, based on the symmetry group $SU(3)_C \otimes SU(2)_L \otimes U(1)_Y$, which describes strong, weak and electromagnetic interactions, via the exchange of the corresponding spin–1 gauge fields: 8 massless gluons and 1 massless photon for the strong and electromagnetic interactions, respectively, and 3 massive bosons, $W^{\pm}$ and Z, for the weak interaction. The gauge symmetry is broken by the vacuum, which triggers the Spontaneous Symmetry Breaking (SSB) of the electroweak group to the electromagnetic subgroup:

$$SU(3)_C \otimes SU(2)_L \otimes U(1)_Y \quad \xrightarrow{\text{SSB}} \quad SU(3)_C \otimes U(1)_{\text{QED}} \,. \tag{1.1}$$

The SSB mechanism generates the masses of the weak gauge bosons, and gives rise to the appearance of a physical scalar particle in the model, the so-called "Higgs". The fermion masses and mixings are also generated through the SSB.

The SM constitutes one of the most successful achievements in modern physics. It provides a very elegant theoretical framework, which is able to describe the known experimental facts in particle physics with high precision.

1.2 Quantum Electrodynamics

Quantum Electrodynamics (QED) was the first of modern quantum theories and the most theoretically and experimentally studied of the SM. It derives from the free Dirac Lagrangian imposing the U(1) space time dependent phase tranformation. Considering the Lagrangian describing a free Dirac fermion $\psi(x)$ with mass m:

$$\mathcal{L}_0 = i\,\overline{\psi}(x)\gamma^\mu \partial_\mu \psi(x) - m\,\overline{\psi}(x)\psi(x)\,. \tag{1.2}$$

The *local* $U(1)$ phase invariance ("Gauge Principle") is only possible if one introduces a new spin-1 (since $\partial_\mu\theta$ has a Lorentz index) field $A_\mu(x)$, transforming as

$$A_\mu(x) \quad \xrightarrow{\text{U(1)}} \quad A'_\mu(x) \equiv A_\mu(x) + \frac{1}{e}\,\partial_\mu\theta\,, \tag{1.3}$$

and defines the covariant derivative

$$D_\mu\psi(x) \equiv [\partial_\mu - ieQA_\mu(x)]\,\psi(x)\,. \tag{1.4}$$

This modification is completely fixed and leads to the total Lagrangian of the QED, $\mathcal{L}_{\text{QED}}$:

$$\mathcal{L}_{\text{QED}} \equiv -\frac{1}{4}\,F_{\mu\nu}(x)\,F^{\mu\nu}(x) + i\,\overline{\psi}(x)\gamma^\mu D_\mu\psi(x) - m\,\overline{\psi}(x)\psi(x)\,, \tag{1.5}$$

where $F_{\mu\nu} \equiv \partial_\mu A_\nu - \partial_\nu A_\mu$ is the usual electromagnetic field strength.

A possible mass term for the gauge field, $\mathcal{L}_m = \frac{1}{2}m^2 A^\mu A_\mu$, is forbidden because it would violate gauge invariance, thus the photon is predicted to be massless. From experiments, $m_\gamma < 6 \cdot 10^{-17}$ eV [1], in agreement with the above theoretical prediction.

1.3 Quantum Chromodynamics

Quantum chromodynamics (QCD) is the theory of strong interactions describing the dynamics of quarks and gluons. Quarks were first introduced by Gell-Mann and Zweig in 1964 to explain the spectroscopy of hadrons. The quarks were establiished as the fundamental constituents of hadrons in the development of the quark model in '60s and '70s and assuming that mesons are $q\bar{q}$ states while baryons are qqq one can nicely classify all the known hadronic particles.

QCD is a non-Abelian [1] gauge theory of $SU(3)$ colour symmetry, described as $SU(3)_C$, which is invariant under $SU(3)$ transformation in colour space. The $SU(3)_C$ symmetry is unbroken as well as the $U(1)$ symmetry in QED, therefore,

---

[1] a non-Abelian group is a non commutative group.

just like the photons, gluons as gauge bosons mediating strong interactions ar also massless.

Since there exist no coloured hadrons in Nature, one should assume that all observed hadrons must be colourless, i.e. singlets under rotation in colour space. This assumption is known as *quark confinement*, because it implies the impossibility to observe free quarks: since these fundamental particles carry colour they are confined inside hadrons.

1.3.1 Evidence of Colours

There are several evidences that the colour degree of freedom is actually in 3 species (red, green and blue). A direct test on the colour quantum number can be obtained from the experimental data on e^+e^- annihilations at high energies, looking at the ratio

$$R_{e^+e^-} \equiv \frac{\sigma(e^+e^- \to \text{hadrons})}{\sigma(e^+e^- \to \mu^+\mu^-)}, \tag{1.6}$$

which at energies well below the Z peak, where the cross-section is dominated by the γ–exchange amplitude, is given by the sum of the contributing quark electric charges squared:

$$R_{e^+e^-} \approx N_C \sum_{f=1}^{N_f} Q_f^2 = \begin{cases} \frac{2}{3}N_C = 2, & (N_f = 3 \,:\, u,d,s) \\ \frac{10}{9}N_C = \frac{10}{3}, & (N_f = 4 \,:\, u,d,s,c) \\ \frac{11}{9}N_C = \frac{11}{3}, & (N_f = 5 \,:\, u,d,s,c,b) \end{cases}. \tag{1.7}$$

The values in the (1.7), obtained for a number of colours $N_C = 3$, are well in agreement with experimental measurements.

1.3.2 The QCD Lagrangian

Following the same steps of the QED case and adopting the vector notation in colour space $q_f^T \equiv (q_f^1, q_f^2, q_f^3)$, the free QCD Lagrangian can be written:

$$\mathcal{L}_0 = \sum_f \bar{q}_f \left(i\gamma^\mu \partial_\mu - m_f \right) q_f \tag{1.8}$$

invariant under arbitrary global $SU(3)_C$ transformations in colour space.

To satisfy that the Lagrangian in Eq. 1.8 is also invariant under *local $SU(3)_C$* transformations, covariant objects and gauge fields are needed. This leads to the total QCD Lagrangian:

$$\mathcal{L}_{\text{QCD}} \equiv -\frac{1}{4} G_a^{\mu\nu} G_{\mu\nu}^a + \sum_f \bar{q}_f \left(i\gamma^\mu D_\mu - m_f \right) q_f. \tag{1.9}$$

with

$$D^\mu q_f \equiv \left[\partial^\mu - i g_s \frac{\lambda^a}{2} G_a^\mu(x) \right] q_f \equiv \left[\partial^\mu - i g_s G^\mu(x) \right] q_f , \qquad (1.10)$$

and

$$G_a^{\mu\nu}(x) \;\; = \;\; \partial^\mu G_a^\nu - \partial^\nu G_a^\mu + g_s f^{abc} G_b^\mu G_c^\nu. \qquad (1.11)$$

In the Lagrangian of Eq. 1.9 all interactions are given in terms of a single universal coupling g_s, which is called the *strong coupling constant*. In Eq. 1.10 λ^a are the generators of the $SU(3)_C$ group and G_a^μ are the eight gauge boson gluon fields. In Eq. 1.11 the upscripts a, b, c in the structure constants of the $SU(3)_C$ symmetry group f^{abc} take values from 1 to 8.

The presence in Eq. 1.11 of the terms $g_s f^{abc} G_b^\mu G_c^\nu$ gives rise to a new feature of QCD with respect to QED, i.e. the existence of self-interactions among the gauge fields. Due to this new self-interactions properties which do not appear in QED, like asymptotic freedom and confinement (see section 1.3.3), could be explained.

1.3.3   Asymptotic Freedom

As discussed before, gluons have self-interactions because of the non-Abelian nature of QCD. This nature produces a drastically different behavior of the running coupling constant $\alpha_s(Q^2) = g_s^2/4\pi$ from the QED case. In QED the charge of the electron appears smaller at large distances due to the screening by vacuum polarization. In QCD the screening effect exist as well, but due to the presence of the virtual gluon pairs the net effect on the couling constant is the opposite.

The running coupling constant $\alpha_s(Q^2)$ can be written:

$$\alpha_s(Q^2) = \frac{12\pi}{(33 - 2n_f) ln \frac{Q^2}{\Lambda_{QCD}^2}} \qquad (1.12)$$

where Λ_{QCD}^2 is a free parameter with mass dimension and n_f is the number of quark flavours. The behavior of the Eq. 1.12 is depicted in Fig. 1.1.

For large values of Q^2 much larger than Λ_{QCD}^2, the effective couplings between quarks and gluons becames small and the quarks and gluons behave as free particles (*asymptotic freedom*). On the other hand, for small Q^2 region like $Q^2 \simeq \Lambda_{QCD}^2$, the quark-gluons coupling becames large and they are confined in hadrons (*confinement*). Λ_{QCD}^2 is thus the scale which separates the world of confinament (hadrons) and asymptotic freedom (free quarks and gluons).
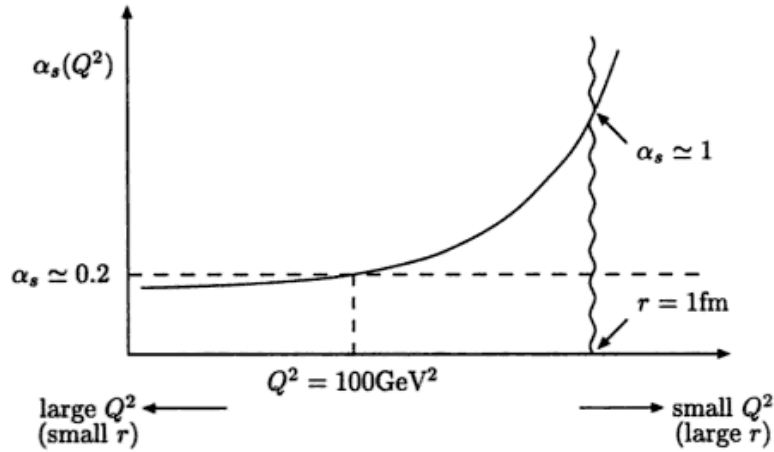
Figure 1.1: The running coupling α_s as a function of Q^2.

1.4   Electroweak Theory

The Glashow-Weinberg-Salam (GWS) model of electroweak interactions is a non-Abelian gauge theory with $SU(2)_L \otimes U(1)_Y$ gauge symmetry accompanied by the Higgs mechanism (see section 1.4.3). It's the first successful unification model in the theory of elementery particle interactions. The discovery of $W^{\pm}$ and Z bosons with expected masses and a weak neutral current mediated by a massive neutral vector boson Z is a great triumph of the model. Moreover, another possible succes of the SM theory is the recent discovery at LHC, made by the ATLAS and CMS collaborations, of a new particle in the search for the Standard Model Higgs boson [6], [7].

1.4.1   Experimental Introduction

The first hint on how to costruct the electroweak theory comes from the experiments that provided a large amount of informations about the dynamics underlying flavour-changing processes. The detailed analysis of the energy and angular distributions in β and pions decays:

$$\mu^- \rightarrow e^- \bar{\nu}_e \, \nu_\mu \tag{1.13}$$

$$n \rightarrow p \, e^- \bar{\nu}_e \tag{1.14}$$

$$\pi^- \rightarrow \mu^- \bar{\nu}_\mu \tag{1.15}$$

$$\pi^- \rightarrow e^- \bar{\nu}_e \tag{1.16}$$

clearly suggested that only the left-handed (right-handed) fermion (antifermion) chiralities participate in those weak transitions and that the strong interaction is universal. The existence of different neutrino types ($\nu_e \neq \nu_\mu$) and that there are separately conserved lepton quantum numbers which distinguish neutrinos from antineutrinos were also determined from experiments. All these experimental informations plus theoretical considerations related to unitarity determine the structure of the modern electroweak theory.

1.4.2   The $\mathbf{SU(2)_L \otimes U(1)_Y}$ Theory

Looking at how QED and QCD Lagrangians have been derived using gauge invariance also the electroweak model structure can be built in the same way. Of course, to describe weak interactions a more complex group of symmetry is nedeed. In fact, keeping in mind the experimental results previously discussed, in terms of $SU(2)$ representations this means that left-handed fermions should appear in doublets, while the right-handed parts are a weak iso-singlets. The structure of the first generation Standard Model fermions can be represented with the following notation. For quarks:

$$\psi_1(x) = \begin{pmatrix} u \\ d \end{pmatrix}_L, \qquad \psi_2(x) = u_R, \qquad \psi_3(x) = d_R. \qquad (1.17)$$

while for the lepton sector:

$$\psi_1(x) = \begin{pmatrix} \nu_e \\ e^- \end{pmatrix}_L, \qquad \psi_2(x) = \nu_{eR}, \qquad \psi_3(x) = e_R^-. \qquad (1.18)$$

We also need to have massive gauge bosons $W^\pm$ and Z in addition to the photon including the electromagnetic interactions in the model. The simplest group to consider is then

$$G \equiv SU(2)_L \otimes U(1)_Y, \qquad (1.19)$$

where L refers to left-handed fields and the subindex Y is the hypercharge. In electroweak theory the gauge bosons couple to fermions by means of hypercharge and weak isospin. Note that, the identification of $U(1)_Y$ with electromagnetism does not work. The assignment of quantum numbers like T_3 (third component of the weak isospin) and Y reported in Tab. 1.3 play an important role in defining electroweak structure. These two quantum numbers are related to the classical electric charge Q via the formula:

$$Q = T_3 + Y/2. \qquad (1.20)$$

The Glashow-Weinberg-Salam Lagrangian of the electroweak model can be divided

Quarks	T_3	Y	Leptons	T_3	Y
u_L	1/2	1/3	ν_e	1/2	-1
d_L	-1/2	1/3	e_L	-1/2	-1
u_R	0	4/3	e_R	0	-2
d_R	0	-2/3			

Table 1.3: $SU(2)_L \otimes U(1)_Y$ assignament of T_3 and Y quantum numbers.

into the following parts:

$$\mathcal{L}_{GWS} = \mathcal{L}_F + \mathcal{L}_G + \mathcal{L}_S + \mathcal{L}_Y \tag{1.21}$$

The first term $\mathcal{L}_F$ is built starting from the free Lagrangian as in QED and QCD

$$\mathcal{L}_0 \;=\; i\,\bar{u}(x)\,\gamma^\mu\,\partial_\mu u(x) \;+\; i\,\bar{d}(x)\,\gamma^\mu\,\partial_\mu d(x) \;=\; \sum_{j=1}^{3} i\,\overline{\psi}_j(x)\,\gamma^\mu\,\partial_\mu\psi_j(x)\,. \tag{1.22}$$

requiring the Lagrangian $\mathcal{L}_0$ to be invariant under local $SU(2)_L \otimes U(1)_Y$ gauge transformations.

In order to satisfy this symmetry requirement, we need to change the fermion derivatives by covariant objects. Since there are now 4 gauge parameters, 4 different gauge bosons are needed:

$$\begin{aligned}
D_\mu\psi_1(x) &\equiv \left[\partial_\mu - i\,g\,\widetilde{W}_\mu(x) - i\,g'\,y_1\,B_\mu(x)\right]\psi_1(x)\,, \\
D_\mu\psi_2(x) &\equiv \left[\partial_\mu - i\,g'\,y_2\,B_\mu(x)\right]\psi_2(x)\,, \\
D_\mu\psi_3(x) &\equiv \left[\partial_\mu - i\,g'\,y_3\,B_\mu(x)\right]\psi_3(x)\,.
\end{aligned} \tag{1.23}$$

where

$$\widetilde{W}_\mu(x) \equiv \frac{\sigma_i}{2}\,W_\mu^i(x) \tag{1.24}$$

denotes a $SU(2)_L$ matrix field. Thus, we have the correct number of gauge fields to describe the $W^\pm$, Z and γ.

The Lagrangian

$$\mathcal{L}_F \;=\; \sum_{j=1}^{3} i\,\overline{\psi}_j(x)\,\gamma^\mu\,D_\mu\psi_j(x)\,, \tag{1.25}$$

is invariant under local G transformations.

The gauge-invariant kinetic term for the gauge fields which should be added to $\mathcal{L}_F$ is given by:

$$\mathcal{L}_{\mathrm{G}} \;=\; -\frac{1}{4}\,W_{\mu\nu}^i\,W_i^{\mu\nu} \;-\; \frac{1}{4}\,B_{\mu\nu}\,B^{\mu\nu}\,. \tag{1.26}$$

with

$$W^i_{\mu\nu} = \partial_\mu W^i_\nu - \partial_\nu W^i_\mu + g\,\epsilon^{ijk}\,W^j_\mu\,W^k_\nu\,, \tag{1.27}$$

$$B_{\mu\nu} = \partial_\mu B_\nu - \partial_\nu B_\mu\,, \tag{1.28}$$

where $W^i_{\mu\nu}$ and $B_{\mu\nu}$ are field strenght tensors of gauge fields corresponding to $SU(2)_L$ and $U(1)_Y$, respectively.

Particularly interesting for the aim of this thesis is the field strengths $W^i_{\mu\nu}$ that contains the quadratic term $g\,\epsilon^{ijk}\,W^j_\mu\,W^k_\nu$. The Lagrangian $\mathcal{L}_G$ gives rise to cubic and quartic self-interactions among the gauge fields, i.e. the coupling between gauge bosons. In **Chapter 2**, starting from this part of the kinetic Lagrangian the anomalous Triple Gauge Couplings together with Diboson production at LHC will be theoretically discussed in detail.

The $SU(2)_L \otimes U(1)_Y$ Lagrangian in Equations 1.25 and 1.26 only contains massless fields. Due to local gauge invariance the mass terms of both gauge bosons and fermions can't appear. In order to make fermions and gauge bosons massive, as in the real world, the Higgs mechanism and the SSB of the gauge invariance is needed such as:

$$SU(2)_L \otimes U(1)_Y \rightarrow U(1)_{QED}. \tag{1.29}$$

To realize this symmetry breaking, the scalar fields which give rise to the Higgs mechanism, called Higgs bosons, are introduced. These can be translated in two additional Lagrangian terms ($\mathcal{L}_s$ and $\mathcal{L}_Y$) nedeed to complete the total $\mathcal{L}_{GWS}$ of the $SU(2)_L \otimes U(1)_Y$ electroweak model. In the next section (1.4.3) these two terms are derived together with SSB and Higgs mechanism discussion.

1.4.3   Spontaneus Symmetry Breaking and Higgs Mechanism

SSB occurs when the symmetry of the chosen original Lagrangian has been broken by breaking the symmetry of the vacuum, in other words, we have SSB if the Lagrangian of the system is invariant under the a given transformation while the vacuum state is not. To understand how this can happen and its implication a first fundamental result called *Goldstone Theorem* must be taken into account. The theorem states that starting from a Lagrangian with a global symmetry and breaking the symmetry of the vacuum states by chosing one particular point among the degeneretes ones of these states "appears" a massless particle called Goldstone boson.

In a practical example, considering a potential function of the complex scalar field $\phi(x)$ (Fig. 1.2):

$$V(\phi) = \mu^2 \phi^\dagger \phi + h\left(\phi^\dagger \phi\right)^2. \tag{1.30}$$

To guarantee that the energy of the system remains bounded, h can assume only positive values, then the minimum of $V(\phi)$ depends only on the sign of μ. For $\mu^2 > 0$ the potential has only one minimum at $\phi = 0$, while for $\mu^2 < 0$ the solutions are the fields configurations satisfying:

$$|\phi_0| = \sqrt{\frac{-\mu^2}{2h}} \equiv \frac{v}{\sqrt{2}} > 0\,, \qquad\qquad V(\phi_0) = -\frac{h}{4}v^4\,. \qquad (1.31)$$
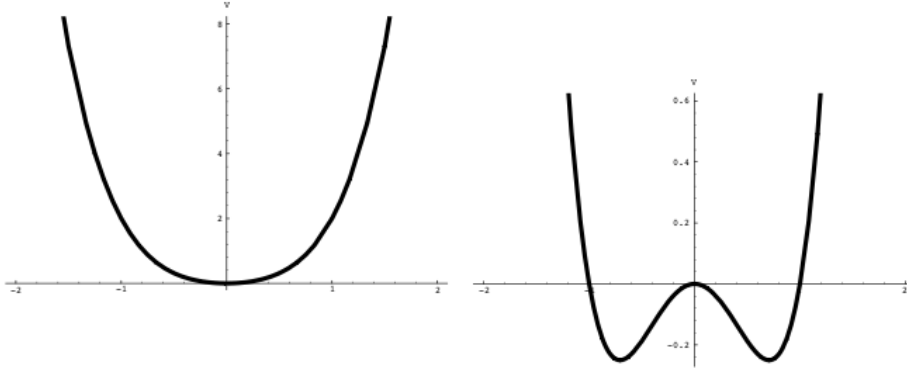
Figure 1.2: Shape of the scalar potential for $\mu^2 > 0$ (left) and $\mu^2 < 0$ (right).

Now considering an $SU(2)_L$ doublet of complex scalar fields and the potential in Eq. 1.30 is possible to construct the Lagrangian of the Goldstone model to give masses to the gauge bosons:

$$\mathcal{L}_S = (D_\mu\phi)^\dagger D^\mu\phi - \mu^2\phi^\dagger\phi - h\left(\phi^\dagger\phi\right)^2\,, \qquad\qquad (h > 0\,, \mu^2 < 0)\,, \quad (1.32)$$

where:

$$D^\mu\phi = \left[\partial^\mu - i\,g\,\widetilde{W}^\mu - i\,g'\,y_\phi\,B^\mu\right]\phi\,, \qquad\qquad y_\phi = Q_\phi - T_3 = \frac{1}{2}\,. \quad (1.33)$$

$\mathcal{L}_S$ is invariant under local $SU(2)_L \otimes U(1)_Y$ transformations. The potential is the same as in the previous example and associating the classical ground state with the quantum vacuum it satisfies:

$$\left|\langle 0|\phi^{(0)}|0\rangle\right| = \sqrt{\frac{-\mu^2}{2h}} \equiv \frac{v}{\sqrt{2}}\,. \qquad (1.34)$$

Choosing a particular ground state, the $SU(2)_L \otimes U(1)_Y$ symmetry gets spontaneously broken to the electromagnetic subgroup $U(1)_{\text{QED}}$ and by means of the

Goldstone theorem 3 massless states should then appear. These can be seen using a clever parametrization of the scalar doublet:

$$\phi(x) = \exp\left\{i\,\frac{\sigma_i}{2}\,\theta^i(x)\right\} \frac{1}{\sqrt{2}} \begin{pmatrix} 0 \\ v + H(x) \end{pmatrix}, \tag{1.35}$$

with 4 real fields $\theta^i(x)$ and $H(x)$. These 3 fields $\theta^i(x)$ are exactly the massless Goldstone bosons associated with the SSB mechanism.

At this stage choosing the physical (unitary) gauge $\theta^i(x) = 0$, the massless excitations of the ground state result unphysical and the Goldstone bosons disappear, so the kinetic piece of the scalar Lagrangian (1.32) takes the form:

$$(D_\mu\phi)^\dagger\,D^\mu\phi \overset{\theta^i=0}{\longrightarrow} \frac{1}{2}\,\partial_\mu H \partial^\mu H + (v + H)^2 \left\{\frac{g^2}{4}\,W^\dagger_\mu W^\mu + \frac{g^2}{8\cos^2\theta_W}\,Z_\mu Z^\mu\right\}. \tag{1.36}$$

The vacuum expectation value of the neutral scalar has generated a quadratic term for the $W^\pm$ and the Z, i.e. those gauge bosons have acquired masses:

$$M_Z\cos\theta_W = M_W = \frac{1}{2}\,v\,g. \tag{1.37}$$

In summary by extending the symmetry of the Lagrangian from the global to local one the 3 massless Goldstone bosons generated by the occurrance of SSB disapear and going to the unitary gauge the $W^\pm$ and the Z (but not the γ, because $U(1)_{\text{QED}}$ is an unbroken symmetry) have acquired masses, related as in Eq. 1.37.

The same argument for generating gauge bosons masses can be used in the fermionic case. So, the last piece of the total Lagrangian $\mathcal{L}_{GWS}$ in the unitary gauge (after SSB), takes the form:

$$\mathcal{L}_Y = \frac{1}{\sqrt{2}}\,(v + H)\,\left\{c_1\,\bar{d}d + c_2\,\bar{u}u + c_3\,\bar{e}e\right\}. \tag{1.38}$$

The SSB mechanism generates fermion masses:

$$m_d = -c_1\,\frac{v}{\sqrt{2}}, \qquad m_u = -c_2\,\frac{v}{\sqrt{2}}, \qquad m_e = -c_3\,\frac{v}{\sqrt{2}}. \tag{1.39}$$

The values of the fermion masses are arbitrary due to the fact that the parameters c_i are not known. Note, however, that all Yukawa couplings are fixed in terms of the masses:

$$\mathcal{L}_Y = -\left(1 + \frac{H}{v}\right)\,\left\{m_d\,\bar{d}d + m_u\,\bar{u}u + m_e\,\bar{e}e\right\}. \tag{1.40}$$

1.4.4 Predictions of the Electroweak Theory

The theoretical framework constructed above implies the existence of massive intermediate gauge bosons, $W^{\pm}$ and Z related among them via the vacuum expectation value of the scalar field as expressed in Eq. 1.37.

On the other hand the model cannot predict the values of the energy scale v and of the fermion masses (Tab. 1.1) which must be extracted from experiments. A direct determination of electroweak energy scale is given by the formula:

$$v = \left(\sqrt{2}\, G_F \right)^{-1/2} = 246 \,\text{GeV} \,. \tag{1.41}$$

where a precise existimation of the Fermi coupling constant G_F:

$$G_F = (1.16637 \pm 0.00001) \cdot 10^{-5} \,\text{GeV}^{-2} \,. \tag{1.42}$$

comes from the measurement of the muon lifetime.

Thus, using Equations 1.41 and 1.37 M_Z is predicted to be bigger than M_W in agreement with the measured masses:

$$M_Z = 91.1875 \pm 0.0021 \,\text{GeV} \,, \qquad M_W = 80.425 \pm 0.034 \,\text{GeV} \,. \tag{1.43}$$

From these experimental numbers, one obtains the electroweak mixing angle

$$\sin^2 \theta_W = 1 - \frac{M_W^2}{M_Z^2} = 0.222 \,. \tag{1.44}$$

An independent estimate of $\sin^2 \theta_W$ comes again from the decay $\mu^- \to e^- \bar{\nu}_e \, \nu_\mu$. This method leads to a values of

$$\sin^2 \theta_W = 0.215 \,, \tag{1.45}$$

in very good agreement with Eq. 1.44.

1.5 The Higgs Boson

Before ending this chapter, dedicated to a Standard Model review, a more detailed discussion on the Higgs boson is presented in this section. From the theoretical point of view the scalar Lagrangian (1.32) has introduced a new scalar particle into the model: the Higgs H. This Lagrangian in terms of the physical fields (unitary gauge), $\mathcal{L}_S$ can be decomposed [2]:

$$\mathcal{L}_S = \frac{1}{4} h\, v^4 + \mathcal{L}_H + \mathcal{L}_{HG^2} \,, \tag{1.46}$$

where in the $\mathcal{L}_H$ term the Higgs mass is given by

$$M_H = \sqrt{-2\mu^2} = \sqrt{2h}\, v\,. \tag{1.47}$$

and the $\mathcal{L}_{HG^2}$ shows that Higgs interactions are always proportional to the mass (squared) of the coupled boson. All Higgs couplings are determined by M_H, M_W, M_Z and the vacuum expectation value v.
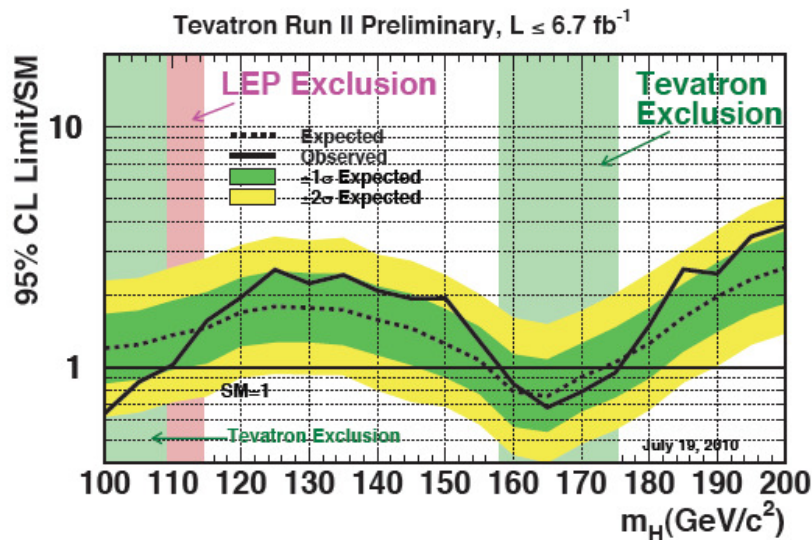
Figure 1.3: Combined LEP and Tevatron measurements on the exclusion mass range of the Higgs boson.

1.5.1   Experimental Limits on the Higgs Mass

After the introduction of the Higgs Mechanism on the elctroweak model, several experiments started to search the evidence of the Higgs boson in the various accelerator cunstructed all over the world. Before the LHC era all the experimental searches for the Higgs have only provided a lower bound on its mass, corresponding to the exclusion of the kinematical range accessible at LEP and the Tevatron [2] as shown in Fig. 1.3 wich tells:

$$M_H > 114.4 \quad \text{GeV} \qquad (95\% \text{C.L.}) \tag{1.48}$$

$$M_H < 158;\;\; M_H > 175 \quad \text{GeV} \qquad (95\% \text{C.L.}) \tag{1.49}$$

---

[2]Tevatron limits are the ones presented at ICHEP conference in '10 with a total integrated luminosity of $\simeq 7$ fb$^-1$

1.5.2   Higgs Search at LHC

The extraordinary performance of the LHC collider in center of mass energy and collected luminosity during 2011 and 2012, has given the possibility to the ATLAS collaboration (together with CMS collaboration) to claim the first observation of a new particle in the search for the Standard Model Higgs boson.
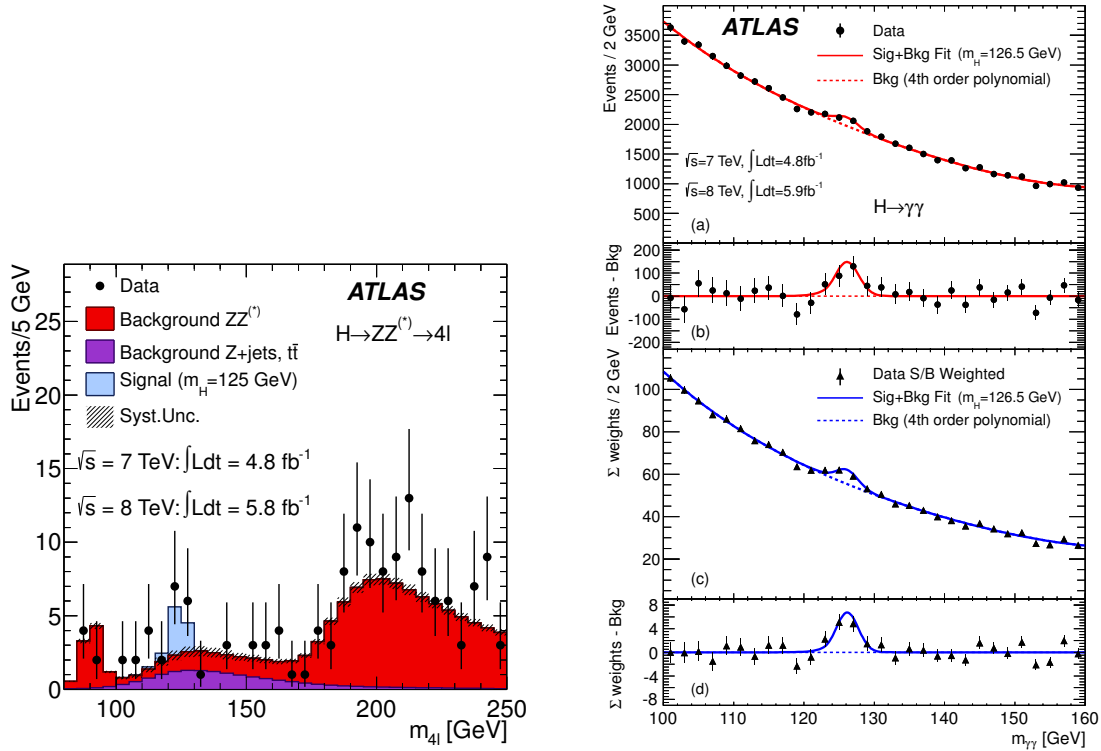
Figure 1.4: On the left, the distribution of the four-lepton invariant mass, m_{4l}, for the selected candidates, compared to the background expectation in the 80 to 250 GeV mass range, for the combination of the $\sqrt{s} = 7$ TeV and $\sqrt{s} = 8$ TeV data. The signal expectation for a SM Higgs with $m_H = 125$ GeV is also shown. On the right, the distributions of the invariant mass of diphoton candidates after all selections for the combined 7 TeV and 8 TeV data sample.

In Fig. 1.4 are reported the invariant mass distributions in the two main channels ($H \rightarrow ZZ^* \rightarrow l^+l^-l^+l^-$ and $H \rightarrow \gamma\gamma$) of the Higgs search as performed by the ATLAS detector. These results together with the one obtained in the $H \rightarrow WW^{(*)} \rightarrow l\nu l\nu$ dacay channel provide conclusive evidence for the discovery of a new particle with mass:

$$M_H = 126.0 \pm 0.4(stat) \pm 0.4(sys) \quad \text{GeV} \tag{1.50}$$

In the narrow region, 122-133 GeV the significance of the excess observed events is 5.9σ (Fig.1.5). Taking into account the entire mass region of the search, 110-600 GeV, the global significance of the excess is 5.1σ.
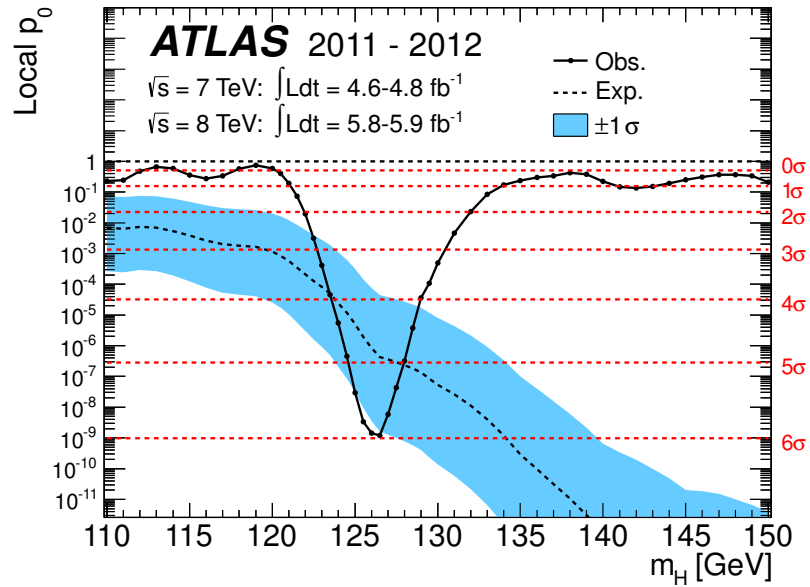
Figure 1.5: The observed (solid) local p0 as a function of m_H in the low mass range. The dashed curve shows the expected local p0 under the hypothesis of a SM Higgs boson signal at that mass with its plus/minus one sigma band. The horizontal dashed lines indicate the p-values corresponding to significances of 1 to 6 sigma.

Chapter 2

Diboson Physics and Anomalous Triple Gauge Couplings at LHC

2.1 Introduction

As presented in the previous chapter in section 1.4.4, the Standard Model (SM) of the electroweak theory makes precise predictions to study the gauge symmetry of the SM. In order to investigate more in depth the SM, gauge boson self-couplings have received much attention by the fact that these interactions are intimately related to the gauge group of the model, and a deviation from the SM would provide important information about the kind of new physics beyond it. In this chapter the attention is focused on the trilinear couplings ZZV (with $V = \gamma$ or Z) and on the discussion of the Z boson pair production at LHC collider.
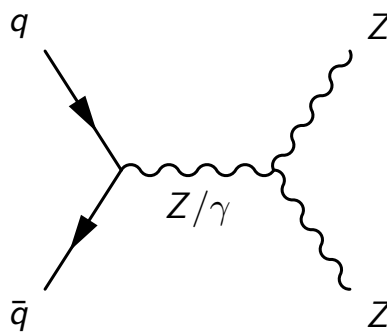
Figure 2.1: The ZZZ neutral TGC vertex forbidden by the SM.

2.2   Triple Gauge Coupling

In section 1.4.2 the electrowek Lagrangian is presented. The term $\mathcal{L}_G$ (Eq. 1.26) can be shown to generate self-interactions among the gauge bosons. It turns out that terms with gauge bosons of the same type are all zero. In other words the SM forbids, at tree level, the Z pair production via the triple gauge vertex shown in Fig. 2.1. So new physics beyond the SM can manifest itself if an anoumalous interaction between three neutral gauge bosons arises.

2.2.1   Effective Lagrangian of the Neutral Triple Gauge Couplings

The most general vertex of self-interacting gauge bosons is shown in Fig. 2.2 where q_1, q_2 and p are the momenta of the two on-shell Z bosons and the s-channel propagator respectively.
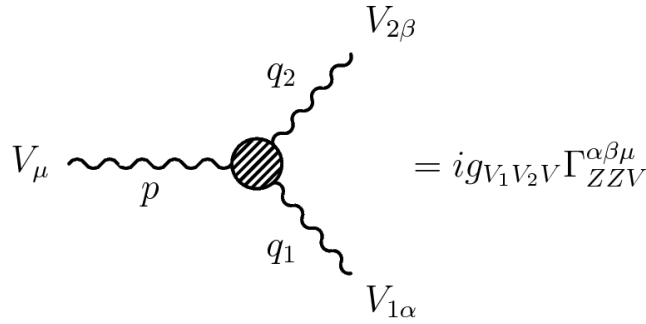
Figure 2.2: Feynman rule for the ZZV vertex.

The effective Lagrangian generating the vertex in Fig. 2.2 is

$$L = \frac{e}{M_Z^2}[f_4^V(\partial_\mu V^{\mu\beta})Z_\alpha(\partial^\alpha Z_\beta) + f_5^V(\partial^\sigma V_{\sigma\mu})\tilde{Z}^{\mu\beta}Z_\beta], \qquad (2.1)$$

where $V_{\mu\nu} = \partial_\mu V_\nu - \partial_\nu V_\mu$ and $\tilde{Z}^{\mu\beta} = \frac{1}{2}\epsilon_{\mu\nu\rho\sigma}Z^{\rho\sigma}$. The couplings f_i^V ($i = 4, 5$) are dimensionless complex functions of q_1^2, q_2^2, p^2 and zero at tree level. All couplings violate charge conjugation C, the terms f_4^V are CP violating while f_5^V terms are CP conserving.

The parton level diboson production cross sections with anomalous couplings grow with the parton center of mass energy $\sqrt{s}$. In order to avoid unphysical results that would violate unitarity, the center of mass energy dependence is taken into account introducing the following form factor parameterization of the coupling

parameters f_i^V:

$$f_i^V(s) = \frac{f_{i0}^V}{(1 + s/\Lambda_{FF}^2)^n} \qquad (i = 4, 5), \qquad (2.2)$$

where Λ_{FF} is the energy scale which is related to the scale of the new physics generating the anomalous ZZV couplings. This kind of form factor ensures that the couplings vanish at high center of mass energy.

In Eq. 2.2 the values of f_{i0}^V and the power n of the form factor at low energy are constrained by partial wave unitarity of the inelastic ZZ production amplitude in fermion-antifermion annihilation at arbitrary center of mass energy.

Selecting an exponent well above the minimum value $3/2$, as shown in [8], ensures that the ZZ differential cross section stay well below unitarity limit at energies $\sqrt{s} >> \Lambda_{FF} >> M_Z$.

A common choice adopted for LHC case and that will be used in this thesis to derive limits in **Chapter 7** is $n = 3$ and $\Lambda_{FF} = 2$ TeV [9].

2.2.2 Anomalous Neutral Triple Gauge Couplings (nTGC)

As already mentioned in the previous section, the two couplings f_i^V $(i = 4, 5)$ contribution are zero at tree-level. The simplest Standard Model method for generating them is considering a virtual one-loop effect of heavy fermions. Fig. 2.3 illustrates this diagram which is normally called the fermionic triangle. The SM
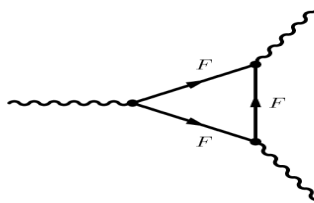
Figure 2.3: One-loop fermionic triangle vertex.

prediction of these contribution are expected to be of the order of 10^{-4} [8].

There are many models beyond the SM that ganerates non zero nTGC. One example is the Miminally Supersimmetric Standard Model (MSSM) which is able to generate the triangle diagram in Fig. 2.3 where the heavy fermions are charginos and neutralinos. Charginos will contribute to $f_5^{Z,\gamma}$, while the neutralinos to f_5^Z only. The total contribution to nTGC in MSSM is expected to be of the same order of magnitude of the one predicted for the SM (10^{-4}).

2.3   ZZ production at LHC

The production of pairs of Z bosons at the Large Hadron Collider (LHC) and in general at hadron colliders proceeds at tree level via the $q\bar{q} \to ZZ$ Fynman diagrams in Fig. 2.4, with the possible non SM contribution of the diagram in Fig. 2.1 previously discussed. Another contribution comes from $gg \to ZZ$ via the quark box diagrams in Fig. 2.5. Possible deviations from SM expectations for the total or differential ZZ production cross sections could be indicative of the production of new resonances decaying to Z bosons or other non-SM contributions such as anomalous neutral triple gauge couplings (nTGC). To perform high precision measurements of this kind, modern tool called Monte Carlo generators are available to calculate SM prediction of the sensitive parameters to test in high energy experiments.

(a) $t-$channel ZZ production.   (b) $t-$channel ZZ production.
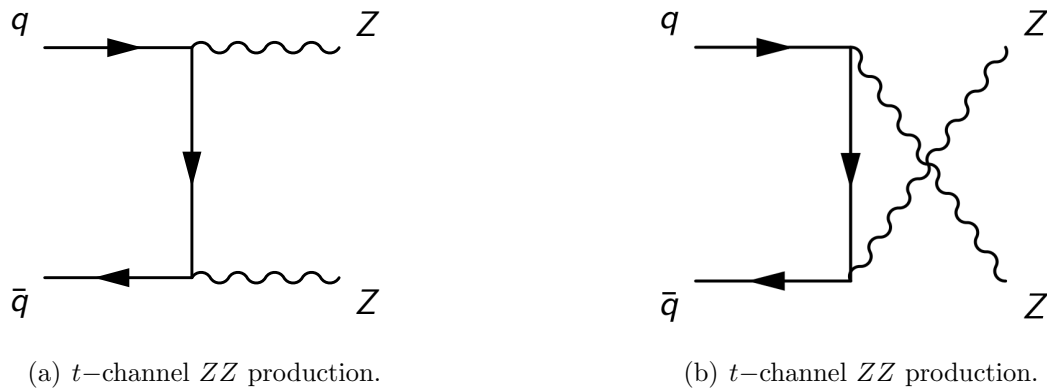
Figure 2.4: The SM tree-level Feynman diagrams for ZZ production through the $q\bar{q}$ initial state in hadron colliders.
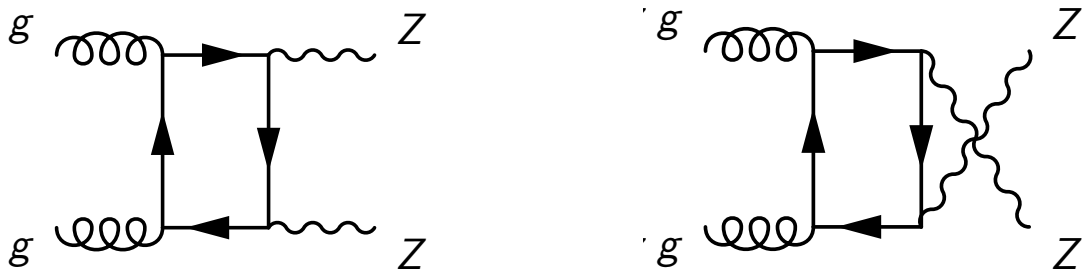
Figure 2.5: Feynman diagrams for $gg \to ZZ$ production.

2.3.1 Monte Carlo Event Generators

Monte Carlo (MC) event generators are needed to make theoretical predictions for high-energy reactions. In modern colliders, such as LHC, primary reactions involve hadrons. In the initial state hadrons are the colliding particles and in the final state they are used to define observables of interest.

Due to the asymptotic freedom of QCD discribed in section 1.3.3, the interaction of partons can be calculated using perturbation theory if the scattering process involves large invariant momentum transfer and correspondingly short time scales.

This make possible to evaluate the cross section for the production of an X-particle final state using the decomposition:

$$\sigma_X = \Sigma_{a,b} \int_0^1 dx_1 dx_2 f_a(x_1, \mu_F^2) f_b(x_2, \mu_F^2) \times \sigma_{ab \to X}(x_1, x_2, \alpha_S(\mu_R^2), Q^2/\mu_F^2, Q^2/\mu_R^2)$$

(2.3)

where $f_{a,b}(x_{1,2}, \mu_F^2)$ are parton distribution functions (PDF) and $\sigma_{ab \to X}$ is the parton-level cross section. Q^2 is the energy of the process while μ_F^2 and μ_R^2 are the factorization and renormalization scales respectively. To compute the cross section in Eq. 2.3 two ingredients are necessary:

1. Parton-level cross section: (from theory)

2. PDF: (fit from experiments, but evolution from theory)

The parton-level cross section can be computed as a series in perturbation theory, using the coupling constant as an expansion parameter:

$$\sigma_{ab \to X} = \sigma_0 + \alpha_S \sigma_1 + ...$$

(2.4)

By calculating the short distance coefficient (Eq. 2.4) at tree-level ($\sigma_{ab \to X} = \sigma_0$) is possible to obtain the first estimate (leading-order LO) of rates for inclusive final states. Even if at this order, extra radiation is included, a LO cross section can strongly depend on the factorization and renormalization scales. A first reliable estimate of the total cross section can be calculated using a next-to-leading order approximation of Eq. 2.4, where a more accurate description of extra radiation is included and new effects coming up from higher order terms (e.g., opening up of new production channels or phase space dimensions) can be evaluated.

Due to their importance a separate section (see 2.3.2) is dedicated to PDF.

In the following, a list of the most common used MC generators is presented. For each generator the main focus is on the ZZ diboson process implementation in the simulation. Depending on the accuracy of the ZZ process description, each MC generator will be used with different scope in the main analysis presented in this thesis.

- **POWHEG BOX**:
  PowhegBox [11] is a next-to-leading order (NLO) MC generator including, for the ZZ diboson case leptonic decays, $Z(\gamma^*)$ interference and non-resonant graphs. It provides calculations without the Z mass at the zero-width approximation, so it is appropriate to model fiducial phase-spaces where at least one of the two Z is off-shell.
  It will be used as the baseline signal MC for the $ZZ \to \ell^-\ell^+\ell^-\ell^+$ selection presented in **Chapter 4**.

- **MC@NLO**:
  MC@NLO [12] is a package which combines a Monte Carlo event generator with NLO calculations for QCD processes. MC@NLO makes use of the HERWIG event generator [13] for the parton shower and hadronization/fragmentation processes, plus the JIMMY [14] package for the underlying event. In the analysis presented here, MC@NLO is used to model $t\bar{t}$ and single top background processes.

- **MCFM**:
  MCFM [15] is a parton-level Monte Carlo program which gives cross section predictions for a large number of processes at hadron colliders. In particular, it is able to calculate diboson production cross sections at LO and NLO in QCD perturbation expansion.
  MCFM provides NLO cross section prediction for the ZZ measurement presented in this thesis (see section 2.3.3).

- **SHERPA**:
  Sherpa [16] is a leading order event generator that includes initial state radation, parton showering and underlying event. SHERPA is also able to produce samples with anoumalus triple gauge couplings and will be used to extract limits on f_i^V ($i = 4, 5$) (see **Chapter 7**).

- **GG2ZZ**:
  The gg2zz [17] implements a complete calculation of gluon-induced loop processes $gg \to Z(\gamma^*)Z(\gamma^*) \to \ell^-\ell^+\ell^-\ell^+$. The contribution to ZZ production in pp collisions is not included in the NLO calculations of $q\bar{q}$-induced processes implemented in programs such as POWHEG and MC@NLO.

2.3.2   Parton Distribution Functions

In hadron-hadron collisions, such as the LHC case, proton compositeness has to be taken into account in cross-section calculations and predictions. Protons are composed, in first approximation, by two up quark and a single down quark, called valence quarks. In addition to the valence quarks, the virtual gluon and quark "*sea*" should be considered. In general the particles composing hadrons both from valence and *sea* are called partons. In the parton model, proposed by Feynman and devoloped by Byorken, the hadron is considered as an incoherent superposition of partons. The momentum fraction x carried by each parton with respect the whole hadron at a momentum transfer Q^2 is described by a probability density functions called, in the proton case, Parton Distribution Functions (PDF):

$$f(x)dx \equiv P(x \in [x, x + dx], Q) \qquad f = q, \bar{q}, g. \qquad (2.5)$$

Since the uncertainty on theoretical cross section calculation mostly arise from PDFs uncertainty, different set of PDFs are used to take into accont the experimental results. The most popular families of PDF are presented in the following:

- **CTEQ PDFs**:
  The CTEQ6.6 [18] is a NLO parton distribution, based on an implementation of the heavy-quark mass effect in perturbative QCD cross sections, with significant improvement with respect to the ordinary zero-mass scheme. The evolution equation from the low energy region to the high energy region is performed at NLO.
  The CTEQ6.6 PDFs have been recently superseded by the new CT10 [19] version. This new version includes in the fit : combined HERA-I Deep Inelastic Scattering (DIS) data, Tevatron inclusive jet production and Z-rapidity measurement.

- **MSTW2008**:
  MSTW2008 [20] PDFs provide fit at LO, NLO and NNLO. The fit includes a large amount of data from fixed-target experiments, HERA and Tevatron, starting from input parton distributions parametrised at $Q^2 = 1$ GeV. Several theoretical refinements and developments in the fitting procedure have been introduced, as treatment of heavy flavors in a general-mass variable flavor number scheme, extended input parameterization for strange quarks and gluon distributions and a new treatment of PDF uncertainties.

- **HERAPDF**:
  The HERAPDF1.0 set is based on the combination of published H1 and ZEUS measurements from HERA I on inclusive DIS in neutral (NC) and charged current (CC) reaction [21]. The PDF fit is performed at NLO using

a variable-flavour-number scheme and includes error PDF sets parametrizing experimental and model uncertainties.

- **ABKM09**:
  The ABKM09 PDF fit is performed at NLO and NNLO using a fixed-flavour-number scheme and is based on DIS measurements and fixed target Drell-Yan production [22].

2.3.3   ZZ Inclusive Cross Section Predictions

The first calculation including NLO corrections to the process, $q\bar{q} \to ZZ$, was presented in [23]. The spin correlations in the decays and phenomenology for the Tevatron and 14 TeV LHC was presented in [24]. Finally, contributions from a gluon-gluon initial state, $gg \to ZZ$, were first considered in [25]. The results presented in this section are obtained using the framework as reported in [26]. At next-to-leading order (NLO) in QCD, the total cross section for non-resonant ZZ production is predicted to be $6.18^{+0.25}_{-0.18}$ pb. In this calculation MCFM [15] with CT10 in the on-shell (zero-width) approximation is used. A 5.8% contribution from gluon fusion is also included. The more realistic case using the natural width of the Z boson, together with the requirement that both Z bosons are within the Z mass window (66-116 GeV), leads to the following NLO cross section prediction:

$$\sigma(ZZ) = 5.89^{+0.22}_{-0.18} \quad \text{pb}. \tag{2.6}$$

In the cross sections calculated above the renormalization (μ_R) and factorization (μ_F) scales are set equal to half the mass of the diboson system. The quoted theoretical uncertainties result from using the full CT10 parton distribution function error set and varying μ_R and μ_F scales simultaneously by a factor of two.

2.4   Previous Experimental Results from LEP, Tevatron and LHC

Z boson pair production was studied at LEP by the L3 [27], OPAL [28], ALEPH [29] and DELPHI [30] collaborations in multiple final states. The cross section was measured over a range across the threshold for ZZ production, as shown in Fig. 2.6. At an energy of $\sqrt{s} = 200$ GeV, the combined cross section is measured to be $\sigma(e^+e^- \rightarrow ZZ) = 0.90 \pm 0.12$ pb. LEP experiments have also set limits on anomalous ZZZ and $ZZ\gamma$ couplings.

Both Tevatron experiments DØ and CDF have also studied Z bosons pair production. The DØ analysis of $ZZ \rightarrow \ell^-\ell^+\ell'^-\ell'^+$ and $ZZ \rightarrow \ell^-\ell^+\nu\bar{\nu}$ lepton production with 6.4 fb^{-1} of data has yielded a measurement of $1.40^{+0.43}_{-0.37}$ (stat.) $\pm$ 0.14 (sys.) pb [31]. Additionally, limits on anomalous ZZZ and $ZZ\gamma^*$ couplings have also been derived [32]. The CDF experiment has used 1.9 fb^{-1} of data and in the combined $\ell^-\ell^+\ell'^-\ell'^+$ and $\ell^-\ell^+\nu\bar{\nu}$ channels measured a cross section of $\sigma(ZZ) = 1.4^{+0.7}_{-0.6}$ (stat. $+$ sys.) pb [33].
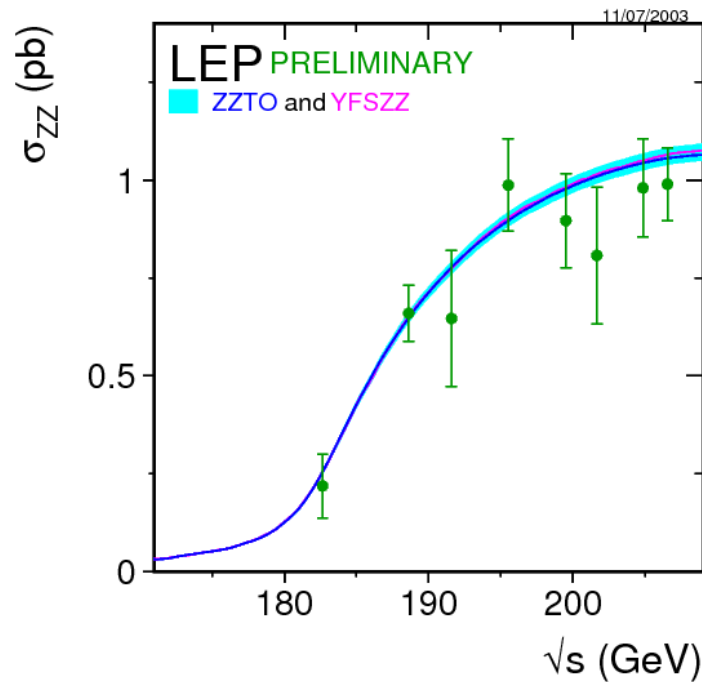
Figure 2.6: ZZ production cross section as a function of $\sqrt{s}$ measured at LEP.

Recently, ATLAS [34] and CMS [35] have released results on ZZ production, both experiments with the first 1 fb^{-1}of the 2011 data at $\sqrt{s} = 7$ TeV. AT-

LAS, with 1.02 fb^{-1}of data, measured a cross section of $8.5^{+2.7}_{-2.3}$ (stat)$^{+0.4}_{-0.3}$ (syst) $\pm$ 0.3 (lumi.) pb, consistent with the theoretical expectations. Using this cross section, limits on the nTGCs were derived and the improvement with respect to LEP and Tevatron measurements is shown in Fig. 2.7.
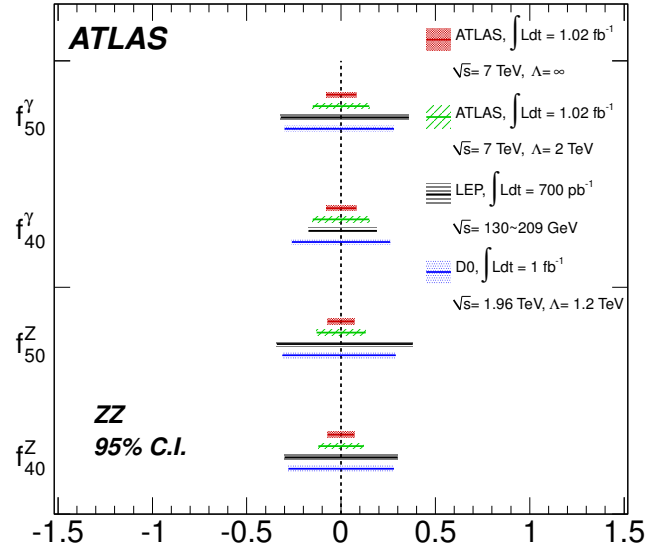
Figure 2.7: Anomalous nTGC 95% confidence intervals from ATLAS, LEP [36] and Tevatron [37] experiments. Integrated luminosities, centre-of-mass energy and cut-off Λ for each experiment are shown.

Chapter 3

The Large Hadron Collider and the ATLAS Experiment

3.1 Introduction

The Large Hadron Collider (LHC) [38] is a two-ring, superconducting accelerator and collider installed in the 27 km long *Large Electron-Positron (LEP)* [39] tunnel aiming to extend the frontiers of particle physics with its unprecedented high energy and luminosity. It is the largest particle accelerator in the world. It is located beneath the border of France and Switzerland, at a depth between 50 and 175 m below the surface. The next sections are dedicated to describe the design, performance and experiments of the LHC collider. Among these experiments, the ATLAS detector will be described in datail since it is the one used to collect the data analyzed in this thesis.

3.2 LHC Design and Performance

LHC has been designed to shed light on an energy region almost unexplored yet. Most of the design parameters are therefore close to the technical limits.

In the LHC tunnel two proton beams circulate in opposite directions and collide in four points. The design performance foresees an energy of 7 TeV for each beam, in order to obtain total center-of-mass energy of 14 TeV and a collison rate of 40 MHz. In 2010 and 2011 the energy was somewhat lower, 7 TeV, while in the 2012 the center-of-mass energy was rised up to 8 TeV. The maximum collision rate was 20 MHz, i.e. a collision every 50 ns. A total integrated luminosity of ~ 5 fb^{-1} and ~ 20 fb^{-1} has been delivered by LHC to the ATLAS experiment respectively in the 2011 and 2012 data taking periods. A peak instantanous luminosity of $L \sim 8 \cdot 10^{33} cm^{-2} s^{-1}$ has been reached in August 2012. In Fig. 3.1 is shown the
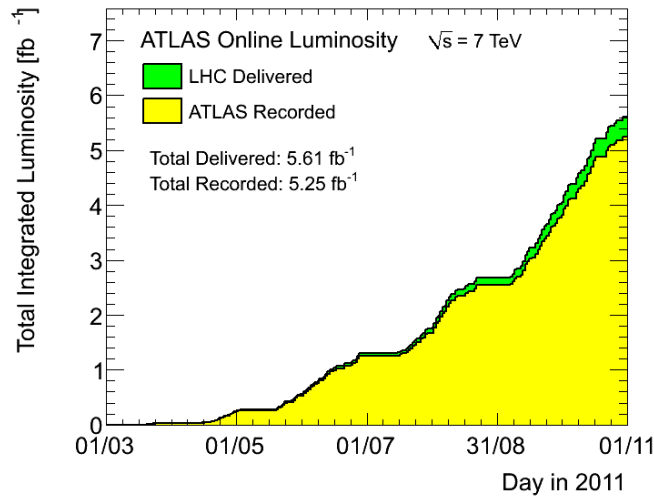
Figure 3.1: Total integrated luminosity delivered by LHC and recorded by ATLAS in 2011.

total integrated luminosity recorded by ATLAS in 2011 wich corresponds to the amount of data used for the analysis presented in this thesis.

In the LHC ring, the two beams circulate into two separate ultrahigh vacuum chambers at a pressure of 10^{-10} Torr. The beams are labelled 1 and 2, where the former circulates clockwise and the latter in the opposite direction. In order to keep the beams into circular trajectories, 1232 superconducting dipole magnets generate a magnetic field of 8.4 T at a current of 11.85 kA and a temperature of 1.9 K. Other 392 superconducting quadrupole magnets produce a field of 6.8 T necessary to focalize the beams. The fields strenght and currents above are predicted in the $\sqrt{s} = 14$ TeV running scenario.

The most important parameters of the LHC in the 7-8 TeV running conditions are reported in Tab. 3.1.

3.2.1   The Injection Chain

To reach the desired center-of-mass energy, protons are accelerated through a chain of accelerators as presented in Fig. 3.2.

- **Linac2**: It is a linear accelerator for protons and ions. It injects beams of 50 MeV in the following accelerator with a rate of 1 Hz. The duration of each pulse ranges from 20 μs to 150 μs depending on the number of required protons.

- **Proton Synchrotron Booster (PSB)**: It speeds up the beams coming

Parameters	Values
Maximum collision energy	8 TeV (2012)
Number of particles per bunch	$2.0 \cdot 10^{14}$
Number of fill bunches	1368
Bunch separation	50 ns
Bunch width (ATLAS)	16.7 μ m
Peak Luminosity	$7.78 \cdot 10^{33} cm^{-2} s^{-1}$
Inelastic pp cross section (ATLAS 7 TeV)	68 mb
	73 mb predicted at 8 TeV
Number of collision per bunch	$10 - 40$

Table 3.1: LHC main parameters.
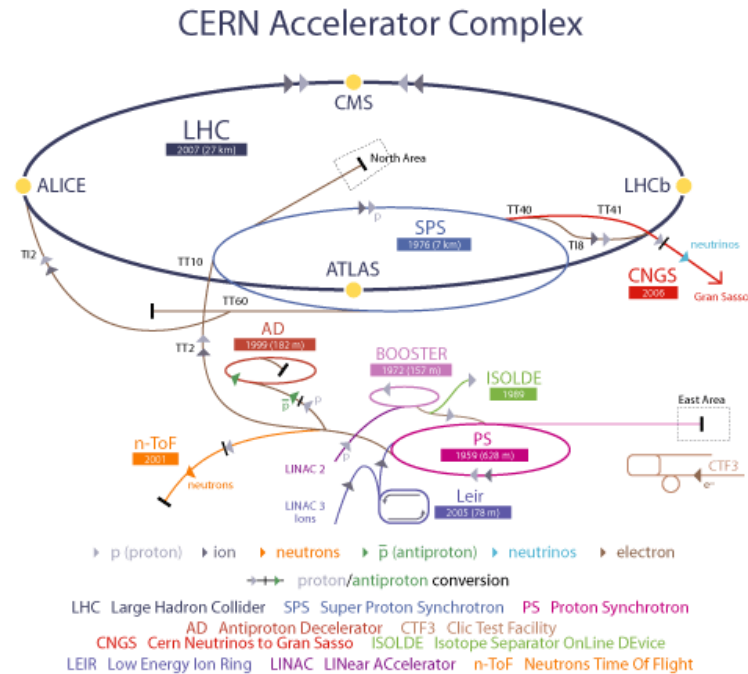
Figure 3.2: Scheme of injection chain at LHC.

from Linac2 to an energy of 1.4 GeV. The accelerator is composed of 4 superimposed rings. Five bunches circulate in each ring that are then focused and sent through a magnet deflector into a single line for injection into the next accelerating element.

- **Proton Synchrotron (PS)**: It accelerates protons up to an energy of 28 GeV. It can be set to separate the bunches by the needed time 50-25 ns.

- **Super Proton Synchrotron (SPS)**: It is used as final injector for protons and heavy ions bringing the energy from 28 GeV to 450 GeV.

After injection in the LHC ring at 450 GeV, protons are accelerated up to the energy of 7(8) TeV (for each circulating beam).

3.3   LHC Experiments
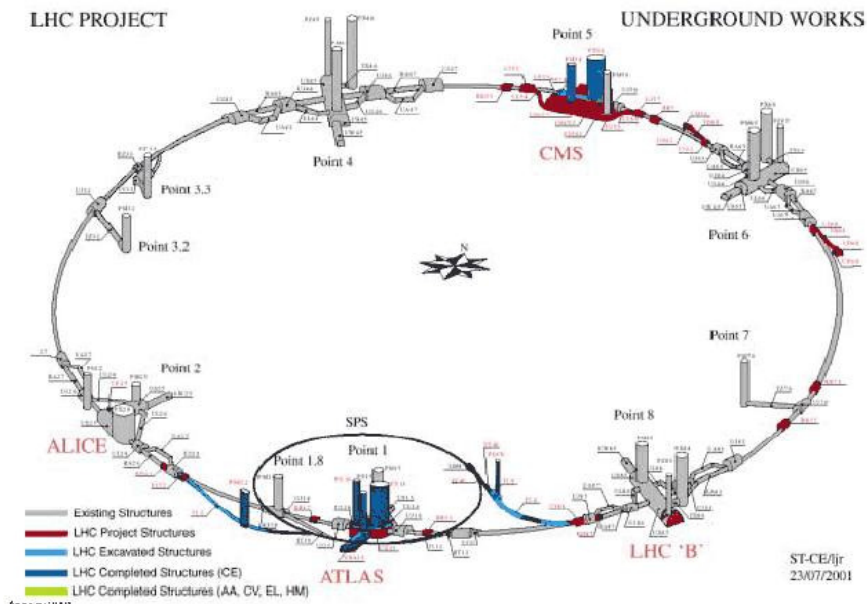
Figure 3.3: Position of the experiments along LHC ring.

Four experiments are installed along the LHC tunnel (see Fig. 3.3):

- **A Toroidal LHC ApparatuS (ATLAS)**: it is a multi-purpose experiment which works at high luminosity ($L = 10^{33-34}cm^{-2}s^{-1}$). Section 3.4 is fully dedicated to the apparatus description.

- **Compact Muon Solenoid (CMS)**: it is a multi-purpose experiment designed to work up to high luminosity with the same intents of ATLAS, but implemented with different technologies.

- **LHCb**: it performs accurate measurements in the flavour physics of the B mesons, for example CP violation. Since the production and the decay vertices of B-mesons are difficult to reconstruct when there is more than one interaction per bunch crossing, LHCb works at a luminosity lower than the

one designed for ATLAS and CMS (about $L = 10^{32} cm^{-2} s^{-1}$), using proton beams less focused near the interaction point.

- **A Large Ion Collider Experiment (ALICE)**: it is dedicated to the study of a condensed status of the matter, called *quark-gluon plasma*, by detecting particles that are produced in heavy ions collisions. Due to the high nucleus-nucleus cross section, the higher track density per collision and the technologies implemented by the detector, ALICE can work up to luminosities of $L = 10^{27} cm^{-2} s^{-1}$.

Other two experiments are installed along the tunnel:

- **LHCf**: it measures γ and π^0 spectra in the very forward region at luminosity of $L = 10^{29} cm^{-2} s^{-1}$. The aim is the calibration of Monte Carlo generators in cosmic rays studies. This detector was installed in 2009 and worked only during the data taking at 900 GeV.

- **Total Cross Section, Elastic Scattering and Diffraction Dissociation at the LHC (TOTEM)**: it is designed to measure the total *pp* cross section at a luminosity of $L = 10^{29} cm^{-2} s^{-1}$. It is installed along the beam pipe near CMS.

3.4 The ATLAS Detector at LHC

The ATLAS detector [40], [49], [50] is the largest one among the four main experiments located around the LHC ring. It's a general purpose apparatus that can provide a wide range of physics studies spanning from precision measurements of standard model parameters to the uncovering of phenomenon due to new physics such as the recent new "Higgs-like" particle observation [6].

The extreme LHC environement in terms of radiation doses and particle multiplicity, combined with the performance requirements for precision measurements sets new standards for the detector, which has to be met by employing a wide range of different techniques in each subsystem of the ATLAS experiment.

In the next sections the experimental design of the ATLAS experiment is presented.

3.4.1 ATLAS Detector Overview

The ATLAS detector, installed 100 m underground in the interaction Point 1 along the LHC tunnel, is nominally forward-backward symmetric with respect to the interaction point. The magnet configuration (see section 3.4.2) comprises a thin supercunducting solenoid surrounding the inner-detector cavity, and three large

superconducting toroids (one barrel and two end-caps) arranged with eight-fold azimuthal symmetry around the calorimeters. The inner detector (see section 3.4.3) is immersed in the 2 T solenoidal field and surrounded by the calorimeters (see section 3.4.4). Outside of the calorimeters is located the muon spectrometer (see section 3.4.5) that difines the overoll dimensions (25 m in height and 44 m in length) of the ATLAS detector.

The overall ATLAS detector layout is shown in Fig. 3.4 and its main performance goals are listed in Tab. 3.2.
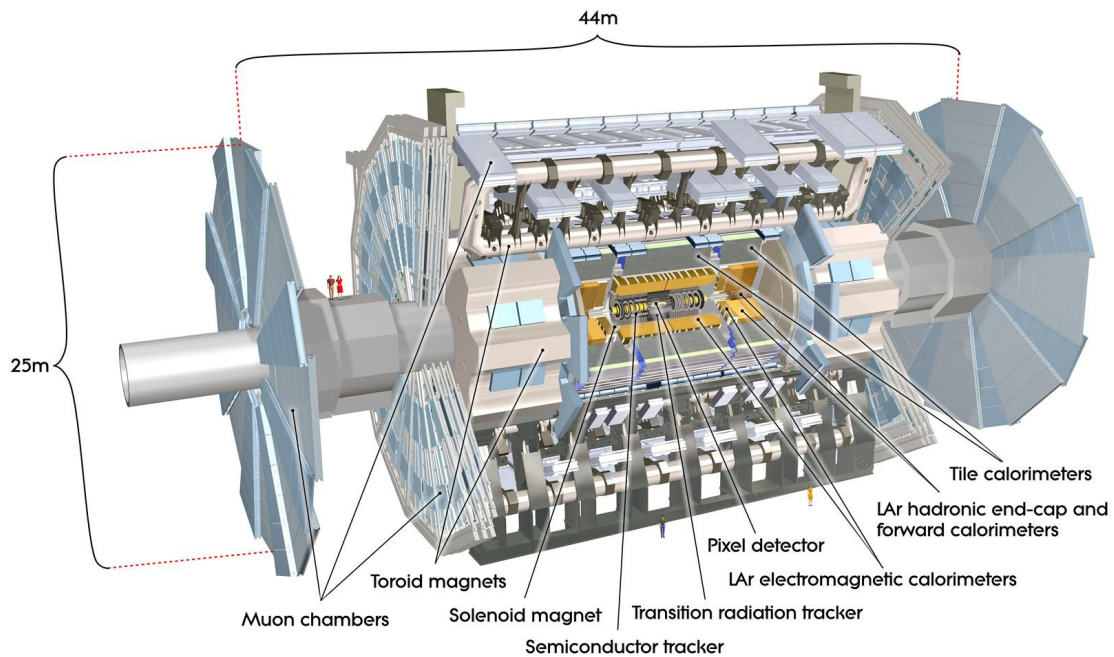
Figure 3.4: Schematic view of the ATLAS detector. The dimensions of the detector are 25 m in height and 44 m in length. The overall weight of the detector is approximately 7000 tonnes.

The origin of the ATLAS coordinate system is defined as the nominal interaction point. The beam direction defines the z-axis and the x-y plane, transverse to the beam direction. The positive x-axis is defined as pointing from the interaction point to the center of the LHC ring. The positive y-axis is defined as pointing upwards. The A-side (C-side) of the detector is defined as the side with positive (negative) z.

Detector component	Required resolution	η coverage	
		Measurement	Trigger
Tracking	$\sigma_{p_T}/p_T = 0.05\% \, p_T \oplus 1\%$	± 2.5	
EM calorimetry	$\sigma_E/E = 10\%/\sqrt{E} \oplus 0.7\%$	± 3.2	± 2.5
Hadronic calorimetry			
barrel and end-cap	$\sigma_E/E = 50\%/\sqrt{E} \oplus 0.3\%$	± 3.2	± 3.2
forward	$\sigma_E/E = 100\%/\sqrt{E} \oplus 10\%$	$3.1 < |\eta| < 4.9$	$3.1 < |\eta| < 4.9$
Muon spectrometer	$\sigma_{p_T}/p_T = 10\%$ at $p_T = 1$ TeV	± 2.7	± 2.4

Table 3.2: General performance goals of the ATLAS detector. The units for E and p_T are GeV.

3.4.2 Magnet System

The ATLAS magnet system is a complex of four large supercunditing magnets with unique features. The geometry of magnet windings can be seen in Fig. 3.5. It has been designed to provide the optimal conditions for particle identification and momentum measurement for each detector system separately. It consists of a *Central Solenoid*, a *Barrel Toroid* and two *End-Cap Toroids* described in the following.

Central Solenoid

The central solenoid is aligned on the beam axis and designed to provide a 2 T axial magnetic field for the inner detector. This 2 T field strength, with a peak of 2.6 T at the windings, was chosen to maintain good tracking for low p_T particles that otherwise in a stronger magnetic field would never reach the inner detector. The position of the central solenoid in front of the elctromagnetic calorimeter demands a careful minimisation of the material in order to achieve the desired calorimeter performance. The axial length of the solenoid is 5.8 m and the inner and outer diameters are 2.46 m and 2.56 m respectively, resulting in a total thickness of 0.66 radiation lengths. The coil mass is 5.4 tonnes and the stored energy is 40 MJ.

The electromagnetic forces are counteracted by the combination of the coil and warm-to-cold machanical support, which maintains the concentricity of the windings.

Barrel Toroid

The barrel toroid consists of eight coils encased in individual racetrack-shaped, stainless-steal vacuum vessels. It is installed outside the hadronic tile calorimeter
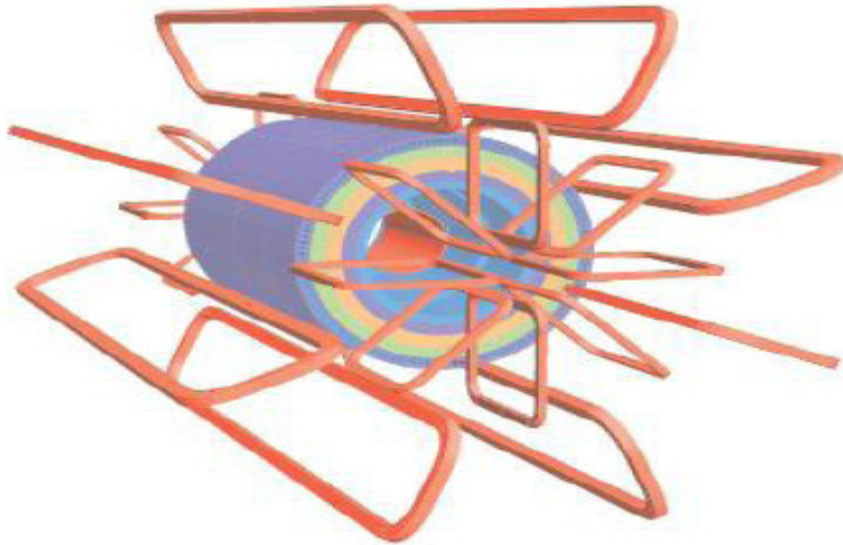
Figure 3.5: Geometry of magnet windings and tile calorimeter steel. The eight barrel toroid coils, with the end-cap coils interleaved are visible. The solenoid winding lies inside the calorimeter volume.

and it's designed to provide an average toroidal magnetic field of approximately 0.5 T (the peak field is 4 T) for the muon detectors in the central regions. The total length is 25 m, the outer diameter is 20.1 m and inner diameter is 9.4 m. The conductor and coil winding technology is essentially the same in the barrel and end-cap toroids; it is based on winding a pure Al-stabilised Nb/Ti/Cu conductor into pancake-shaped coils, followed by vacuum impregnation.

End-Cap Toroids

It is composed by 8 rectangular coils arranged in a single cylindrical vessel. The outer diameter is 10.7 m while the inner diameter is 1.65 m. The total lenght is 5 m. The vessel is mounted at the ends of ATLAS in order to close the magnetic field lines produced by the Barrel Toroid. With this configuration the magnetic field is orthogonal to the beam axis and has a value of 2 T.

3.4.3   Inner Detector

The ATLAS Inner Detector (ID) shown in Fig. 3.6 is totally immersed in the 2 T magnetic field formed by the central solenoid. The ID consists of the three independent but complementary sub-detectors of Fig. 3.7. At inner radii, high-resolution pattern recognition capabilities are available using discrete space-points from sili-

con *pixel* layers and stereo pairs of silicon microstrip (SCT) layers. At larger radii, the transition radiation tracker (TRT) comprises many layers of gaseous straw tube elements interleaved with transition radiation material.

These three subsystems function independently in order to have precise measurements of the charged particles trajectories, including impact parameter measurements and vertexing within the pseudorapidity range $|\eta| < 2.5$.
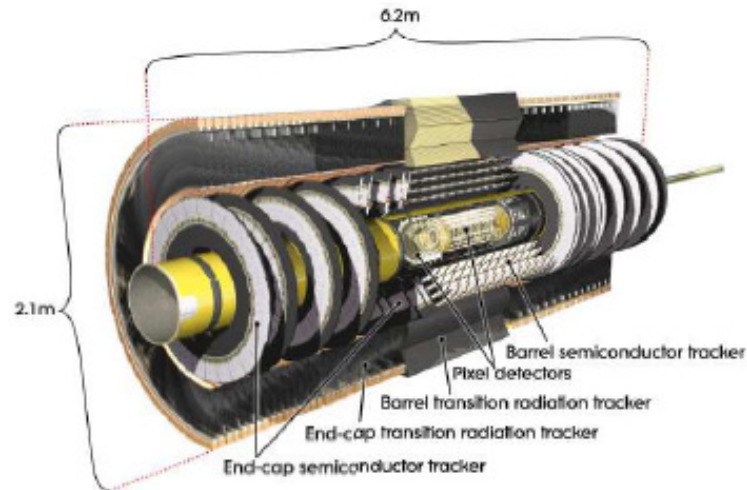
Figure 3.6: The layout of the Inner Detector.

The Pixel Detector

In the ATLAS vertex detector, the usage of finely segmented silicon pixel sensors provides a spatial resolution of 12 μm in $R - \phi$ and 100 μm in z. These performances are needed in order to obtain a spacial resolution better than the characteristic length scale of the heavy quark decay that is of the order of $c\tau = 100 - 400$ μm.

The nominal pixel size is 50 μm in the ϕ direction and 400 μm in z (barrel region, along the beam axis) or r (end-cap region). The pixel detector is made from 1744 tile-like modules. Each module contains 47232 pixel sensor covering an active area of 16.4×60.8 mm^2 and resulting in over 80 million read-out channels. To ensure maximal coverage, the sensor modules are mounted in staves along the z-axis and tilted by 1 degree to create a small overlap between the modules in the ϕ-direction.

The Semiconductor Tracker

The SCT sensors is the second building block of the ATLAS ID. As in the pixel detector case it makes use of silicon as active material and rely on many of the same ideas and much of the same semiconductor technology. Where the pixel detector uses high granularity silicon pixel sensors, the SCT uses silicon micro-strip sensors. Each silicon detector is 6.36×6.30 cm^2 , with 768 readout strips each, with 80 μm pitch. One side of the detector have readout strips aligned along the z axis; on the other side the strips are rotated by 40 mrad to improve the resolution in the z-direction. The SCT provides eight precise measurements (four space points) and the designed resolution in the barrel are 17 μm $(R - \phi)$ and 580 μm in the z-coordinate. The total number of readout channels in the SCT is approximately 6.3 million.
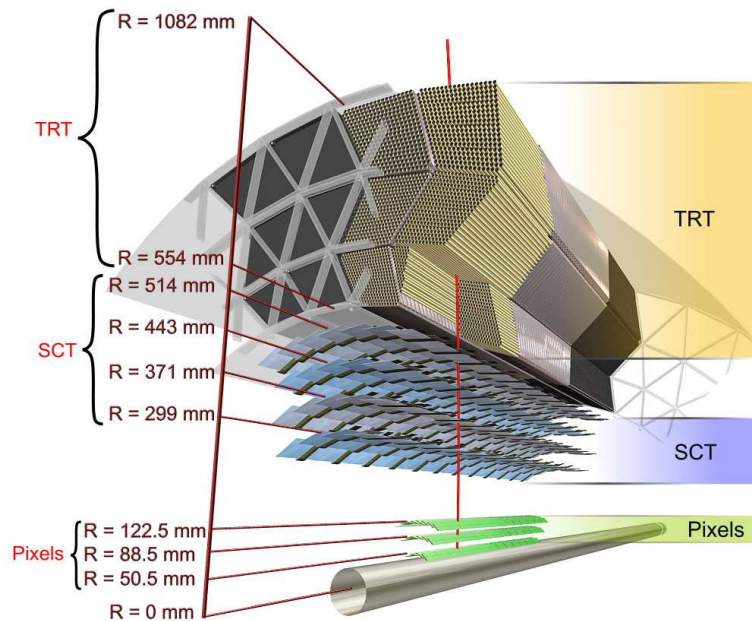
Figure 3.7: Drawing showing the sensors and structural elements of the ID traversed by a charged track of 10 GeV p_T in the barrel inner detector.

The Transition Radiation Tracker

The last subsystem in the inner detector is based on technology using gaseous drifts tubes. The basic TRT detector elements are polyaimide drift (straw) tubes filled with a gas mixture of 70% Xe, 27% CO_2 and 3% O_2. Each straw is 4 mm in diameter for a maximum straw lenght of 144 cm in the barrel. The tubes are

arranged in 36 layers. A gold-plated tungsten wire in the middle of each tube collects the signal. Each layer is interspersed with a radiator to stimulate transition radiation from ultrarelativistic particles. Transition radiation arises when an ultra-relativistic charged particle traverses the boundary between materials of different dielectric constants. This effect is proportional to the γ-factor of the traversing particle and can provide particle identification capabilities from the amount of transition radiation produced by a given particle.

The TRT system can provide 36 hits per track with an intrinsic precision of 130 μm per tube covering the range $\eta < 2.0$. In the barrel region ($|\eta| < 1.0$), the tubes are placed parallel to the beam axis, while in the end-cap regions ($0.8 < |\eta| < 2.0$) they are arranged radially on wheels.

3.4.4   Calorimeters

The ATLAS calorimeters (Fig. 3.8) consist of a number of sampling detectors with full ϕ-symmetry and coverage around the beam axis. Calorimeters in ATLAS absorb and measure the energy of charged and neutral particles, as well as jets. They also detect missing transverse energy by summing up all the measured energy deposits. Missing energy can be a sign of interesting new physics, such as the production of new weakly interacting neutral particles as neutralinos. Fig. 3.9 shows the amount of material in units of radiation length of each part of the calorimeters. These requirements are necessary in order to fully stop the most energetic particles produced in *pp* collisions at ATLAS.
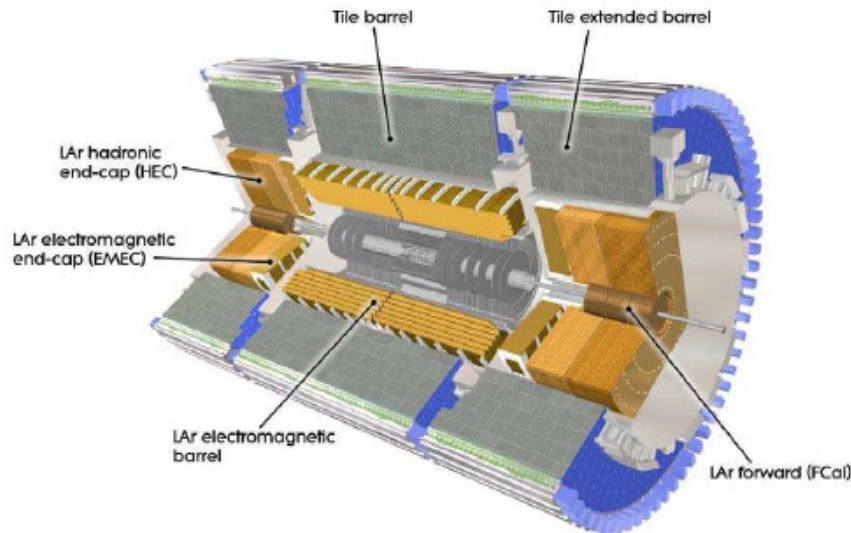
Figure 3.8: The ATLAS calorimetry system.
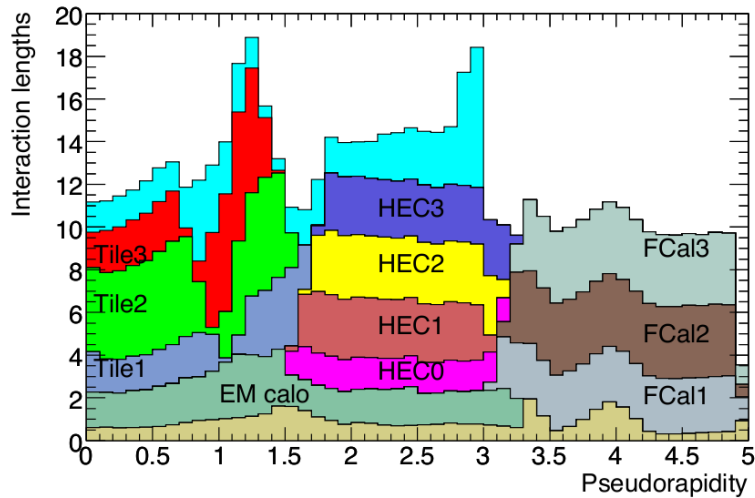
Figure 3.9: Cumulative amount of material, in units of interaction length, as a function of $|\eta|$, in front of the electromagnetic calorimeters, in the electromagnetic calorimeters themselves, in each hadronic layer, and the total amount at the end of the active calorimetry.

The Electromagnetic Calorimeter

The ATLAS electromagnetic (EM) calorimeter is designed to identify and measure with high precision the energy of electrons and photons. It surrounds the inner detector and is divided into three parts. A barrel part, within $|\eta| < 1.475$, and two endcaps situated within $1.375 < |\eta| < 3.2$. The calorimeter system has also an additional forward module to cover the region closest to the beam ($3.1 < |\eta| < 4.9$).

The barrel and the end-cap modules are divided into three parts, the so-called *samplings*, with different granularity depending on the distance from the interaction point. A sketch of a barrel module of the EM calorimeter is shown in Fig. 3.10.

The EM calorimeter is composed by liquid argon as active material, with accordion-shaped kapton electrodes, and lead absorber plates as passive medium. When a particle traverses the liquid argon gap, it creates charge by ionization. The signal is then collected on readout electrodes. The EM calorimeter in the region $0 < |\eta| < 1.8$ is preceded by a presampler detector to correct for electron energy losses in the material upstream the EM calorimeter. The performances of the ATLAS calorimeter are reported in Tab. 3.2.
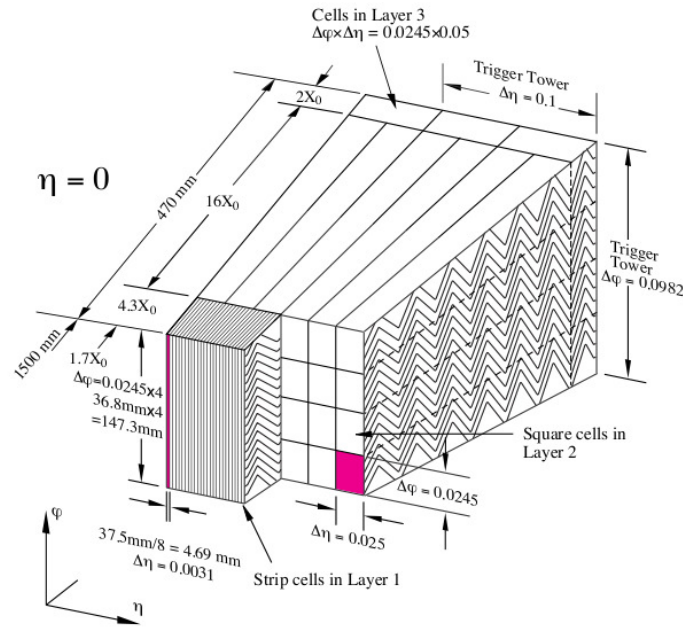
Figure 3.10: Sketch of a barrel module of the electromagnetic calorimeter where the different layers and *sampling* granularity are clearly visible.

The Hadronic Calorimeter

The hadronic calorimeters are designed to absorb and measure particles that interact via the strong nuclear force. They consist of a Hadronic Tile Calorimeter (HTC) made of iron and plastic scintillator (tile) in the barrel region ($|\eta| < 1.7$), a liquid argon sampling calorimeter in the end-caps (Hadronic End-Caps Calorimeter, HEC) for $1.5 < |\eta| < 3.2$ coverage, and a Forward Calorimeter (FCAL), very close to the beam pipe, made of liquid argon, iron and tungsten, that covers the region of $|\eta| < 5$.

The ATLAS tile sampling calorimeter has a unique feature. In this detector the tiles are made to point radially out from the beam line. In this way, the particles emerging from the interaction point traverse the tiles in the longitudinal direction. This kind of design has the possibility to reach a finer readout segmentation in the z direction for high p_T particles giving a better shower shape determination and E_T^{miss} resolution.

At higher η, the radiation level will be higher and thus the hadronic calorimeter (HEC) in the region behind the EM end-caps is based on the more radiation resistant liquid argon tecnology. Here, the absorber material is copper. Finally the FCAL at the highest η must therefore be designed to cope with a very high particle flux.

The thicknesses of the calorimeters have to be tuned in order to contain all the hadronic shower, to minimize the punch-through into the muon system and to provide a good resolution for high energy jets. The total thickness is 11 interaction lengths. The overall performances are summarized in Tab. 3.2.

3.4.5   Muon Spectrometer

The muon spectrometer forms the outer part of the ATLAS detector and is designed to detect charged particles exiting the barrel and end-cap calorimeters and to measure their momentum in the pseudorapidity range $|\eta| < 2.7$. It is also designed to trigger on these particles in the region $|\eta| < 2.4$. The driving performance goal is a stand-alone transverse momentum resolution of approximately 10% for 1 TeV tracks, which translates into a sagitta along the z (beam) axis of about 500 μm, to be measured with a resolution of ≤ 50 μm. Muon momenta down to a few GeV (~ 3 GeV, due to energy loss in the calorimeters) may be measured by the spectrometer alone. Even at the high end of the accessible range (~ 3 TeV), the stand-alone measurements still provide adequate momentum resolution and excellent charge identification. To meet these requirements the muon system uses two types of precision tracking chambers, namely the Monitored Drift Tube chambers (MDT) at low $|\eta|$ and the Cathode-Strip Chambers (CSC) at high $|\eta|$.

The capability to trigger on muon tracks is an additional design criteria of the muon system. For this purpose, dedicated fast trigger chambers have been installed in between the precision chambers in both the barrel and the end-cap region. In the barrel region ($|\eta| < 1.05$), Resistive Plate Chambers (RPC) were selected for this purpose while in the end-cap ($1.05 < |\eta| < 2.4$) Thin Gap Chambers (TGC) were chosen. A general view of the muon spectrometer is shown in Fig. 3.11.

Precision Tracking Chambers

The basic detection elements of the MDT chambers are aluminium tubes of 30 mm diameter and 400 μm wall thickness, with a 50 μm diameter central W-Re wire. The tubes are operated with a non-flammable mixture of 93% Ar and 7% CO_2 at 3 bar absolute pressure. The shape and dimensions of the drift tubes were in general chosen to optimize solid angle coverage. To obtain high spatial resolution the MDTs chambers are constructed from 2×4 monolayers of drift tubes for the inner station and 2×3 monolayers for the middle and outer stations. In this way an overall spatial resolution of 30 μm can be achieved.

The sensitive element of the CSC's is a multi-wire proportional chambers with the wires oriented in the radial direction. Each chamber is composed of several layers where each layer is made from an 18.75 mm thick sheet of polyurethane foam sandwiched between two 0.82 mm thick copper-clad laminates in which a 17
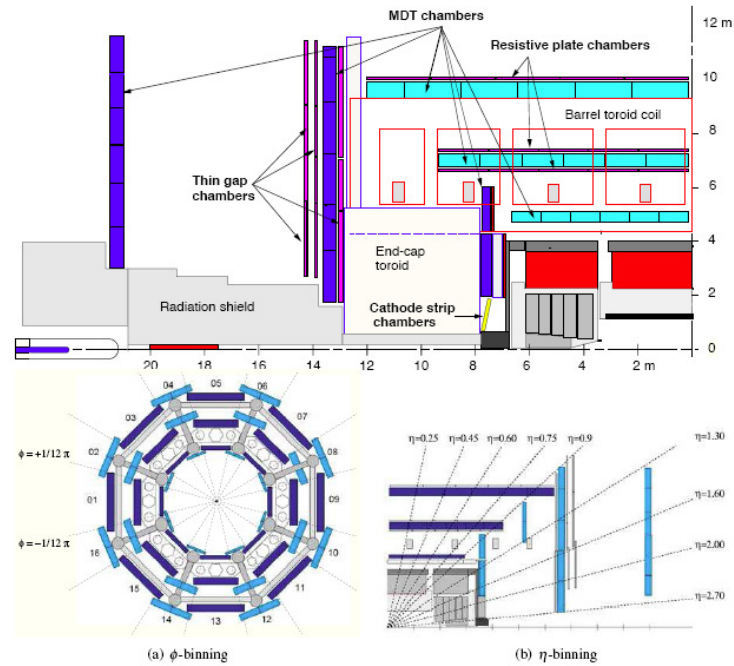
Figure 3.11: End and side view of the muon spectrometer.

μm thick copper cladding forms the cathodes. Both cathodes are segmented, one with the strips perpendicular to the wires (providing the precision coordinate) and the other parallel to the wires providing the transverse coordinate. The position of the track is obtained by interpolation between the charges induced on neighbouring cathode strips. The anode wires have a diameter of 30 μm and are made of gold-plated tungsten with 3% rhenium, however the anode signal is not read out. The CSC's chambers are arranged in two disks of eight chambers each.

Trigger Chambers

The trigger chambers of the muon system provide fast information on muon tracks traversing the detector, allowing the first level of trigger (see section 3.6) logic to recognize their multiplicity and approximate energy range.

The RPC is a gaseous parallel electrode-plate (i.e. no wire) detector. Two resistive plates, made of phenolic-melaminic plastic laminate, are kept parallel to each other at a distance of 2 mm by insulating spacers. The electric field between the plates of about 4.9 kV/mm allows avalanches to form towards the anode, along the ionizing tracks. The signal is read out via a capacitive coupling to metallic strips, which are mounted on the outer faces of the resistive plates.

Thin Gap Chambers (TGC's) are used in the end-cap region. They operate on

the same principle as multi-wire proportional chambers, and they provide good time resolution and high rate capability. TGC's are multi-wire proportional chambers with a wire-to-cathode distance of 1.4 mm being smaller than the wire-to-wire distance of 1.8 mm, as shown in Fig. 3.11. With a highly quenching gas mixture of CO_2 and n-C_5H_{12} (n-pentane), this cell geometry allows for an operation in a quasi-saturated mode, i.e. with a gas gain of 3×10^5.

3.5   ATLAS Forward Detectors

A precise luminosity measurement is an important benchmark for the search of new physics in a modern particle experiment. Different types of forward detectors have been designed and developed in ATLAS to accomplish this task according to the space left by the other subdetectors.

Fig. 3.12 shows the ATLAS forward detectors ordered according to their distance from the interaction point (IP). The closest to the IP is a Cerenkov detector called LUCID (LUminosity measurement using Cerenkov Integrating Detector, see section 3.5.1), the second system is the Zero-Degree Calorimeter (ZDC, see section 3.5.2) and the most remote detector is the absolute luminosity detector ALFA (Absolute Luminosity For ATLAS, see section 3.5.3). In addition to these subdetectors in section 3.5.4 is presented the BCM (Beam Condition Monitor) since it is used in ATLAS luminosity determination (see section 3.5.5).
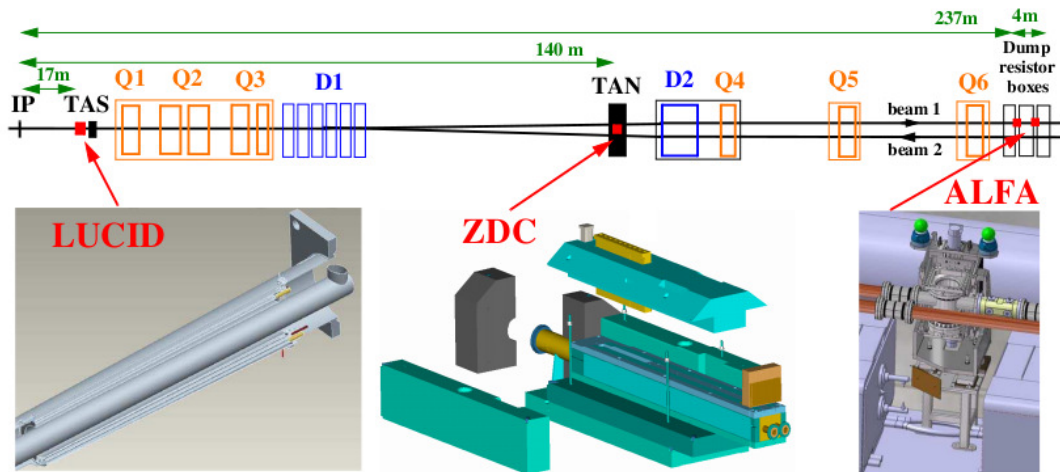
Figure 3.12: Placement of the forward detectors along the beam-line around the ATLAS interaction point.

3.5.1 LUCID

LUCID is a Cherenkov detector specifically designed for measuring the luminosity in ATLAS. Sixteen mechanically polished aluminium tubes filled with C_4F_{10} gas sorround the beampipe on each side of the IP at a distance of 17 m, covering the pseudorapidity range $5.6 < |\eta| < 6.0$. The Cherenkov photons created by charged particles in the gas are reflected by the tube walls until they reach the photomultiplier tubes (PMTs) situated at the back end of the tubes. Additional Cherenkov photons are produced in the quartz PMT window. The Cherenkov light created in the gas tipically produces 60-70 photoelectrons per incident charged particle, while the quartz window adds another 40 photoelectrons to the signal. If one of the LUCID PMTs produces a signal over a preset threshold (equivalent to $\simeq 15$ photoelectrons), a "hit" is recorded for that tube in that bunch crossing.

3.5.2 ZDC

The ZDC detector is mainly dedicated to measure the centrality in heavy ion collisions. It is able to count and measure the energy of the neutral particles at zero degrees with respect to the beam line that are not swapt away by the magnetic field in the beam pipe. Since in Pb-Pb collisions the centrality of the interaction is strongly correlated to the very forward (spectator) neutrons, the impact parameter can be measured by ZDC. In *pp* collisions ZDC provides an additional minimum bias trigger for ATLAS.

The pseudo-rapidity range covered by ZDC is $|\eta| > 8.3$. ZDC is a sampling compact calorimeter composed of tungsten alloy as absorber material and quartz fibers, which generate and transmit the Cherenkov light produced by showers of secondaries to the readout system.

The ZDC is situated in a slot in the TAN (Target Absorber Neutral) absorber, which would otherwise contain inert copper bars as shielding. The TAN is located at ± 140 m from the interaction point, at the place where the straight-section of the beam-pipe is divided back into two independent beam-pipes.

3.5.3 ALFA

ALFA is the ATLAS system for the determination of LHC absolute luminosity via elastic scattering at small angles. The accuracy of $2 - 3\%$ in luminosity measurement can be achieved by using special optics configuration: LHC running at high β^* , low luminosity and parallel-to-point focusing, to focus all the particles scattered at the same angle in the same position y at the detector position.

To measure the particles scattered at very small angles (about 3 μrad), the detector must approach the beam to about 1.5 mm. The technology used to achieve

this goal is the so-called Roman Pot, a system integrated with the beam pipe and able to move the detector close to the beam.

ALFA is situated at 240 m from the interaction point at either sides of ATLAS. Each module is composed by 2 groups of scintillating plastic fibers of square cross-section (0.5×0.5 mm^2), at 90 degrees with respect to each other. A tipical spatial resolution obtained with this configuration is about 30 μm. The pseudo-rapidity coverage range is $10.6 < |\eta| < 13.5$.

3.5.4   BCM

The BCM detector consists of two stations (forward and backward) each with four modules placed close to the beam pipe. Each module includes two diamond sensors read out in parallel. The stations are located symmetrically around the interaction point, positioning the diamond sensors at $z = \pm 184$ cm and $r = 55$ mm (a pseudo-rapidity of about 4.2). Equipped with fast electronics (2 ns rise time) these stations measure time-of-flight and pulse height to distinguish events resulting from lost beam particles from those normally occurring in proton-proton interactions. BCM also provides a measurement of bunch-by-bunch luminosities in ATLAS by counting in-time and out-of-time collisions. It was indeed originally designed to monitor background levels and issue beam-abort requests when beam losses start to risk damaging the Inner Detector.

3.5.5   Luminosity Overview

The rate of physics processes produced at colliders is a function of both their cross section and the luminosity of the collider. The instantaneous luminosity, providing the event rate for unit cross section, depends on the number of particles circulating into the beams as well as the overlap integral of the beams. For two perfectly head-on beams, the higher the number of particles and the smaller the beam size, the higher the number of collisions. In order to discover rare processes high luminosity or, equivalently, high event-rate is a must.

Instantaneous and Integrated Luminosities

The *instantaneous* luminosity $\mathscr{L}$ is defined as the ratio between the interaction rate R of any process and its cross section σ. It is expressed in units of $cm^{-2}s^{-1}$ and it is independent of the process itself.

$$\mathscr{L} = \frac{R}{\sigma} \tag{3.1}$$

The instantaneous luminosity can be inferred from the machine parameters: if the two beams are made of identical bunches, these are Gaussian in shape and perfectly overlapping without crossing angle, the luminosity is given by:

$$\mathscr{L} = f_r n_b \frac{N_1 N_2}{4\pi \sigma_x \sigma_y} \tag{3.2}$$

where $\sigma_{x,y}$ are the gaussian transverse profiles of the beams, e.g. the standard deviations of the bidimentional gaussians, N_1 and N_2 are the number of protons in the bunches of beam 1 ans 2, n_b is the number of bunches and f_r is the beam-revolution frequency.

Eq. 3.2 can be rewritten also in terms of other parameters which are directly accessible from LHC:

$$\mathscr{L} = F \frac{N_1 N_2 f_r n_b \gamma}{4\pi \beta^* \epsilon} \tag{3.3}$$

where N_1 and N_2 are the number of particles in the bunches, γ is the relativistic factor for the colliding particles (i.e. E_p / m_p for the colliding protons at the LHC), ϵ is the emittance which describes the extent occupied by the particles of the beam in the phase space. The beta functions β^* describes the focusing properties of the magnetic lattice and F is a factor that takes into account the angle at which the beams cross each other.

The *integrated* luminosity L is obtained by integrating the instantaneous luminosity over a certain time interval t and is expressed in units of cm^{-2}:

$$L = \int_0^t \mathscr{L}(t') dt' \tag{3.4}$$

At LHC, the instantaneous luminosity is expected to decrease by 1% every 10 minutes according to the power law:

$$\mathscr{L} = \mathscr{L}_0 e^{-\frac{t}{\tau}} \tag{3.5}$$

where $\tau \simeq 14$ h.

Luminosity Calibration Via Van der Meer Scan

To determine the luminosity by means of Equations 3.2 or 3.3 is difficult since a good measurement of the lateral beam sizes is needed. One way to obtain reliable measurement of the beam sizes at the IP is to measure the beam profile in some place away from the interaction point (IP) and then extrapolate to the IP. The drawback of this method is that a good knowledge of the β^* function is needed for the extrapolation. Since the uncertainty of the β^* function can be as high as 10%, this sets a upper limit in the precisions at which the absolute luminosity can be

determined using this method. This uncertainty could possibly be reduced if the beam divergence at the IP can be measured.

Another way to measure the beams widths at the IP was originally proposed by *Van der Meer* in 1968 [51]. In this method the beam sizes can be determined by moving the two beams across each other and simultaneously monitor the relative change in counting rate.

In terms of colliding beam parameters, the luminosity is defined as:

$$L = n_b f_r N_1 N_2 \int \rho_1(x, y) \rho_2(x, y) dx dy \tag{3.6}$$

where n_b is the number of colliding bunches, f_r is the machine revolution frequency (11245.5 Hz for LHC), $N_{1(2)}$ is the number of particles per bunch in beam 1(2) and $\rho_{1(2)}(x, y)$ is the particle density in the transverse plane (x-y) of beam 1(2) at the IP. Under the general assumption that there is no correlation between x and y, the luminosity can be written as:

$$L = n_b f_r N_1 N_2 \Omega_x(\rho_1(x)\rho_2(x)) \Omega_y(\rho_1(y)\rho_2(y)) \tag{3.7}$$

where:

$$\Omega_x(\rho_1, \rho_2) = \int \rho_1(x)\rho_2(x) dx \qquad \rho_1(x) = \int \rho_1(x, y) dy \tag{3.8}$$

Ω_x is the beam overlap integral in the x direction, with an analogous definition for the overlap integral in the y direction. With the Van der Meer method the overlap integral can be calculated as:

$$\Omega_x(\rho_1, \rho_2) = \frac{R_x(0)}{\int R_x(x) dx} \tag{3.9}$$

where $R_x(x)$ is the rate at displacement x. We define Σ_x by the equation:

$$\Sigma_x = \frac{1}{\sqrt{2\pi}} \frac{\int R_x(x) dx}{R_x(0)} \tag{3.10}$$

When $R_x(x)$ is Gaussian, Σ_x coincides with the standard deviation of the rate distribution. By using Equations 3.9 and 3.10, the luminosity can be rewritten as:

$$L = \frac{n_b f_r N_1 N_2}{2\pi \Sigma_x \Sigma_y} \tag{3.11}$$

which is the general formula to extract luminosity from machine parameters by performing a beam separation scan.

The main source of systematics to the luminosity determined from beam parameters is the uncertainty in the measurements of the beam currents. Other errors come from the relative centering of the two beams and systematic uncertainties related to the change of the beam emmitance during the scans. A complete discussion on systematics uncertainties on the absolute luminosity calibration can be found here [53].

Final Uncertainty on Luminosity

The luminosity scales determined by the ATLAS Collaboration for 2010 and 2011 [52] [53] have been calibrated based on *vdM* scan data. Systematics uncertainties on the absolute luminosity calibration are reported in Tab. 3.3.

Uncertainty Source	$\delta\mathscr{L}/\mathscr{L}$ [%]	
Data Year	2010	2011
Bunch Population Product	3.1	0.5
Other *vdM*		
Calibration Uncertainties	1.3	1.4
Afterglow Correction		0.2
BCM Stability		0.2
Long-Term Consistency	0.5	0.7
μ Dependence	0.5	0.5
Total	3.4	1.8

Table 3.3: Relative uncertainty on the calibrated luminosity scale broken down by source.

The combination of these systematic uncertainties results in a final uncertainty on ATLAS luminosity scale during *pp* collisons at $\sqrt{s} = 7$ TeV of $\delta\mathscr{L}/\mathscr{L} = \pm 3.4\%$ for the 48 pb^{-1} of data delivered in 2010 and $\delta\mathscr{L}/\mathscr{L} = \pm 1.8\%$ for the 5.6 fb^{-1} delivered in 2011.

The analysis presented in this thesis, although fully based on 2011 data, was completed before the final value ($\pm 1.8\%$) became public. As a consequence the final results reported here will be affected by a preliminary 2011 luminosity uncertainty existimation that was $\pm 3.9\%$.

3.6 ATLAS Trigger and Data Acquisition Systems

At LHC, the production cross section of interesting physics signatures (Higgs production, SUSY particles etc...) is expected to be around seven orders of magnitude lower than the cross section of minimum bias QCD events. To record all minimum bias events, considering that each colliding event corresponds to ~ 1 MB space, one would need 40 TB free disc space per each second. Since current technology does not allow this enormous amount of data to be captured the ATLAS experiment developed a series of procceses, called the trigger system, to filter

out the minimum bias events with a rejection factor of at least 10^7 while keeping 100% efficiency in the selection of interesting physics.
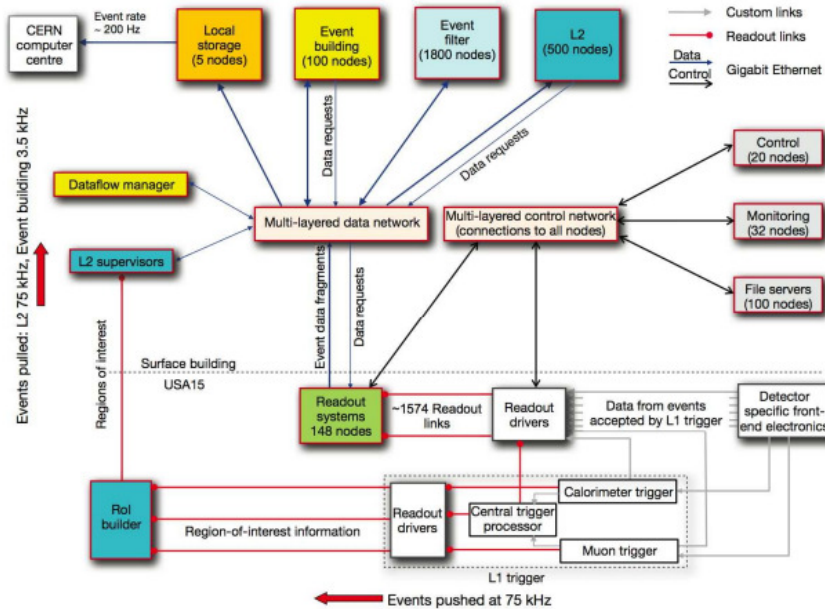
Figure 3.13: Block diagram of the ATLAS trigger and data acquisition systems.

At ATLAS this trigger system [54] is divided into three levels called Level-1 (LVL1), Level-2 (LVL2), and the Event Filter (EF). Each trigger level refines the decisions made at the previous level and, where necessary, applies additional selection criteria. A block diagram of the ATLAS trigger and data acquisition (DAQ) systems can be seen in Fig. 3.13.

The LVL1 trigger makes fast decision in order to select the bunch crossings containing interesting events. It is hardware based and receives data from the calorimeters and the muon system (RPCs and TGCs). LVL1 fast identifies and processes the so-called Regions-of-Interests (RoI's) of each event, where high activity has been detected. The RoI's are essentially geographical coordinates in η and ϕ, for which the LVL1 selection process has identified an interesting signature using informations coming from the various sub-systems. The LVL1 target is to reduce the initial rate of 40 MHz to 75 kHz in order to be handle by the detector readout systems. The time necessary for L1 to decide whether to reject or keep the event is 2.5 μs.

The second step of the ATLAS trigger system is the LVL2 which refines the information from the previous step by acquiring additional data from increasingly more detectors. The LVL2 trigger uses RoI information on coordinates, energy, and type of signatures to limit the amount of data which must be transferred from

the detector readout. The LVL2 trigger reduces the event rate to below 3.5 kHz, with an average event processing time of approximately 40 ms.

The final stage of the event selection is carried out by the EF. It uses offline analysis procedures on fully-built events to further select events down to a rate which can be recorded for subsequent offline analysis. The EF reduces the event rate to approximately 200 Hz, with an average event processing time of order four seconds.

The ATLAS DAQ receives and buffers the event data from the detector-specific readout electronics at the LVL1 trigger rate. It transmits to the LVL2 trigger any data requested by the trigger (typically the data corresponding to RoI's) and, for those events fulfilling the LVL2 selection criteria, event-building is performed. The assembled events are then moved by the data acquisition system to the event filter, and the events selected there are moved to permanent event storage. In addition to controlling movement of data down the trigger selection chain, the data acquisition system also provides for the configuration, control and monitoring of the ATLAS detector during data-taking. Supervision of the detector hardware (gas systems, power-supply voltages, etc.) is provided by the Detector Control System (DCS).

Chapter 4

$ZZ \to \ell^-\ell^+\ell^-\ell^+$ Event Selection and Recostruction

4.1 Introduction

This chapter is an accurate description of the event and object selection to perform the ZZ cross section measurement presented in the next chapter. The LHC 2011 data collected at $\sqrt{s} = 7$ TeV using the ATLAS detector together with MC samples are described in section 4.2. The selection criteria for the ZZ events decaying in the four charged leptons channel are described in section 4.3.

4.2 Data Samples

4.2.1 Data 2011

This study uses a data sample of proton-proton collisions taken between February and November 2011 at a center-of-mass energy of $\sqrt{s} = 7$ TeV at the LHC. Events are selected using a data-quality flag called Good Run List (GRL) in which the good operational state of each sub-detectors is required. The total integrated luminosity as reported by the ATLAS luminosity calculation tool is 4640 pb^{-1}. The estimate of the luminosity uncertainty is 3.9% as discussed in section 3.5.5. In AT-LAS data are recorded in different physics streams depending to the trigger object (electron, muon, jet, etc...) that fired the event. Two data streams are used in this analysis: `physics_Muons` and `physics_Egamma`. From about one month and a half, May to June 2011, part of the calorimeter (corresponding to 6 Front-End boards) was absent from data taking. The corresponding decrease in detector acceptance is taken into account by a proper scaling in the Monte Carlo samples.

4.2.2 Signal Monte Carlo Samples

The $ZZ \to \ell^+ \ell^- \ell^+ \ell^-$ process is modeled using PowhegBox [11] as signal MC. PowhegBox is a next-to-leading order (NLO) MC generator, with up to one parton in addition to the ZZ system which use CT10 as parton density function (PDF) set. In addition, the LO multi-leg generator Sherpa [16] with the CTEQ6L1 PDF set [27] is used to evaluate systematic uncertainties by comparing with PowhegBox and to generate signal samples with anomalous neutral triple gauge couplings. Since the above mentioned samples have only $q\bar{q} \to ZZ$ production, the $gg \to ZZ$ production is estimated using GG2zz [17] interfaced to Herwig [13] and Jimmy [14] for hadronization and multiple parton scattering. The Z^*/γ^* interference is implemented appropriately in all the above generators.

MCID	Process	Generator	events	fiducial k-factor (ZZ ; ZZ*)	ϵ_{filter}	cross section [pb]
126159	$ZZ \to e^+ e^- e^+ e^-$	PowhegBox	100000	1.00 ; 1.00	0.70	0.0657
126160	$ZZ \to \mu^+ \mu^- \mu^+ \mu^-$	PowhegBox	100000	1.00 ; 1.00	0.71	0.0657
126861	$ZZ \to e^+ e^- \mu^+ \mu^-$	PowhegBox	200000	1.00 ; 1.00	0.63	0.1516
126862	$ZZ \to \mu^+ \mu^- \tau^+ \tau^-$	PowhegBox	200000	1.00 ; 1.00	0.13	0.1517
126863	$ZZ \to e^+ e^- \tau^+ \tau^-$	PowhegBox	200000	1.00 ; 1.00	0.13	0.1515
126864	$ZZ \to \mu^+ \mu^- \tau^+ \tau^-$	PowhegBox	100000	1.00 ; 1.00	0.013	0.06597
116600	$gg \to ZZ \to \ell^+ \ell^- \ell^+ \ell^-$	GG2zz	65000	1.00 ; 1.00	0.60339	0.00279
116601	$gg \to ZZ \to e^+ e^- e^+ e^-$	GG2zz	65000	1.00 ; 1.00	0.99319	0.00279
116602	$gg \to ZZ \to \mu^+ \mu^- \mu^+ \mu^-$	GG2zz	65000	1.00 ; 1.00	0.99475	0.00279
116603	$gg \to ZZ \to e^+ e^- \mu^+ \mu^-$	GG2zz	65000	1.00 ; 1.00	0.99411	0.00558
126148	$ZZ \to \ell^+ \ell^- \ell^+ \ell^-$	Sherpa	459998	1.68 ; 1.60	1.0	0.26622

Table 4.1: The ZZ signal production process, the MC ID run number, the MC generator used, the cross section and number of fully simulated MC events are given above. The MC simulation filter is an event selection at the generator level.

In Tab. 4.1 the ZZ MC signal samples used in this analysis are listed. The corresponding cross section, the k-factor needed to correct this to the NLO prediction (calculated with respect to the NLO MCFM [15] prediction), and the event generator filter efficiency are shown. The filters are mainly used to reject τ events. In the Sherpa sample a dilepton mass of at least 12 GeV, and for the lepton p_{T} to be > 1 GeV are required, while the PowhegBox filter requires 3 leptons with $p_{\text{T}} > 5$ GeV and a dilepton mass >4 GeV. Finally, in the GG2zz samples, a filter demanding at least 3 leptons (e or μ) with $p_{\text{T}} > 5$ GeV and $|\eta| < 10$ is applied to

the events at the generator level.

ATLAS is simulated [56] with a program based on Geant4 [57]. The simulation includes the detector response to additional inelastic pp events, distributed so as to reproduce the number of collisions per bunch-crossing in the data. Interactions in the out-of-time bunches from pile-up are also included in the simulation.

4.2.3 Background Processes

The Z+jets W+jets, $Z\gamma$ and $W\gamma$ (Tables A.1 and A.2) backgrounds are modeled using LO ALPGEN [58] generator with CTEQ6L1 PDFs set interfaced with Herwig and Jimmy for parton showers and underlying events respectively. Top quark background events ($t\bar{t}$, Wt and single top, Tab. A.3) as well as WW background are simulated with MC@NLO [12] with CT10 PDFs. For W/Z+γ (Tab. A.4), MADGRAPH [59] LO generator with CTEQ6L1 PDFs is also used together with Pythia for hadronization and showering. Finally, events with heavy flavor dijets (Tab. A.3) are modeled with PYTHIAB [60].

The cross sections for the simulated processes, generator names, generator level filter efficiencies and total number of events are shown in Appendix A. Whenever LO event generators are used, the cross sections are corrected by using k-factors to NLO or NNLO (if available) derived from matrix element calculations [61].

4.3 $ZZ \to \ell^-\ell^+\ell^-\ell^+$ Selection Criteria

Electrons and muons are the physics objects needed in the analysis for the ZZ events reconstruction. The ZZ candidate must pass a series of requirements, based on event preselection criteria (see section 4.3.1), lepton object requirements (see section 4.3.2) and finally selection requirements of the ZZ system (see section 4.3.3).

4.3.1 Event Preselection

The 'preselection' is commonly used to select a 'good' event rejecting cosmic ray background and events with bad data-quality flag. The event preselection cuts applied are reported here:

1. **Good Runs List cut**
   Keep events with the detector in a fully operational state (applied only for data).

2. **Trigger cut**
   The ZZ candidate events in all final-states are pre-selected with either the

Period	e trigger	μ trigger
B-I	e20_medium	mu18_MG
J-K	e22_medium	mu18_MG_medium
L-M	e22vh_medium1	mu18_MG_medium

Table 4.2: Lepton trigger chain used in the corresponding 2011 data periods.

unprescaled single-electron or the unprescaled single-muon triggers. The trigger chains used in the ATLAS internal subdivision and nomenclature of the 2011 dataset (labelled as "Period") are reported in Tab. 4.2.

For the electron (muon) chain a corresponding p_T of at least 20 (18) GeV is required to the leptons that fired the trigger. The lepton that fulfills the trigger requirements is called the triggered object.

3. **Primary vertex cut**
   To reject cosmic ray events, the primary vertex of the event must have at least 3 tracks associated with it.

4. **Event Cleaning cut**
   LAr calorimiter noise warning flag must not be set indicating an event with the calorimeter in a good operational state.

5. **Overlap removal cut**
   Objects are removed from the event using a ($\Delta R = \sqrt{\Delta\eta^2 + \Delta\phi^2}$) overlap criteria:

   - remove electrons within $\Delta R < 0.1$ of any selected muon;
   - if two selected electrons overlap within $\Delta R < 0.1$, remove lower-p_T electron.

4.3.2 Object Reconstruction

The reconstructed physics objects used in this study are briefly described here. The main objects needed to reconstruct the ZZ event are electrons and muons.

Electrons

The requirements which must be satisfied by the selected electrons are summerized in Tab. 4.3.

Two different kind of electrons can be distinguished depending on their pseudo-rapidity η. "Central" electrons are reconstructed in the region $|\eta| < 2.47$, while

"forward" electrons are used to extend the pesudo-rapidity coverage to $2.47 < |\eta| < 3.16$.

Requirement	$\ell^-\ell^+\ell^-\ell^+$ **final state**
Central Electron Selection:	
1. e: Type	GSF, `author==1 or 3`
2. e: Quality	`(OQ AND 1446 == 0)`
3. e: ID cut	`Loose++`
4. e: η	$\|\eta\| < 2.47$ (include crack: $1.37 < \|\eta_{Cluster}\| < 1.52$)
5. e: E_T	$E_T > 7$ GeV
6. e: z_0	$z_0 < 2$ mm
7. e: d_0	$\|d_0\|/\sigma(d_0) < 6$
8. e: Track isolation	Σp_{T} $(\Delta R < 0.2)/p_{\mathrm{T}} < 15\%$
9. e: Calorimeter isolation	calo $\Sigma E_T(\Delta R < 0.2)/E_T < 30\%$
10. e: Overlap removal	a) Remove e if $\Delta R < 0.1$ from μ
	b) Remove lowest E_T e in $\Delta R < 0.1$ from another e
Forward Electron Selection:	
1. e: Type	`author==8`
2. e: Quality	`(OQ AND 1446 == 0)`
3. e: ID cut	`Tight`
4. e: η	$2.50 < \|\eta\| < 3.16$
5. e: E_T	$E_T > 20$ GeV
6. e: Overlap removal	Remove if overlaps with central
	electron or any muon in $\Delta R < 0.1$

Table 4.3: Electron selection requirements.

Central electrons are reconstructed with the "standard" electron algorithm [62]. In order to account for the effect of bremsstrahlung in the inner detector, tracks are refitted using a Gaussian-sum filter (GSF) [63].

GSF is a non-linear generalization of the Kalman filter, which takes into account non-Gaussian noise, introduced by bremsstrahlung emission, by modeling it as a weighted sum of Gaussian components. A dedicated algorithm refits all tracks associated to existing electrons using the GSF, and then loops over electron and photon calorimeter clusters trying to match them with a GSF refitted track.

Central electrons are required to pass the 2011 egamma "Loose++" electron identification requirements [64].

To avoid problems with the front-end boards of the liquid argon calorimeter or other data quality issues, all electron candidates are required to pass an object quality cut (OQ). This OQ defines a bad electron and indicates that its cluster is affected by at least one of the following three conditions: the presence of a dead front-end board in the first or second sampling layer, the presence of a dead region affecting the three samplings, or the presence of a masked cell in the core.

To ensure that the candidates come from the primary vertex, the absolute z_0 of the electron track with respect to the primary vertex must be less than 2 mm and the d_0 significance is required to be less than 6. z_0 is the z distance of the track at the point of closest approach (longitudinal impact parameter) and d_0 is the transverse distance to the beam axis at the point of closest approach (transverse impact parameter) in the ATLAS coordinate system defined as in section 3.4.1.

Electrons in the region $1.37 < |\eta_{cluster}| < 1.52$ are retained; their energy (both for electrons in data and in simulated events) is scaled appropriately using the tools provided by the e-gamma performance group.

Electron candidates are required to have a transvers energy $E_T > 7$ GeV.

In order to reject non-prompt leptons from the decay of heavy quarks and fake electrons from misidentified jets (charged hadrons or photon conversions), all selected electrons are required to be isolated both in the tracker and in the calorimeter. The track isolation cut requires that the scalar sum of the transverse momenta of inner detector tracks inside a cone of size $\Delta R = 0.2$ around the electron must be smaller than the 15% of the electron E_T. For the calorimeter isolation, the ratio of the sum of the transverse energy in calorimeter cells within a cone of $\Delta R < 0.2$ around the electron must be less than 30% of the electron E_T. The energy in the isolation cone does not include the energy of the electron itself, and is corrected for the effects of pileup using the official prescription of the e-gamma performance group.

Forward electrons are reconstructed from calorimeter information only since ATLAS inner detector (ID) is not able to cover the pseudo-repidity range beyond $|\eta| = 2.5$. In this case the transverse momentum is computed from the calorimeter energy and the electron direction, where the electron direction is computed using the primary vertex position and the shower barycentre position in the calorimeter. Without ID informations, isolation requirements can't be imposed on such electrons and moreover it is not possible to determine the electron charge. Since the lack of tracking makes it harder to reject hadronic and photonic fakes, to lower the background these electrons are required to pass tighter identification requirements [64].

Muons

Muons are identified by matching tracks (or track segments) reconstructed in the muon spectrometer to tracks reconstructed in the inner detector [62]. The muon selection requirements for the $ZZ \to \ell^-\ell^+\ell^-\ell^+$ are summarized in Tab. 4.4.

Two different algorithm are used for muons reconstructions: the `STACO` and the `CaloTrkMuID` algorithms. The `STACO` muons reconstructed through the statistical combination of the parameters from an inner detector track and those from a muon spectrometer track or track segment are called *Combined muons* and *Segment Tag muons* respectively. If muons have no inner detector track, they are reconstructed from a muon spectrometer track only (*Stand Alone muons*, SA).

All `STACO` muons are required to pass the "loose" identification criteria.

Combined muons (CM) and *Segment Tag muons* (ST) are used in the pseudo-rapidity region $|\eta| < 2.5$, with $p_{\mathrm{T}} > 7$ GeV and they are referred to as "central muons". Muons in the region $2.5 < |\eta| < 2.7$ are defined "forward muons". Forward muons are required to have a full muon spectrometer track, which, where it is possible, it is combined with an inner-detector track. Due to inner detector pseudo-rapidity coverage, only muons up to $|\eta| < 2.6$ have such a chance, with decreasing probability as the $|\eta|$ increases. The rest of the muons in the $2.5 < |\eta| < 2.7$ region are SA, reconstructed using only the information from the muon system.

The `CaloTrkMuID` algorithm use the calorimeter to tag inner-detector tracks as originating from muons. Muons selected by this algorithm are referred to as "Calo-tag muons". "Calo-tag muons" muons are only considered in the region $|\eta| < 0.1$, and are not selected if they overlap with a selected "central muons" muon within $\Delta R < 0.1$.

A series of cuts are prescripted from the ATLAS Muon Performance group to define good quality tracks [65]. This recomandations ensure that the inner detector tracks have a minimum number of hits in each silicon sub-detector.

To ensure that the candidates come from the primary vertex (identified as the vertex that has the highest $\sum p_{\mathrm{T}}^2$ of associated tracks), the magnitude of the longitudinal impact parameter with respect to the primary vertex, $|z_0|$, must be less than 2 mm and the transverse impact parameter, d_0, must have significance ($|d_0|/\sigma_{d_0}$) less than 3.5. These requirements are not applied to *Stand Alone muons* which have no inner-detector track.

All muons are required to be isolated from energy deposits in the calorimeter. The ratio of the sum of the transverse energy in calorimeter cells within a cone of $\Delta R < 0.2$ around the muons must be less than 30% of the muon p_T for muons with $|\eta| < 2.5$. A tighter isolation ratio (less than 15%) is applied for forward muons ($2.5 < |\eta| < 2.7$).

Requirement	$\ell^-\ell^+\ell^-\ell^+$ **final state**
Standard Muons	
1. μ: type	"loose" STACO muons
	Combined or SegmentTagged
2. μ: p_T and η	$p_T > 7$ GeV, $|\eta| < 2.5$
3. μ: ID hits	MCP recommendation, see Sec.4.3.2
4. μ: z_0	$|z_0| < 2$ mm
5. μ: d_0	$|d_0|/\sigma(d_0) < 3.5$
6. μ: track iso	$\Sigma p_T(\Delta R < 0.2)/p_T < 15\%$
7. μ: calo iso	calo $\Sigma E_T(\Delta R < 0.2)/p_T < 30\%$
Forward Muons	
1. μ: type	"loose" STACO muons
	Combined or StandAlone
2. μ: p_T and η	$p_T > 10$ GeV, $2.5 < |\eta| < 2.7$
3. μ: ID hits	MCP recommendation, see Sec.4.3.2
4. μ: z_0	$|z_0| < 2$ mm
5. μ: d_0	$|d_0|/\sigma(d_0) < 3.5$
7. μ: calo iso	calo $\Sigma E_T(\Delta R < 0.2)/p_T < 15\%$
Calo-tag Muons	
1. μ: type	Calorimeter Tagged muons
2. μ: p_T and η	$p_T > 20$ GeV, $|\eta| < 0.1$
3. μ: ID hits	MCP recommendation, see Sec.4.3.2
4. μ: z_0	$|z_0| < 2$ mm
5. μ: d_0	$|d_0|/\sigma(d_0) < 3.5$
6. μ: track iso	$\Sigma p_T(\Delta R < 0.2)/p_T < 15\%$
7. μ: calo iso	calo $\Sigma E_T(\Delta R < 0.2)/p_T < 30\%$
8. Quality Cuts	`CaloMuonIDTag` > 10 $||$
	`CaloLRLikelihood` > 0.9
9. Overlap Removal	Remove if overlaps with a
	standard muon in $\Delta R < 0.1$

Table 4.4: Muon selection requirements.

4.3.3 $ZZ \to \ell^- \ell^+ \ell^- \ell^+$ Candidate Event Selection

The $ZZ \to \ell^- \ell^+ \ell^- \ell^+$ selection includes the following final states with electrons and muons: $e^+ e^- e^+ e^-$, $\mu^+ \mu^- \mu^+ \mu^-$, and $e^+ e^- \mu^+ \mu^-$. All selection criteria are the same for the three channels except for the trigger matching.

Z candidates selected are classified according to two nomenclatures:

- Classification according to the proximity to the Z-pole mass, results in the Z candidates called *primary* (closest to pole), or *secondary* (furthest from the Z pole).

- Classification according to their p_{T}, results in calling them *leading* (higher in p_{T}), or *subleading* (lower in p_{T}).

The final ZZ candidate selection steps are described in the following list.

1. **Four leptons**
   The event must have four and only four leptons passing the selection criteria listed in section 4.3.2. This cut simplifies the equations for the background estimate (see section 5.6). MC predictions show 1.3% of signal events would fail this cut. In data, no events with more than four fully selected leptons were observed.

2. **Trigger match**
   The events passing the pre-selection are required to possess a "trigger-matched lepton", i.e., a lepton that is within $\Delta R < 0.1$ of the triggered object. At least one trigger-matched lepton must have $p_T > 25$ GeV and $|\eta| < 2.47$ (if it is an electron) or $p_T > 20$ GeV and $|\eta| < 2.4$ (if it is a muon).

3. **Quadruplet Formation**
   There must be two same flavour, oppositely charged lepton pairs. In $e^+ e^- e^+ e^-$ and $\mu^+ \mu^- \mu^+ \mu^-$ events there are two possible ways of pairing the four leptons into opposite sign pairs. The pairing which minimises the quantity $|m_{12} - m_Z| + |m_{34} - m_Z|$ is chosen, where m_{12}, m_{34} are the invariant masses of the two lepton pairs consisting of leptons '1','2','3','4' and m_Z is the Z-pole.

4. **"Primary" Z candidate**
   The Z candidate closest to the Z pole must satisfy the mass cut $66 < m_{12} < 116$ GeV.

5. **"Secondary"** Z **candidate**

Two non-exclusive mass cuts are applied to the secondary Z candidate, one to select the event as a ZZ event, one to select the event as a ZZ^{*} [1] event :

(a) To be classified as a ZZ event the secondary Z candidate must satisfy the mass cut $66 < m_{34} < 116$ GeV.

(b) To be classified as a ZZ event the secondary Z candidate must satisfy the mass cut $m_{34} > 20$ GeV.

(c) The leptons are requried to be separated according to the following criteria: $\Delta R(\ell, \ell) > 0.2$.

The expected background contributions to the final selected sample are mainly modeled with a data-driven estimate. Monte Carlo simulations are used as a closure test and will be discussed in the next chapter as well as the systematics uncertainties.

4.3.4 $ZZ \to \ell^- \ell^+ \ell^- \ell^+$ **Candidate Plots**

The selection described in the previous sections leads to 84 ZZ^{*} candidates, out of which 66 are classified as ZZ candidates.

Fig. 4.1 shows an event display for a selected $ZZ \to \mu^+ \mu^- \mu^+ \mu^-$ event. The inner detector tracks are colored in red and required to have a minimum transverse momentum of 200 MeV. The four reconstructed muon tracks are drawn in blue. The muon precision chambers shown in green have recorded at least 6 hits. The yellow structures belong to the muon trigger system. In purple, all calorimeter cells of the hadronic endcap calorimeters and the forward calorimeters with energy deposits of at least 1 GeV are shown, while in light green are the cells of the electromagnetic calorimeter fulfilling the same requirement.

The pseudorapidity η and rapidity Y distributions of leading and subleading Z for the ZZ^{*} and ZZ candidates are shown in Fig. 4.2 and Fig. 4.3, respectively.

The transverse momentum (p_T) of the two leptons forming the leading Z in both ZZ^{*} and ZZ candidates selection are reorted in Fig. 4.4. In these plots data points are compared with only PowhegBox signal.

Figure 4.5 shows the observed correlation for candidates between the transverse momentum of the Zs and the ΔR of the two leptons forming the pair. Figure 4.6 shows the observed correlation for $ZZ \to \ell^- \ell^+ \ell^- \ell^+$ candidates between the invariant mass of the four lepton system M^{ZZ} and the minumum ΔR of the two leptons forming the pair.

---

[1]From here on ZZ will indicate the selection with both on-shell Z, while ZZ^{*} the case where one of the Z is allowed to be off-shell.

ZZ→4μ candidate in 7 TeV collisions
primary Z mass : 89.18 GeV
$p_T(\mu_1)$ = 61.60 GeV
$p_T(\mu_2)$ = 25.68 GeV
secondary Z mass : 88.03 GeV
$p_T(\mu_3)$ = 42.69 GeV
$p_T(\mu_4)$ = 38.60 GeV

Run Number: 183602, Event Number: 282919
Date: 2011-06-18, 06:36:40 CET
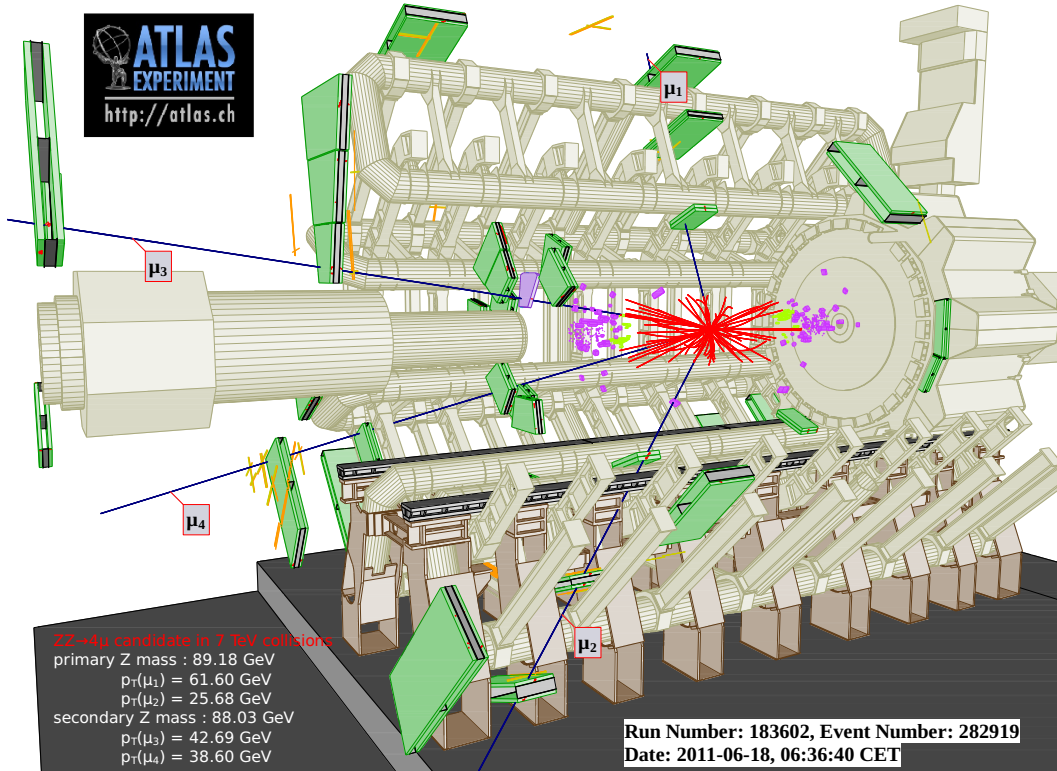
Figure 4.1: Event display of a $ZZ \rightarrow \mu^+ \mu^- \mu^+ \mu^-$ candidate event (Run Number 183602, Event Number 282919). One Z candidate has a mass of 89.18 GeV and a p_T of 36.04 GeV and it is formed by two muons (μ1,μ2) with p_T , η, ϕ of 61.60 GeV, -0.89, -2.11 rad and 25.68 GeV, 0.09, 1.10 rad, respectively. The other Z candidate has a mass of 88.03 GeV and a pT of 46.39 GeV and it is formed by two muons (μ3,μ4) with p_T , η, ϕ of 42.69 GeV, -2.55, 1.39 rad and 38.60 GeV, -1.23, -0.54 rad, respectively. The four lepton system has a mass of 239.69 GeV and a p_T of 21.99 GeV.
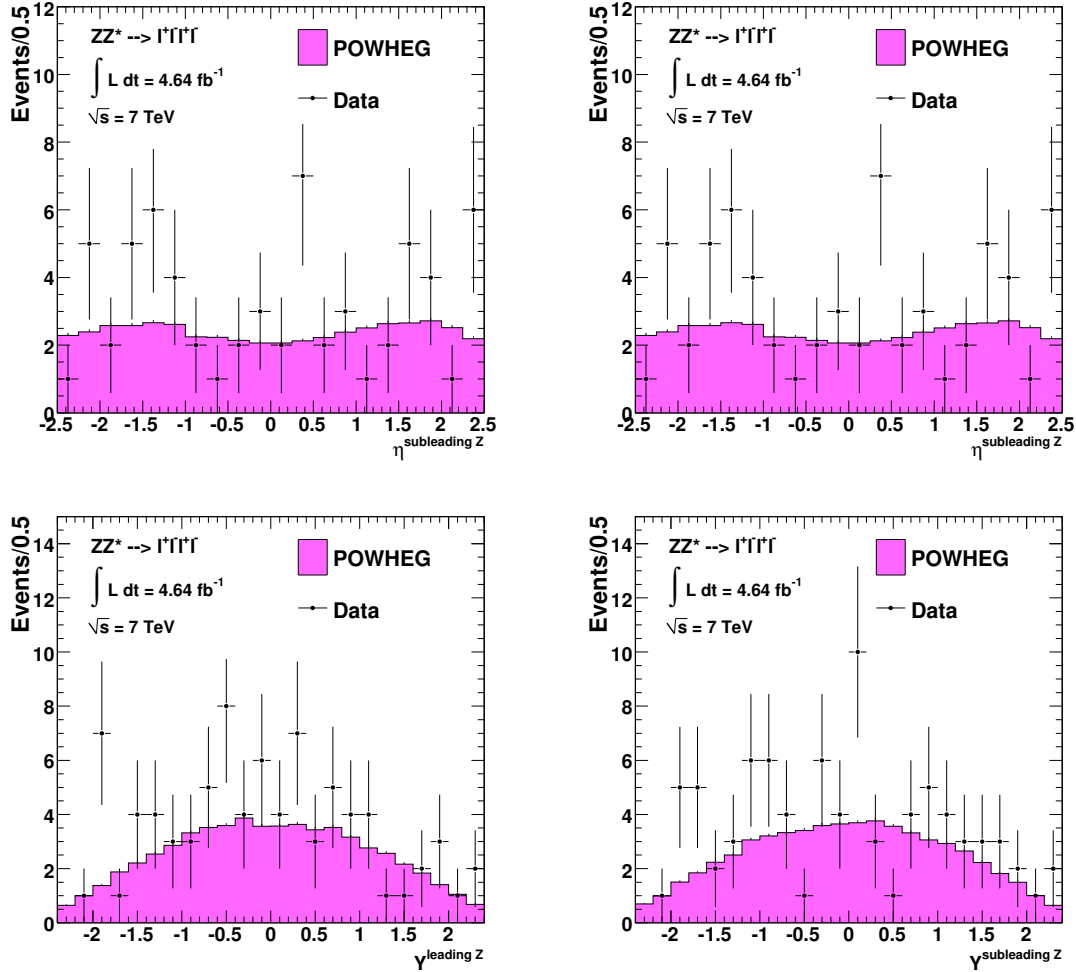
Figure 4.2: The top row shows the pseudorapidity η distributions of the leading (left) and the subleading (right) Z of the ZZ^* candidates. In the same way the rapidity Y is shown in the bottom row.
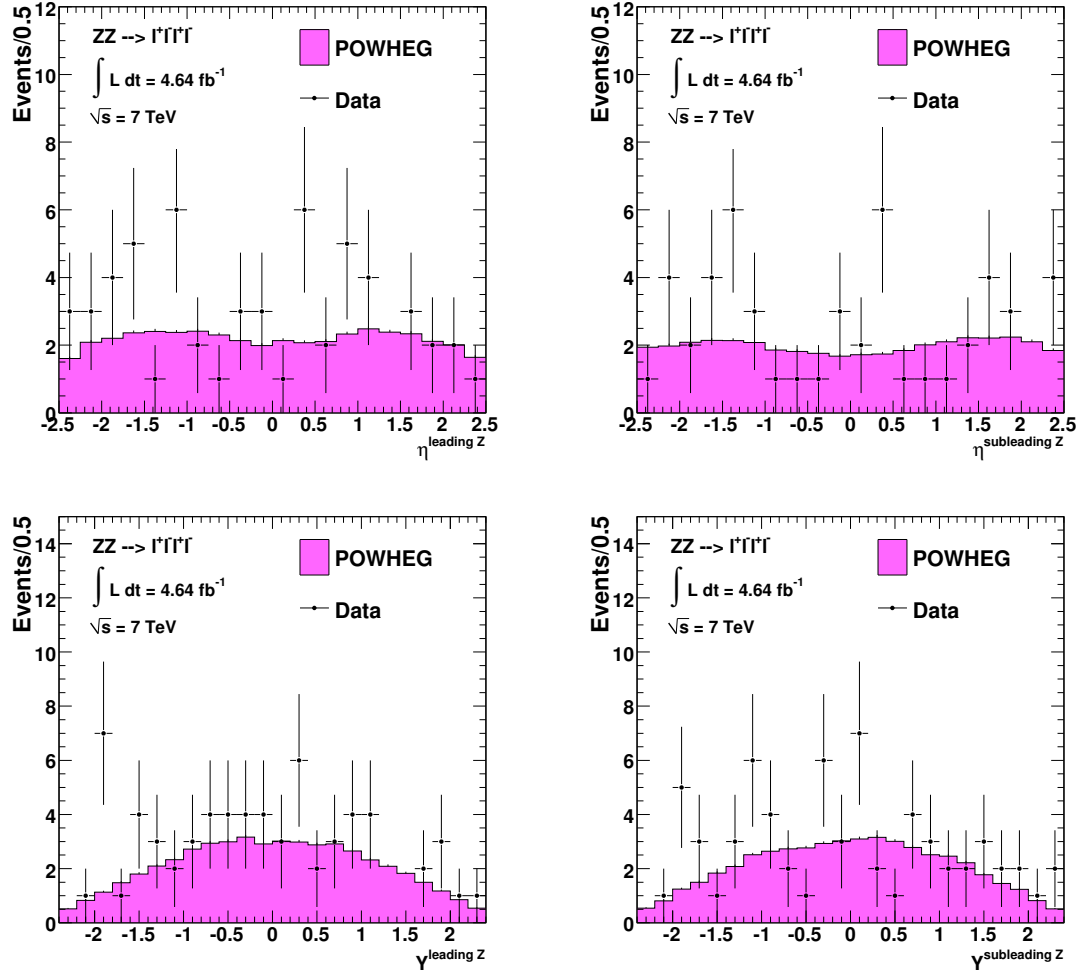
Figure 4.3: The top row shows the pseudorapidity η distributions of the leading (left) and the subleading (right) Z of the ZZ candidates. In the same way the rapidity Y is shown in the bottom row.
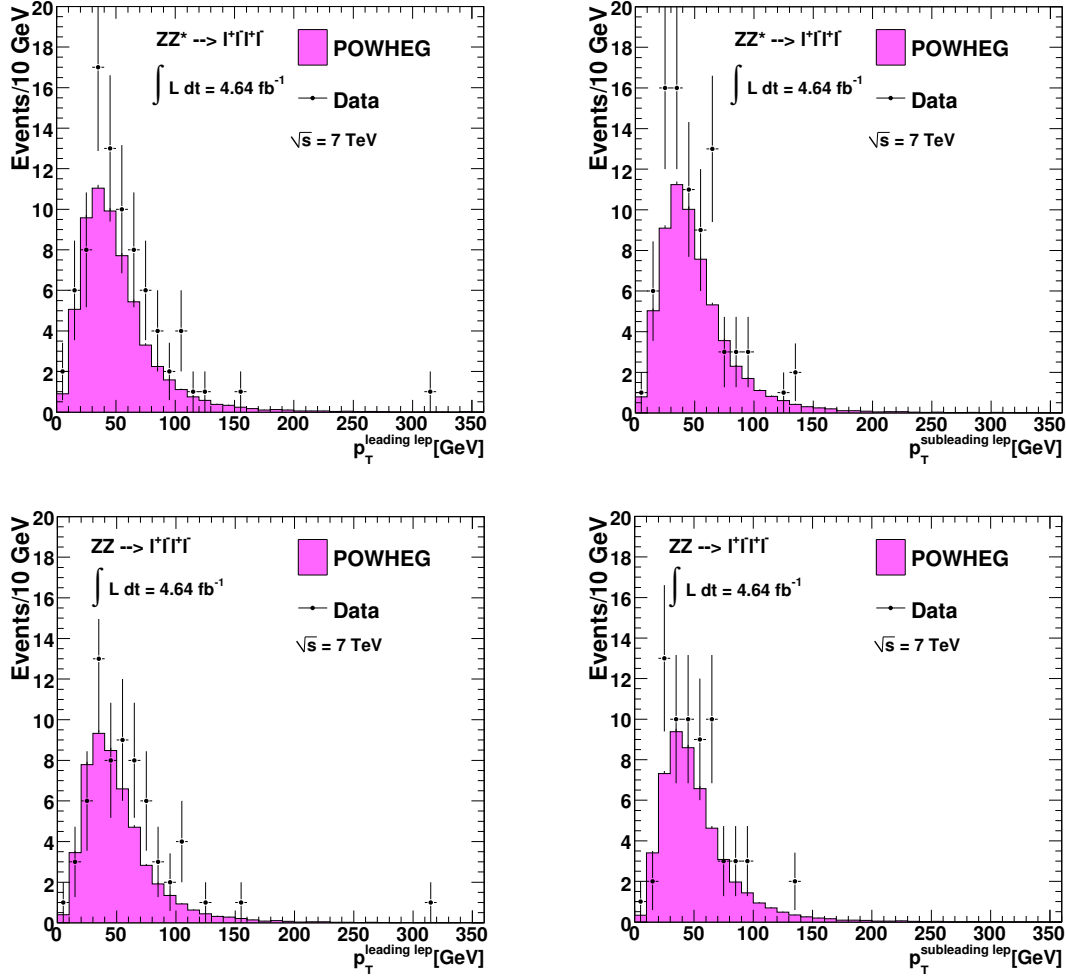
Figure 4.4: The top row shows the p_T distributions of the leading (left) and the subleading (right) leptons of the leading Z for ZZ^* candidates. The same lepton p_T distributions are shown for ZZ candidates in the bottom row.
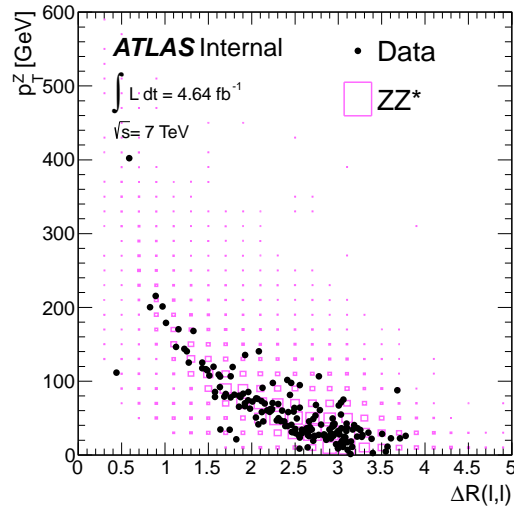
Figure 4.5: The p_T of the Z candidate versus the ΔR of the two leptons forming the pair. The events observed in the data are shown as black dots and the signal prediction as boxes.
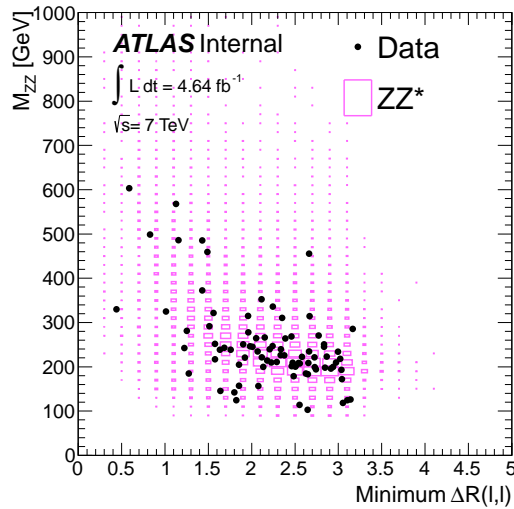
Figure 4.6: The invariant mass of the four lepton system M^{ZZ} versus the minimum ΔR between leptons forming the Z pairs. The events observed in the data are shown as black dots and the signal prediction as boxes.

Chapter 5

$ZZ \to \ell^- \ell^+ \ell^- \ell^+$ Production Cross Section Determination

5.1 Introduction

In this chapter the first main topic of this thesis is presented. ZZ total cross section measurement together with other two cross sections in a restricted 'fiducial' phase space for the $\ell^- \ell^+ \ell^- \ell^+$ final state are discussed. The first when both Z's are required to be on-shell, and the second where one Z is allowed to be off shell, i.e. the ZZ^* case.

As already reported in **Chapter 2** using the CT10 [19] PDF set the total cross section for on-shell ZZ production at NLO calculated with MCFM [15] is $5.89^{+0.22}_{-0.18}$ pb. MCFM calculation includes the gluon-gluon contribution to ZZ production. The reported uncertainties arise from the choice of the renormalisation and factorisation scales ($\mu_\mathrm{R} = \mu_\mathrm{F}$) and from the uncertainty in the chosen PDF. They are assessed by repeating the calculations with $\mu_\mathrm{R} = \mu_\mathrm{F} = 0.5 m_{ZZ}$ and $\mu_\mathrm{R} = \mu_\mathrm{F} = 2 m_{ZZ}$ and compared to the nominal $\mu_\mathrm{R} = \mu_\mathrm{F} = m_{ZZ}$ and using the 52 error sets of the CT10 PDFs.

First, the total and "fiducial" cross section definitions will be given in section 5.2, then acceptance values and systematic uncertainties on the cross section measurements are described in sections 5.3, 5.4 and summarized in section 5.5. The background estimation is reported in section 5.6, the distributions of the selected candidates are shown in section 5.7 and finally the cross section results are calculated in section 5.8.

5.2 Fiducial and Total Cross Section Definition

The fiducial cross sections are defined such that they correspond closely to the experimental selection cuts in a particular final state. They are therefore free from any systematic errors that arise from extrapolating to regions of phase space which are not measured.

In our case the $ZZ \to \ell^-\ell^+\ell^-\ell^+$ on-shell (ZZ) fiducial volume is defined by the following cuts:

- $ZZ \to \ell^+\ell^-\ell^+\ell^-$, $\ell = e, \mu$, where each Z decays to a particle-antiparticle pair of a given lepton flavor, i.e. $Z \to e^-e^+$ or $Z \to \mu^-\mu^+$;

- $66 < m_{12}(Z) < 116$ GeV, where $m_{12}(Z)$ is the mass of the Z reconstructed from the first and second leptons. The same-flavor, opposite-sign lepton pairings are chosen such that the mass of the reconstructed Z is closest to the PDG value of the Z mass;

- $66 < m_{34}(Z) < 116$ GeV, where $m_{34}(Z)$ is the mass of the Z reconstructed from the third and fourth leptons;

- Transverse momentum of leprons: $p_T^\ell > 7$ GeV;

- Leptons pseudorapidity range: $|\eta^\ell| < 3.16$.

- Minimum ΔR ($\Delta R = \sqrt{\Delta\eta^2 + \Delta\phi^2}$) between any two out of the four selected leptons in the event to be greater than 0.2: $\min(\Delta R(\ell, \ell)) > 0.2$.

The second fiducial volume, allowing one Z to be off-shell (ZZ^*), is defined as:

- $ZZ^* \to \ell^+\ell^-\ell^+\ell^-$, $\ell = e, \mu$;

- $66 < m_{12}(Z) < 116$ GeV;

- $m_{34}(Z^*) > 20$ GeV;

- $p_T^\ell > 7$ GeV;

- $|\eta^\ell| < 3.16$.

- $\min(|\Delta R(\ell, \ell)|) > 0.2$.

For a given $ZZ^{(*)} \to \ell^-\ell^+\ell^-\ell^+$ sub-channel where $\ell \in \{e, \mu\}$, the fiducial cross section [1] is defined:

$$\sigma_{ZZ^{(*)} \to \ell^-\ell^+\ell^-\ell^+}^{fid} = \frac{N_{\ell^-\ell^+\ell^-\ell^+}^{obs} - N_{\ell^-\ell^+\ell^-\ell^+}^{bkg}}{\mathcal{L} \times C_{ZZ^{(*)} \to \ell^-\ell^+\ell^-\ell^+}} \tag{5.1}$$

---

[1]The subscript $\ell^-\ell^+\ell^-\ell^+$ in the fiducial cross section formula means that it is multiplied by the specific channel Branching Ratio, i.e: $\sigma_{ZZ^{(*)} \to \ell^-\ell^+\ell^-\ell^+}^{fid} = \sigma_{ZZ^{(*)}}^{fid} \times BR_{comb}(ZZ^{(*)} \to \ell^-\ell^+\ell^-\ell^+)$.

Here, $N^{obs}_{\ell^-\ell^+\ell^-\ell^+}$ and $N^{bkg}_{\ell^-\ell^+\ell^-\ell^+}$ denote the number of observed and background events respectively, $\mathcal{L}$ is the luminosity and $C_{ZZ^{(*)} \to \ell^-\ell^+\ell^-\ell^+}$ is the correction factor defined in section 5.3.

In addition to the fiducial cross section, we also calculate a production cross section in the total phase space volume for the ZZ case only. The ZZ total production cross-section is calculated as:

$$\sigma^{tot}_{ZZ} = \frac{N^{obs}_{\ell^-\ell^+\ell^-\ell^+} - N^{bkg}_{\ell^-\ell^+\ell^-\ell^+}}{\mathcal{L} \times BR_{comb}(ZZ \to \ell^-\ell^+\ell^-\ell^+) \times A_{ZZ \to \ell^-\ell^+\ell^-\ell^+} \times C_{ZZ \to \ell^-\ell^+\ell^-\ell^+}} \quad (5.2)$$

where $A_{ZZ \to \ell^-\ell^+\ell^-\ell^+}$ is the correction factor defined in section 5.4 which represents the fiducial cuts efficiency. The specific-channel branching ratio $BR(ZZ \to \ell^-\ell^+\ell^-\ell^+)$ for both Z decaying in leptons is $[BR(ZZ \to \ell^-\ell^+\ell^-\ell^+)]^2 = [0.03366]^2$ per channel [1]. The summation of all possible combinations ($eeee, \mu\mu\mu\mu$ and $ee\mu\mu$, where the last counts 2) gives a combined branching fraction $BR_{comb}(ZZ \to \ell^-\ell^+\ell^-\ell^+) = 4 \times 0.033662^2 = 0.004532$.

5.3 Fiducial Acceptance Definition

The primary purpose of using the fiducial cross section defined in Eq. 5.1 is to correct the reconstructed-level cross section to a truth-level cross section defined by a fiducial volume corresponding to the volume in which the measurement is performed. The reason to only correct to a fiducial volume is that this correction will be less sensitive to purely theoretical uncertainties like the PDF set used. This correction essentially gives the probability of reconstructing an event, given that all the objects in the event would have been in the detector and passed our selection level cuts.

C_{ZZ} in Eq. 5.1 is defined as:

$$C_{ZZ} = \epsilon_{trig} \times \epsilon_{event} \times \epsilon_{lep} \times \alpha_{reco} \quad (5.3)$$

where ϵ_{trig} is the trigger efficiency, ϵ_{event} is the efficiency of the event level cuts (like the primary vertex cut, etc.), ϵ_{lep} is the product of the individual efficiencies for the four leptons to pass the lepton object selection cuts, and finally α_{reco} is the reconstruction to generator-level fiducial volume correction which also includes smearing corrections and resolutions. C_{ZZ} is calculated separately for each channel by applying the necessary MC with respect to data corrections to the signal $ZZ \to \ell^-\ell^+\ell^-\ell^+$ MC (such as smearing, pileup reweighting, reconstruction scale factors, etc.) and finding the ratio of the number of events which pass the reconstruction level cuts to the number of events which pass the fiducial volume cuts at the generator level. Thus,

$$C_{ZZ} = \frac{N_{\text{Reconstructed } ZZ}^{\text{MC Pass All Cuts}} \times \text{SF}}{N_{\text{Generated } ZZ}^{\text{MC Fiducial Volume}}} \quad (5.4)$$

where the scale factor (SF) is applied on an event-by-event level. The SF (see section 5.3.1) is used to correct for discrepancies in trigger efficiency and reconstruction efficiency between data and MC in the $ZZ \to \ell^-\ell^+\ell^-\ell^+$ channel and is defined as

$$SF = \frac{\epsilon_{trig}^{data}}{\epsilon_{trig}^{MC}} \cdot \frac{\epsilon_{reco}^{data}}{\epsilon_{reco}^{MC}} \quad (5.5)$$

with $\epsilon_{reco} = \epsilon_{lep} \cdot \epsilon_{event}$. Since the selection cuts for electrons and muons are different, the fiducial volume corresponding to exactly our selection cuts for each $ZZ \to \ell^-\ell^+\ell^-\ell^+$ sub-channels are also different. In order to calculate a combined fiducial cross section, we would need to first perform an additional extrapolation to a common fiducial volume and then extract a combined cross section in the combined volume.

The fiducial acceptance (C_{ZZ}) calculation and comparison between various generators is reported in Tab. 5.1. Values are shown for both ZZ and ZZ^* selections in the three different dacay channels and in the combined one with only associated statistical uncertainty.

$ZZ \to \ell^-\ell^+\ell^-\ell^+$ Channel, ZZ^* Selection				
Generator	$e^+e^-e^+e^-$	$\mu^+\mu^-\mu^+\mu^-$	$e^+e^-\mu^+\mu^-$	combined
Sherpa	0.420 ± 0.004	0.682 ± 0.004	0.536 ± 0.003	0.544 ± 0.002
Pythia	0.413 ± 0.004	0.689 ± 0.004	0.543 ± 0.003	0.547 ± 0.002
PowhegBox	0.408 ± 0.004	0.674 ± 0.004	0.537 ± 0.003	0.539 ± 0.002
gg2zz	0.457 ± 0.002	0.761 ± 0.002	0.589 ± 0.002	0.600 ± 0.001
PowhegBox + gg2zz	0.410 ± 0.004	0.679 ± 0.004	0.540 ± 0.003	0.542 ± 0.002
$ZZ \to \ell^-\ell^+\ell^-\ell^+$ Channel, ZZ Selection				
Generator	$e^+e^-e^+e^-$	$\mu^+\mu^-\mu^+\mu^-$	$e^+e^-\mu^+\mu^-$	combined
Sherpa	0.437 ± 0.004	0.689 ± 0.004	0.550 ± 0.003	0.557 ± 0.002
Pythia	0.425 ± 0.004	0.695 ± 0.004	0.549 ± 0.003	0.555 ± 0.002
PowhegBox	0.426 ± 0.005	0.682 ± 0.004	0.543 ± 0.003	0.549 ± 0.002
gg2zz	0.466 ± 0.002	0.765 ± 0.002	0.596 ± 0.002	0.606 ± 0.001
PowhegBox + gg2zz	0.428 ± 0.005	0.687 ± 0.004	0.546 ± 0.003	0.552 ± 0.002

Table 5.1: Fiducial acceptance, C_{ZZ}, comparisons between various generators. The top section of the table shows C_{ZZ} for the $ZZ \to \ell^-\ell^+\ell^-\ell^+$ channel with the ZZ^* selection, while the bottom section with the ZZ selection. Only statistical uncertainties are shown.

5.3.1 Efficiency Correction Scale Factors

To correct for discrepancies in trigger, reconstruction and identification efficiency between data and MC, performance groups provide scale factors to be applied on event-by-event level in the lepton selection.

MC events are also re-weighted to account for any difference in the number of pileup vertices in the data and MC samples. The pileup re-weighting makes the distribution of MC events as a function of the number of reconstructed primary vertices similar to the distribution observed in data. The change of pileup condition during data and the different states of the detector response are also modeled in the official ATLAS pileup reweighting tool. The overall event-level scale factors resulting from the corrections are given in Tab. 5.2.

Channel	Overall Scale Factor	
	ZZ	ZZ^*
$\ell^-\ell^+\ell^-\ell^+$	0.9672	0.9653
$e^+e^-e^+e^-$	0.9523	0.9475
$\mu^+\mu^-\mu^+\mu^-$	0.9807	0.9804
$e^+e^-\mu^+\mu^-$	0.9646	0.9629

Table 5.2: Overall event level scale-factors (the results of applying the scale factors to all the relevant objects in an event) applied to the MC, split by decay channel. The overall scale-factors correct for muon identification efficiency, electron reconstruction and identification efficiencies and trigger efficiency.

The systematics of scale-factors correction for muon identification efficiency, electron reconstruction and identification efficiencies is treated in section 5.3.2, while here is described more in depth the trigger case.

The scale factors to account for the mis-modeling of the single-lepton trigger efficiency in the MC with respect to the data have been derived using the tag-and-probe method (T&P) on $Z \to \ell^+\ell^-$ events. The scale factors are applied to leptons forming the Z candidate which match to a trigger object as described above. The scale factor depends on the lepton flavor and p_T of the individual leptons. It is calculated according to Eq. 5.6 where N_l is the number of leptons matching to a trigger object, ϵ_{Data,l_n} is the trigger efficiency determined with T&P from data for a single lepton flavor of lepton l_n, and ϵ_{MC,l_n} is the trigger efficiency determined with T&P from MC.

$$SF = \frac{1 - \prod_{n=1}^{N_l}(1 - \epsilon_{Data,l_n})}{1 - \prod_{n=1}^{N_l}(1 - \epsilon_{MC,l_n})} \tag{5.6}$$

The systematic uncertainty associated with the scale factors for muon triggers

is 0.2%, while the one associated with the electron trigger is 1%, which are given by muon and e-gamma performances group respectively.

The trigger efficiencies determined with the ZZ MC samples after the selection cuts except for the trigger object-lepton matching and the triggered-object requirement are listed in Tab. 5.3.

Channel	Trigger Efficiency [%]	
	ZZ Selection	ZZ^*Selection
$eeee$	$100.0^{+0.0}_{-0.4}$	$99.6^{+0.2}_{-0.5}$
$\mu\mu\mu\mu$	$98.7^{+0.4}_{-0.6}$	$98.2^{+0.4}_{-0.5}$
$ee\mu\mu$	$99.6^{+0.2}_{-0.3}$	$98.8^{+0.3}_{-0.4}$
$llll$	$99.4^{+0.2}_{-0.2}$	$98.8^{+0.2}_{-0.2}$

Table 5.3: Trigger efficiencies for ZZ events after all selection cuts excluding the trigger match and trigger requirement.

The systematic uncertainty associated to trigger SF is reported in the summary table Tab.5.8. It is evaluated by summing in quadrature the statistical uncertainty obtained from MC and the systematic error of the efficiency.

5.3.2 Systematic Uncertainties on C_{ZZ}

The main sources of systematics on the cross section measurement arises from the electron and muon object reconstruction and identification.

Electrons

The systematic uncertainties coming from electron object are summarized in Tab. 5.4. The uncertainty values used are those provided by the ATLAS performance group.

- **Reconstruction and Identification Efficiency:** The differences observed in the reconstruction and identification efficiencies between the data and MC are taken into account by weighting the simulation with scale factors provided by the egamma group. The systematic uncertainties are then determined by varying the scale factors within their quoted uncertainties ($\pm 1\sigma$). The electron identification efficiency scale factors and their uncertainties are determined from W and Z T&P measurements and are given as a function of η, E_T, and electron algorithm (loose, medium, etc.). The uncertainties of the η and E_T dependent scale factors are added in quadrature to obtain the combined electron identification uncertainty. A similar procedure is followed for the extraction of the scale factors related to reconstruction efficiency.

- **Energy Scale:** The systematic uncertainties on the energy scale derived from the 2011 dataset and implemented in the official ATLAS tool provided by the e-gamma group are used on the Monte Carlo to obtain the associated uncertainty on the signal acceptance.

- **Energy Smearing:** Since the MC does not reproduce the observed energy resolution in data, a smearing is applied to it. The systematic uncertainties associated with the smearing procedure are obtained from the official ATLAS tool provided by the e-gamma performance group.

- **Electron Isolation and Impact Parameter:** The uncertainties are assigned by the Higgs to ZZ analysis [66]. For electrons with p_T less than 15 GeV they are found to be 5%, for 15-20 GeV 2%, for 20-35 GeV 1% and for p_T above 35 GeV, the uncertainty is less than 1%.

Source %	$eeee$		$ee\mu\mu$	
C_{ZZ} **Uncertainties**	ZZ	ZZ^*	ZZ	ZZ^*
e energy resolution	< 0.1	< 0.1	< 0.1	< 0.1
e energy scale	0.5	0.6	0.1	0.1
e identification efficiency	5.5	6.0	2.7	2.8
e reconstruction	3.9	4.0	1.9	2.0
e isolation/z0/d0Sig	3.3	3.6	1.6	1.7
Total (C_{ZZ})	**7.5**	**8.1**	**3.7**	**3.8**

Table 5.4: Systematic uncertainties of electrons considered in the cross-section calculation.

Muons

The systematic uncertainties coming from muon objects are similar to the electrons and they are summarized in Tab. 5.5.

They are of three types:

- **Reconstruction efficiency:** The event yields are computed while varying efficiency scale factor applied to MC following the recommendations of the muon performance group for 2011 data [65]. The event number variations are symmetrical around the nominal values.

- p_T **smearing and scale:** The momentum scale correction is turned off as a conservative systematic estimate of the uncertainty in the scale correction.

The smearing uncertainty is calculated by varying the MC muon p_T smearing, according to the uncertainty on muon p_T observed in data. This smearing uncertainty is estimated separately for Inner Detector parameter variation and Muon Spectrometer parameter variation. As a conservative estimate the absolute value of the maximum variation between lower and higher smearing is taken as the systematic uncertainty.

- **Muon Isolation and Impact Parameter:** In analogy with the electron case the uncertainties are assigned by the Higgs to ZZ analysis [66]. For muons with p_T less than 15 GeV they are found to be 2%, for 15-20 GeV 1% and for p_T above 20 GeV, the uncertainty is less than 1%.

Source %	$\mu\mu\mu\mu$		$ee\mu\mu$	
C_{ZZ} **Uncertainties**	ZZ	ZZ^*	ZZ	ZZ^*
μ momentum resolution	< 0.1	< 0.1	< 0.1	< 0.1
μ momentum scale	< 0.1	< 0.1	< 0.1	< 0.1
μ reconstruction efficiency	1.2	1.2	0.6	0.6
μ isolation/z0/d0Sig	2.2	2.4	1.1	1.2
Total (C_{ZZ})	**2.5**	**2.7**	**1.3**	**1.3**

Table 5.5: Systematic uncertainties of muons considered in the cross-section calculation.

5.4   Total Acceptance Definition

In order to calculate a total cross section, one must correct the reconstruction level cross section to full phase space of possible truth level quantities. This is performed by applying a correction from the fiducial volume to the full phase space at truth-level. This correction is defined as A_{ZZ} and is calculated as

$$A_{ZZ} = \frac{N_{\text{Generated } ZZ}^{\text{MC Fiducial Volume}}}{N_{\text{Generated ZZ}}^{\text{MC All}}} \tag{5.7}$$

In analogy with C_{ZZ}, A_{ZZ} is calculated for each channel separately and the results are shown in Tab. 5.6.

The uncertainty on the correction from the fiducial cross section to the total cross section come from PDF uncertainty, and it is assessed by varying the PDF set, the factorisation and renormalization scales and taking the weighted difference with the correction calculated with a $gg \rightarrow ZZ$ generator.

$ZZ \to \ell^-\ell^+\ell^-\ell^+$ Channel, ZZ^* Selection				
Generator	$e^+e^-e^+e^-$	$\mu^+\mu^-\mu^+\mu^-$	$e^+e^-\mu^+\mu^-$	combined
MCFM			0.755 ± 0.002	0.755 ± 0.002
PowhegBox	0.745 ± 0.001	0.745 ± 0.001	0.749 ± 0.001	0.747 ± 0.001
gg2zz	0.919 ± 0.004	0.919 ± 0.004	0.919 ± 0.004	0.919 ± 0.003
PowhegBox + gg2zz	0.755 ± 0.001	0.755 ± 0.001	0.758 ± 0.001	0.757 ± 0.001
$ZZ \to \ell^-\ell^+\ell^-\ell^+$ Channel, ZZ Selection				
Generator	$e^+e^-e^+e^-$	$\mu^+\mu^-\mu^+\mu^-$	$e^+e^-\mu^+\mu^-$	combined
MCFM			0.795 ± 0.001	0.795 ± 0.001
PowhegBox	0.796 ± 0.001	0.796 ± 0.001	0.796 ± 0.001	0.796 ± 0.001
gg2zz	0.932 ± 0.004	0.932 ± 0.004	0.932 ± 0.004	0.932 ± 0.004
PowhegBox + gg2zz	0.804 ± 0.001	0.804 ± 0.001	0.804 ± 0.001	0.804 ± 0.001

Table 5.6: Acceptance A_{ZZ} comparison between different generators. The table shows A_{ZZ} for the $ZZ \to \ell^-\ell^+\ell^-\ell^+$ channels for both ZZ (top) and ZZ^* (bottom) selections.

The uncertainty on the total acceptance A_{ZZ} was estimated by shifting the factorization and renormalization scales up and down by a factor of two and by determining the uncertainty with the 52 CT10 error sets. Adding them in quadrature, the total PDF and scale uncertainty is 0.6%. An additional 1.1% uncertainty due to initial state radiation, final state radiation and underlying event modeling is evaluated by comparing the acceptance in MCFM [15] and PowhegBox [11]. This difference is found to be 1.1%. The total systematics uncertainty of the fiducial-to-total phase-space acceptance correction is therefore 1.3% as reported in the summary table Tab. 5.8.

5.5   Summary of Acceptance Values and Systematic Uncertainties

In Tab. 5.7 final combined expected correction factors A_{ZZ} and C_{ZZ} for the ZZ and ZZ^* selection are reported. A complete summary of the acceptance (C_{ZZ} and A_{ZZ}) systematic uncertainties used in the cross section measurement is shown in Tab. 5.8. It includes C_{ZZ} systematics from leptons object selection (see Tab. 5.4 and Tab. 5.5) and acceptance (C_{ZZ} and A_{ZZ}) theoretical systematics uncertainty evaluation arising from PDF and scale uncertainties and for the differences between various generators (see Tab. 5.6 and Tab. 5.1). In addition trigger systematics uncertainty, evaluated as reported in section 5.3.1 and luminosity uncertainty as discussed in section 3.5.5 of **Chapter 3** are also shown.

$\ell^-\ell^+\ell^-\ell^+$ channel	A_{ZZ}	C_{ZZ}
ZZ^* Selection	$0.757 \pm 0.001 \pm 0.019$	$0.542 \pm 0.002 \pm 0.022$
ZZ Selection	$0.804 \pm 0.001 \pm 0.010$	$0.552 \pm 0.002 \pm 0.021$

Table 5.7: Expected correction factors (A_{ZZ} for the fiducial-to-total acceptance and C_{ZZ} for the fiducial reconstruction) for the ZZ and ZZ^* selection. The first uncertainty is statistical and the second is systematic.

Source %	$eeee$		$\mu\mu\mu\mu$		$ee\mu\mu$		$llll$	
Reconstruction Uncertainties	ZZ	ZZ^*	ZZ	ZZ^*	ZZ	ZZ^*	ZZ	ZZ^*
e energy resolution	< 0.1	< 0.1	-	-	< 0.1	< 0.1	< 0.1	< 0.1
e energy scale	0.5	0.6	-	-	0.1	0.1	0.1	0.2
e identification efficiency	5.5	6.0	-	-	2.7	2.8	2.4	2.5
e reconstruction	3.9	4.0	-	-	1.9	2.0	1.7	1.7
e isolation/z0/d0Sig	3.3	3.6	-	-	1.6	1.7	1.4	1.5
μ momentum resolution	-	-	< 0.1	< 0.1	< 0.1	< 0.1	< 0.1	< 0.1
μ momentum scale	-	-	< 0.1	< 0.1	< 0.1	< 0.1	< 0.1	< 0.1
μ reconstruction efficiency	-	-	1.2	1.2	0.6	0.6	0.7	0.7
μ isolation/z0/d0Sig	-	-	2.2	2.4	1.1	1.2	1.3	1.3
IP Resolution	< 0.1	< 0.1	0.4	0.4	0.3	0.3	0.3	0.3
Trigger	< 0.1	< 0.1	0.3	0.4	0.1	0.2	0.2	0.2
Total Reconstruction Uncertainty (C_{ZZ})	7.5	8.1	2.6	2.7	3.9	4.1	3.5	3.7
Theoretical Uncertainties	ZZ				ZZ^*			
MC Generator Difference (C_{ZZ})	1.6				1.5			
PDF & Scale (A_{ZZ})	0.6				2.5			
MC Generator Difference (A_{ZZ})	1.1				0.2			
Total (A_{ZZ})	1.3				2.5			
Total (C_{ZZ})	7.7	8.3	3.0	3.1	4.2	4.3	3.9	4.0
Luminosity	3.9							

Table 5.8: Summary of all relative acceptance uncertainties considered in the cross-section calculation for the $ZZ \to \ell^-\ell^+\ell^-\ell^+$ channel. Sums in quadrature of the weighted average of the three channels and a combined uncertainty are shown. Luminosity uncertainty is also shown.

5.6 $ZZ \rightarrow \ell^-\ell^+\ell^-\ell^+$ Backgrounds Estimation

ZZ production with subsequent dacay to four charged leptons is a rare SM process where the main background contributions are Z+jet, $Zb\bar{b}$, $Z+\gamma$+jet, and top decays ($t\bar{t}$ and single top). Such background processes have two prompt leptons from W and Z decays, and two "fake" leptons (from charged hadrons faking an electron or a muon) or leptons from heavy flavour decays. Additional background arise from diboson WZ+jet (and WW+jets) events containing three (two) prompt leptons and one (two) fake lepton. Since the $ZZ \rightarrow 4\ell$ is the only SM process with four prompt leptons in the final state, all background processes have at least one fake lepton, and can be estimated using the data-driven approach.

5.6.1 Data-driven Estimation

ZZ signal events contain isolated, prompt leptons from a vector-boson decay while leptons from the background sources mentioned above tend to be spatially correlated with jets. While the majority of these leptons will fail the isolation requirement, the tails of the jet distributions may have electrons or muons which satisfy the isolation and identification requirements.

Since the tails of jet fragmentation is not well model by Monte Carlo predictions, better estimates of event yields for this kind of backgrounds can be calculated directly from data. To estimate the background contribution of four-lepton events in which at least one lepton does not originate from a Z decay, we identify a sample of events in the data adjacent to the signal region but dominated by this type of background, by inverting some of the identification requirements. We extrapolate to the signal region using an extrapolation factor (a "fake factor", FF) measured in this background sample.

Fake Faktors Calculation

To derive the fake factors, we identify "pre-lepton" objects by applying nearly all the lepton selection requirements, but reserve a few requirements for a second stage. The pre-leptons are then classified either as "selected leptons" (denoted by "L"), if they pass all the remaining requirements at the second selection stage, or as "lepton-like jets" (denoted by "J"), if they fail some of the remaining requirements at the second selection stage. These requirements depend on whether the lepton is an electron or a muon (see Tab. 5.9). For muons, the "J" are muon candidates that fail the isolation requirement or fail the impact parameter requirement but not both. For electrons with $|\eta| < 2.47$, the lepton-like jets are clusters in the electromagnetic calorimeter matched to inner detector tracks that fail either the full electron selection or the isolation requirement but not both. For electrons with

	Selected leptons	Lepton-like jets
Muons	Track iso < 0.15	(d_0-significance > 3.5 and Track iso < 0.15 and Calo iso < 0.30)
	and Calo iso < 0.30	or (d_0-significance < 3.5 and (Track iso > 0.15 or Calo iso > 0.30)
	and d_0-significance < 3.5	
Electrons	Track iso < 0.15	(!Loose++ and Track iso < 0.15 and Calo iso < 0.30)
	and Calo iso < 0.30	or (Loose++ and Track iso > 0.15 and Calo iso > 0.30)
	and Loose++	
Forward		
Electrons	Tight	!Tight

Table 5.9: Summary of requirements for selected leptons and lepton-like jets.

$|\eta| > 2.5$, the lepton-like jets are electromagnetic clusters that are reconstructed as electrons but fail the tight identification requirements.

The regions defined by the cuts are represented visually in Fig. 5.1.
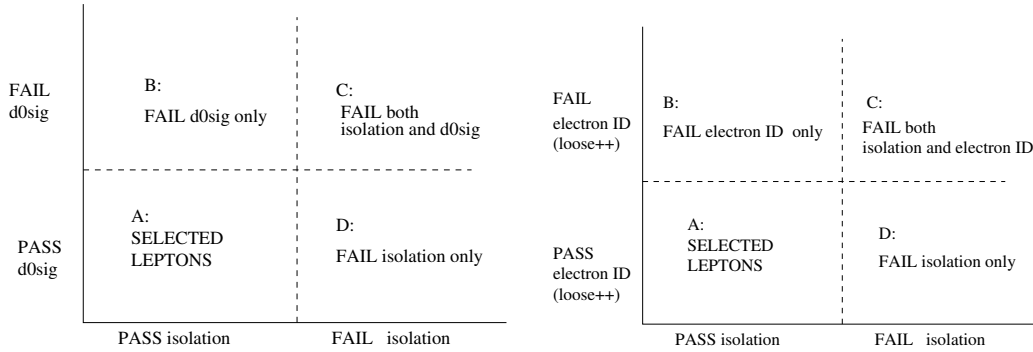
Figure 5.1: Definition of selected leptons and lepton-like jets for muons (left) and electrons (right).

To extrapolate to the signal region, we need to know the fake-factor, the ratio of the number of selected leptons to the number of lepton-like-jets. This fake factor is defined as:

$$FF_{lepton} = \frac{N^{\text{data}}_{\text{selected leptons}} - N^{\text{MC } WZ, ZZ}_{\text{selected leptons}}}{N^{\text{data}}_{\text{lepton-like jets}} - N^{\text{MC } WZ, ZZ}_{\text{lepton-like jets}}} \tag{5.8}$$

To measure the fake-factor, we select a sample of events which have a reconstructed Z and then look for an additional lepton in the event that satisfies either the selected lepton or lepton-like jet requirements. The requirements to categorize the event as "Z-tagged" can be found in Tab. 5.10.

Criteria	Selection
Leptons	Either 2 selected Muons or 2 selected Electrons
Z-reconstruction	oppositely charged leptons
	1 trigger matched lepton
	$|M_{ll} - M_Z| < 20$ GeV
MET	$MET < 25$ GeV

Table 5.10: Summary of requirements to select Z candidate events. The additional leptons in the event, if any, are used to estimate the fake factor for this sample.

The origin of the third lepton in the event is dominated by jets from Z+jets events but can also include leptons from WZ and ZZ. These latter are removed using a MC prediction via the terms $N^{\text{MC } WZ, \, ZZ}_{\text{selected leptons}}$ and $N^{\text{MC } WZ, \, ZZ}_{\text{lepton-like jets}}$.

The fake factor is calculated by subtracting the WZ+ZZ contribution in each histogram from the data to remove the contribution from isolated analysis level leptons which are from an expected source and then dividing the **selected lepton** distributions by the **lepton-like jet** distributions.

In this way, the fake factor distributions parametrized in p_{T} end η are found and are given in Figures 5.2 and 5.3 for central and forward electrons and in Fig. 5.4 for muons. Due to the lack of statistics above 60 GeV for the p_T parametrization, all muon-like jets with $p_T > 60$ GeV used the fake factor for the last filled bin $(50 - 60$ GeV). The fake-factor is applied directly from the histograms assuming no correlation between p_{T} and η, with the equation:

$$FF(p_{\text{T}}, \eta) = \frac{FF(p_{\text{T}}) \times FF(\eta)}{< FF(p_{\text{T}}, \eta) >}, \tag{5.9}$$

where $< FF(p_{\text{T}}, \eta) >$ is the average fake factor in the control samples, averaged over both p_{T} and η.

Fake Lepton Background Formula

The fake lepton background to the four-selected-lepton sample has contributions from events with two fake leptons (F) plus two true leptons (T) and events with one fake lepton plus three true leptons. Thus, we write the number of background events as:

$$N^{\text{fake}}_{4\ell} = N_{TTFF} \times f \times f + N_{TTTF} \times f \tag{5.10}$$

where f is the fraction of fake leptons which are reconstructed as selected leptons. N_{TTTF} events can be WZ+1 jet events, while N_{TTFF} events can be, for example, from Z+2 jets, $t\bar{t}$, tW+1 jet and single top+2 jets.
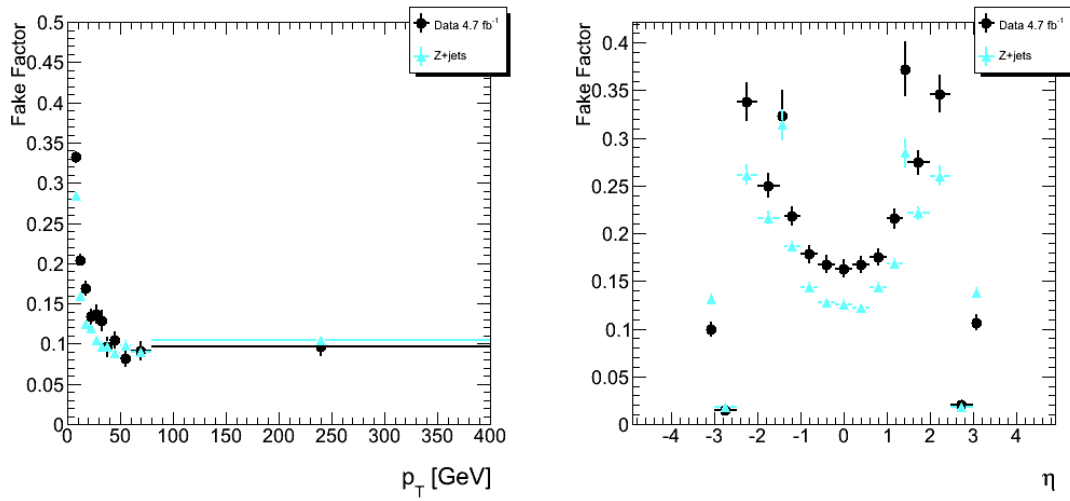
Figure 5.2: Fake Factor distribution for electrons parametrized in p_T, left and η, right.
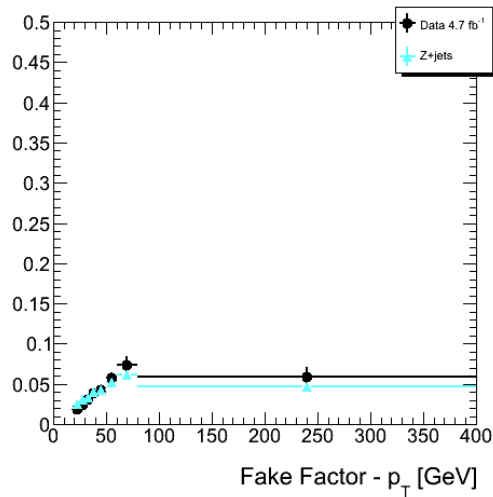
Figure 5.3: Fake Factor distribution for forward electrons parametrized in p_T
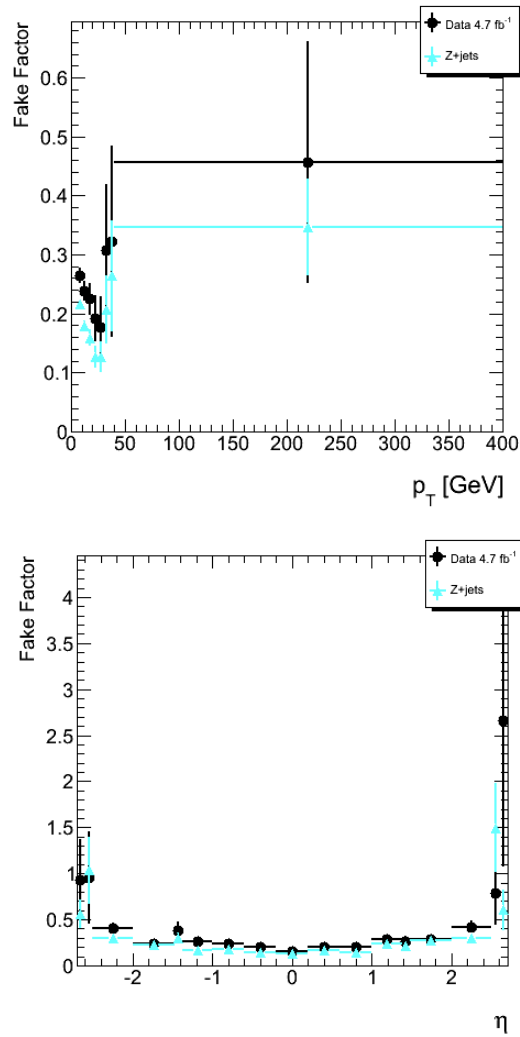
Figure 5.4: Fake Factor distribution for muons parametrized in p_{T}, top and η, bottom.

Denoting selected leptons as L and lepton-like jets as J (as discussed in beginning of section 5.6.1), then the fake factor (FF) and the probability (f) of a fake lepton to be found as selected lepton are

$$f = \frac{L}{L + J} \text{ and } FF = \frac{L}{J} \qquad (5.11)$$

which when combined give:

$$FF = \frac{f}{1 - f} \text{ and } f = \frac{FF}{1 + FF} \qquad (5.12)$$

Events with two selected leptons and two lepton-like jets given as a function of T and F objects can be written:

$$N_{LLJJ} = N_{TTFF} \times (1 - f)^2 \qquad (5.13)$$

Events with three selected leptons and one lepton-like jet, can be ralated to their true composition by writing:

$$N_{LLLJ} = N_{TTFF} \times 2f(1 - f) + N_{TTTF} \times (1 - f) \qquad (5.14)$$

where the factor of 2 is due to combinatorics. Combining these last two equations under the assumption that $L/(L + J) = 1$ for true leptons and correcting for the small contribution (N_{LLLJ}^{ZZ}) from $ZZ \to 4\ell$ events which are reconstructed as $LLLJ$ events, the correct value for the background estimate can be proven to be:

$$N_{4\ell}^{\text{fake}} = (N_{LLLJ} - N_{LLLJ}^{ZZ}) \times FF - N_{LLJJ} \times FF^2 \qquad (5.15)$$

Statistical and Systematic Uncertainties

In the case when $LLJJ$ and $LLLJ$ events are found in the data, the statistical uncertainty can be calculated directly by adding the relative error from the FF applied to those events in quadrature with the relative error on the number of events measured in the channels.

However, if there are no events found, the best estimate is a contribution of zero and we set a 68% confidence level (CL) upper limit on the expected yields corresponding to an upper limit of 1.29 events. This number is then scaled by the FF (evaluated at the p_{T} bin with the largest fake factor), and we quote it as the sigma of a Gaussian truncated at zero.

If the overall $N_{4\ell}^{\text{fake}}$ estimate turns out to be negative, then we quote a truncated Gaussian with mean at zero and sigma equal to the estimated statistical and systematic uncertainties added in quadrature. This is conservative compared to

Ingredients in Eq.5.15	$eeee$	$\mu\mu\mu\mu$	$2e2\mu$	Combined ($\ell\ell\ell\ell$)
$(+)$ $N_{LLLJ} \times FF$	1.63 ± 0.34	0.21 ± 0.21	1.84 ± 0.40	3.67 ± 0.57
$(-)N_{LLJJ} \times FF^2$	0.96 ± 0.10	0.33 ± 0.16	0.83 ± 0.09	2.12 ± 0.21
$(-)ZZ$ correction	0.17 ± 0.13	$0.12^{+0.20}_{-0.12}$	0.34 ± 0.21	0.63 ± 0.32
Fake estimate, $N^{\text{fake}}_{4\ell}$	$0.50^{+0.57}_{-0.50}$(stat)	< 0.64 $[0^{+0.57}_{-0}$(stat)	$0.66^{+0.70}_{-0.66}$(stat)	$0.92^{+1.10}_{-0.92}$(stat)
	± 0.26(syst)	$^{+0.30}_{-0}$(syst)]	± 0.55(syst)	$^{+0.71}_{-0.74}$(syst)

Table 5.11: ZZ fake estimate in 4.6 fb^{-1} of data.

quoting a sigma equal to the estimated uncertainty minus the negative estimate for the mean background value.

As a systematic uncertainty on the fake factor used, we take the largest of the statistical uncertainties and the difference between the fake factor derived in data with that derived in MC (from Alpgen Z+jets samples).

Data-driven Background Estimates

The fake estimates are shown in Tab. 5.11 for on-shell ZZ events and in Tab. 5.12 for ZZ^* events. The total fake background for on-shell ZZ events is

$$0.92^{+1.10}_{-0.92}(\text{stat.})^{+0.71}_{-0.71}(\text{syst.}) \tag{5.16}$$

and for ZZ^* events the total fake background is

$$9.07 \pm 2.32(\text{stat.}) \pm 1.30(\text{syst.}) \tag{5.17}$$

where the systematic uncertainty comes from the statistical and systematic uncertainty on the fake factors. The statistical and systematic errors given for the fake estimates in Tables 5.11 and 5.12 are calculated by coherently fluctuating the ingredients in Eq. 5.15 up and down by one sigma such that the error on the fake estimate is maximized.

5.6.2 Monte Carlo Background Estimations

The MC predictions have high statistical uncertainty and rely on good modeling of leptons in jets, they are used only as a cross-check to nominal data-driven background estimates.

Tab. 5.13 show the MC predictions for the number of events passing the selection requirements for Z+jets, WZ/WW and top-quark ($t\bar{t}$ and single-t) backgrounds in all channels. All numbers are normalised to 4.6 fb^{-1}.

Ingredients in Eq.5.15	$eeee$	$\mu\mu\mu\mu$	$2e2\mu$	Combined ($\ell\ell\ell\ell$)
$(+)\ N_{LLLJ} \times FF$	8.85 ± 0.98	0.21 ± 0.21	10.63 ± 1.06	19.70 ± 1.46
$(-)N_{LLJJ} \times FF^2$	4.24 ± 0.23	1.10 ± 0.31	4.24 ± 0.23	9.58 ± 0.45
$(-)ZZ$ correction	0.29 ± 0.18	$0.20^{+0.25}_{-0.20}$	0.56 ± 0.28	1.05 ± 0.42
Fake estimate, $N_{4\ell}^{\text{fake}}$	$4.33 \pm 1.39(\text{stat})$	$< 0.91\ [0^{+0.77}_{-0}(\text{stat})$	$5.84 \pm 1.57(\text{stat})$	$9.07 \pm 2.32(\text{stat})$
	$\pm 0.62(\text{syst})$	$^{+0.49}_{-0}(\text{syst})]$	$\pm 0.93(\text{syst})$	$\pm 1.29(\text{syst})$

Table 5.12: ZZ^* fake estimate in 4.6 fb^{-1} of data.

The dominant source of background is Z+jets. The MC-based prediction is 1.49 ± 0.37 background events in the $\ell^-\ell^+\ell^-\ell^+$ combined case for the ZZ selection and 8.26 ± 1.30 events for the ZZ^* selection; this is to be compared with the data-driven estimate of $0.92 \pm 1.10 \pm 0.71$ events for the ZZ selection and $9.07 \pm 2.32 \pm 1.30$ events for the ZZ^* selection. Both data-driven and MC background estimations result in good agreement.

Cut	Z+jets	WZ/WW	Top
Four Leptons	34.46 ± 3.40	2.03 ± 0.44	0.27 ± 0.21
Trigger Match	32.96 ± 3.33	2.02 ± 0.44	0.27 ± 0.21
2 OS-SF Pairs	14.29 ± 1.91	1.28 ± 0.27	0.19 ± 0.20
$66 < M_{Z1} < 116$ GeV	10.03 ± 1.57	1.16 ± 0.26	0.00 ± 0.00
$M_{Z2} > 20$ GeV	7.43 ± 1.29	0.83 ± 0.17	0.00 ± 0.00
$66 < M_{Z2} < 116$ GeV	1.24 ± 0.36	0.25 ± 0.08	0.00 ± 0.00

Table 5.13: MC predicted number of events passing various levels of selection for the Z+jets, WZ/WW and top quark backgrounds in all four-lepton channels combined. The Z+jets background includes contributions from both light and heavy flavour jets. The top quark background includes contributions from $t\bar{t}$ and single top. The yields are normalised to 4.64 fb^{-1}.

5.7 Candidates Kinematic Distributions

The summary table of observed and expected events selected as described in the previous chapter together with background estimation calculated in section 5.6 is reported in section 5.7.1. The kinematic distributions for selected candidate events are shown in section 5.7.2.

5.7.1 Observed and Expected Events

The number of expected and observed events after applying all selection cuts are shown in Tab. 5.14. Both statistical and systematic uncertainties are given for both (ZZ and ZZ^*) selections in the table. In the $ZZ \to \ell^-\ell^+\ell^-\ell^+$ channel we observe 66 events passing the on-shell selection, with $53.4 \pm 0.3 \pm 2.2$ signal and $0.9 \pm 1.1 \pm 0.7$ background events expected (the first uncertainty is statistical and the second is systematic). Allowing one Z to be off-shell, we observe 84 events, with a signal expectation of $64.4 \pm 0.4 \pm 4.6$ and a background expectation of $9.1 \pm 2.3 \pm 1.3$.

$ZZ \to \ell^-\ell^+\ell^-\ell^+$	$e^+e^-e^+e^-$	$\mu^+\mu^-\mu^+\mu^-$	$e^+e^-\mu^+\mu^-$	$\ell^-\ell^+\ell^-\ell^+$
Observed ZZ	16	23	27	66
Observed ZZ^*	21	30	33	84
Expected ZZ	$10.3 \pm 0.1 \pm 1.0$	$16.5 \pm 0.2 \pm 0.9$	$26.7 \pm 0.2 \pm 1.7$	$53.4 \pm 0.3 \pm 3.2$
Expected ZZ^*	$12.3 \pm 0.2 \pm 1.2$	$20.5 \pm 0.2 \pm 1.1$	$31.6 \pm 0.3 \pm 2.0$	$64.4 \pm 0.4 \pm 4.0$
Expected Bkg ZZ	$0.5 \pm 0.6 \pm 0.3$	$0.3(\text{stat}) \pm 0.3(\text{syst})$	$0.7 \pm 0.7 \pm 0.6$	$0.9 \pm 1.1 \pm 0.7$
Expected Bkg ZZ^*	$4.3 \pm 1.4 \pm 0.6$	$< 0.7(\text{stat}) \pm 0.5(\text{syst})$	$5.8 \pm 1.6 \pm 0.9$	$9.1 \pm 2.3 \pm 1.3$

Table 5.14: Summary of observed events and expected signal and background contributions in the individual sub-channels and combined. The background estimations cover $Z + X$, top, other diboson processes, and $W + X$. The first error is statistical while the second is systematic. The systematics quoted on the signal and background yield do not include the uncertainty on the luminosity.

5.7.2 Kinematic Distributions

Figure 5.5 shows the mass of the leading Z candidate versus the mass of the subleading Z candidate for the data and predicted signal events in the $ZZ \to \ell^-\ell^+\ell^-\ell^+$ channel. The estimated background distribution to this plot is shown in Fig. 5.6.

Distributions of the mass of the leading and subleading Z ($M^{\text{leading Z}}$, $M^{\text{subleading Z}}$) in the ZZ^* selection case are shown in Fig. 5.7. Obviously this case includes also the distributions of $M^{\text{leading Z}}$ and $M^{\text{subleading Z}}$ for both on-shell $Z's$ in the mass window (66-116 GeV). M^{ZZ}, $p_{\text{T}}^{\text{leading Z}}$, $p_{\text{T}}^{\text{subleading Z}}$ and p_{T}^{ZZ} for the final $ZZ \rightarrow \ell^-\ell^+\ell^-\ell^+$ candidates are shown in Figure 5.8 for the selection allowing one Z to be off-shell ($m^{Z2} > 20$ GeV), for all four-lepton final states combined. Fig. 5.9 shows the same distributions for events passing the ZZ selection (66 GeV $< m^{Z2} <$ 116 GeV). In all plots, the points are data and the stacked histograms shows the signal and background prediction from simulation and data-driven methods, normalized to the luminosity of the data. The gray band indicates the combined statistical and systematic uncertainty on the signal prediction.

Similar distributions split by four-lepton final state are given in Appendix B.
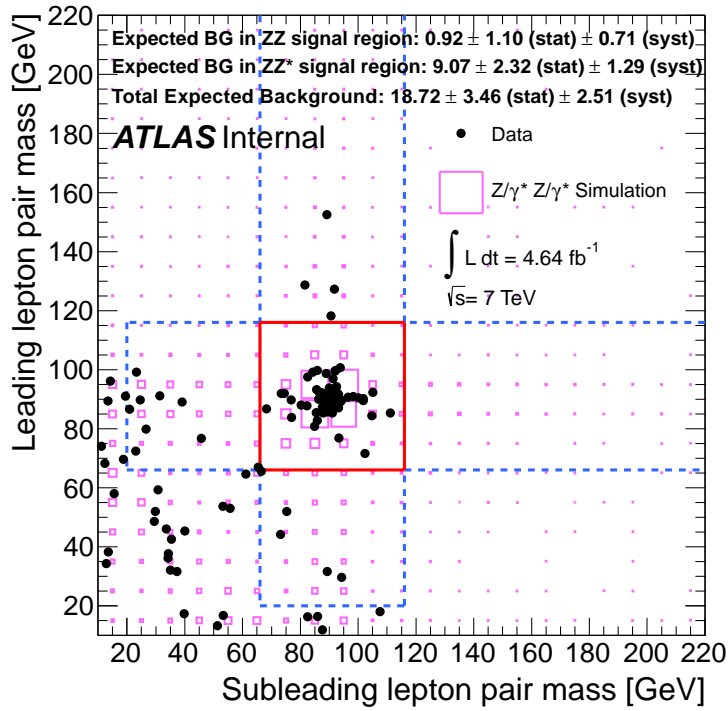
Figure 5.5: The mass of the leading Z candidate versus the mass of the subleading Z candidate. The events observed in the data are shown as solid points and the signal prediction from simulation normalized to the luminosity of the data as pink boxes, where the size of each box is proportional to the yield in that bin. The solid red box indicates the ZZ signal region defined by the cuts on the Z masses. The area enclosed by the dashed blue lines indicates the ZZ^* signal region, defined by the cuts on the Z and Z^* masses.
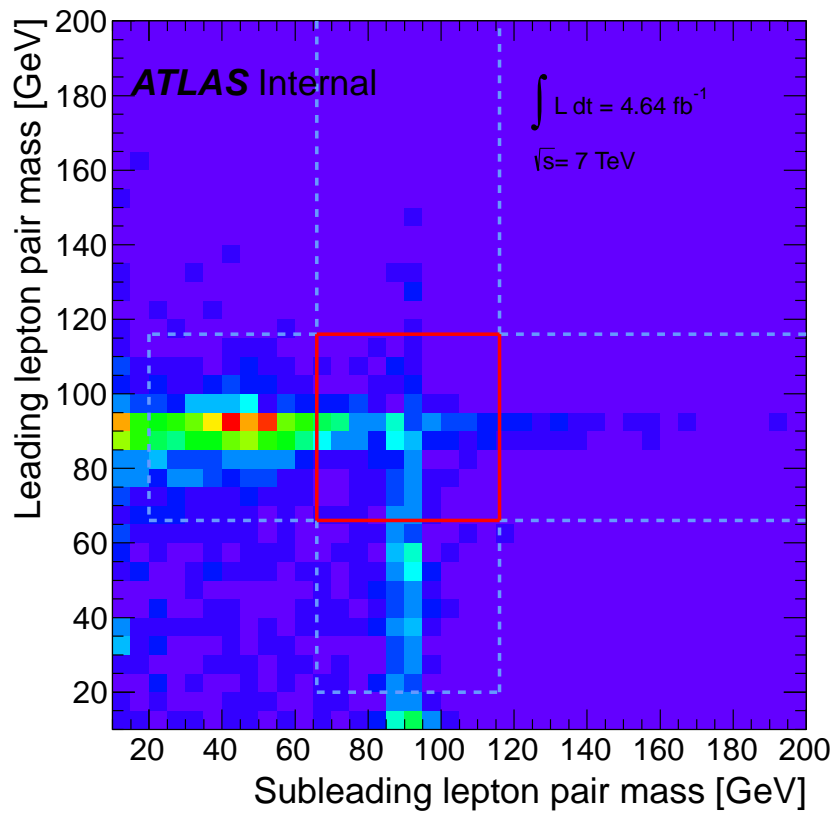
Figure 5.6: The simulated distribution of the mass of the leading Z candidate versus the mass of the subleading Z candidate in background events. The distribution is taken from Monte-Carlo and normalised to the estimated background. The area enclosed by the dashed blue lines indicates the ZZ^* signal region, defined by the cuts on the Z and Z^* masses.
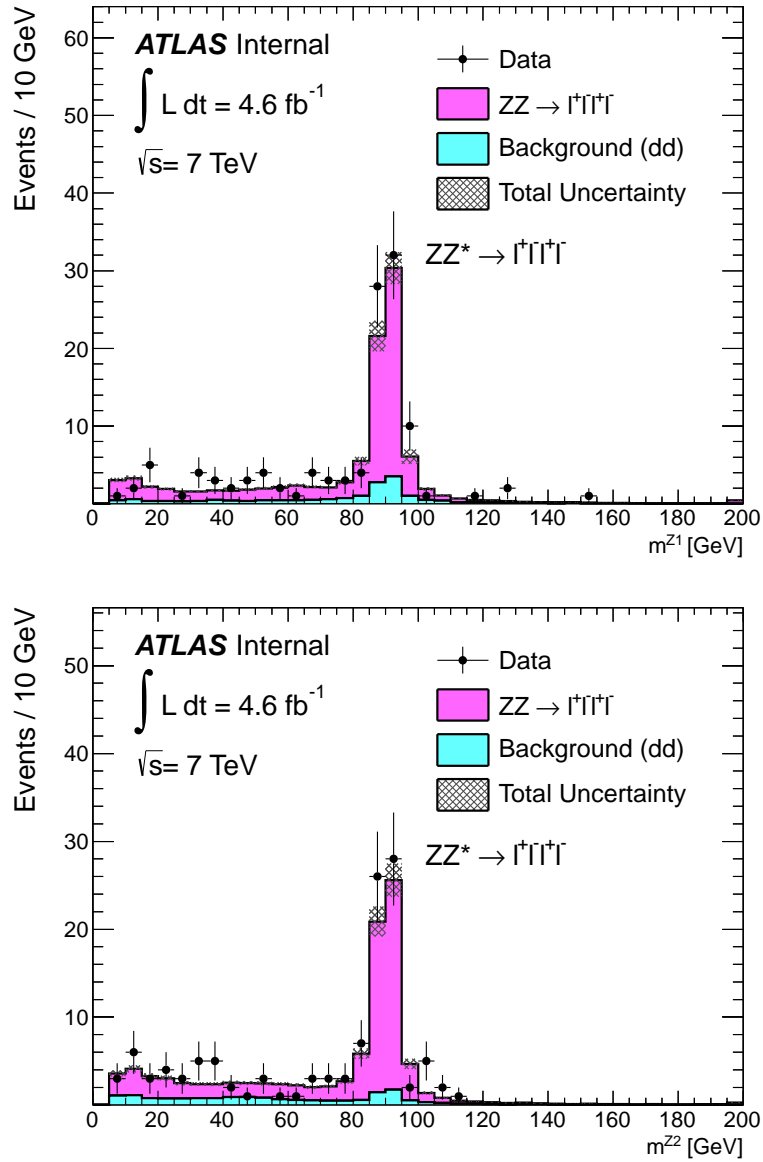
Figure 5.7: $M^{leading\ Z}$ (top) and $M^{subleading\ Z}$ (bottom) distributions for $ZZ \to \ell^-\ell^+\ell^-\ell^+$ candidates in all four-lepton channels allowing one Z to be off shell (ZZ^*selection).
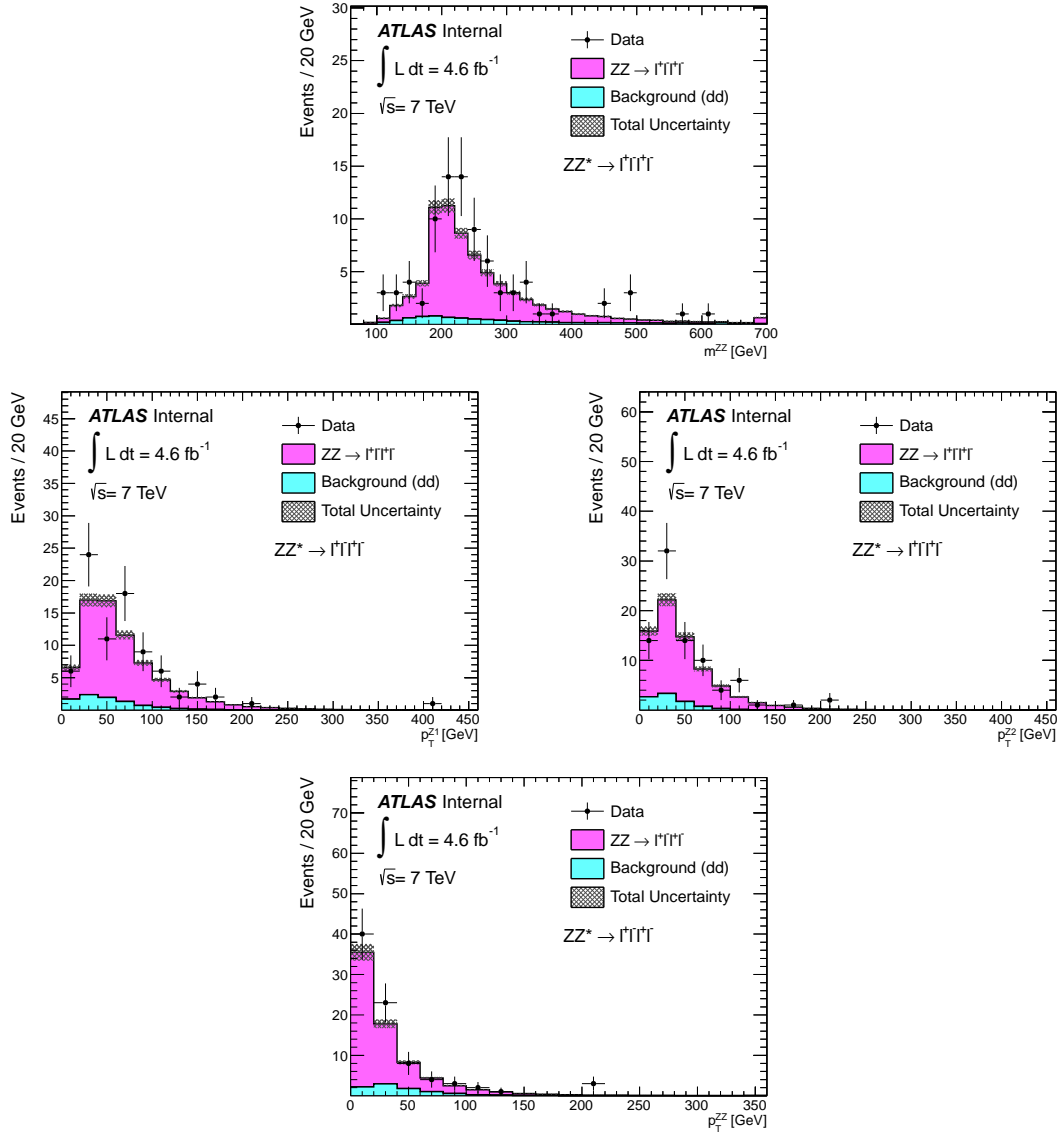
Figure 5.8: Kinematic distributions for $ZZ \to \ell^-\ell^+\ell^-\ell^+$ candidates in all four-lepton channels allowing one Z to be off shell (ZZ^*selection). On top the M^{ZZ}, in the central row the $p_{\mathrm{T}}^{leading\ Z}$ (middle left) and the $p_{\mathrm{T}}^{subleading\ Z}$ (midle right) and finally the p_{T}^{ZZ} are shown.
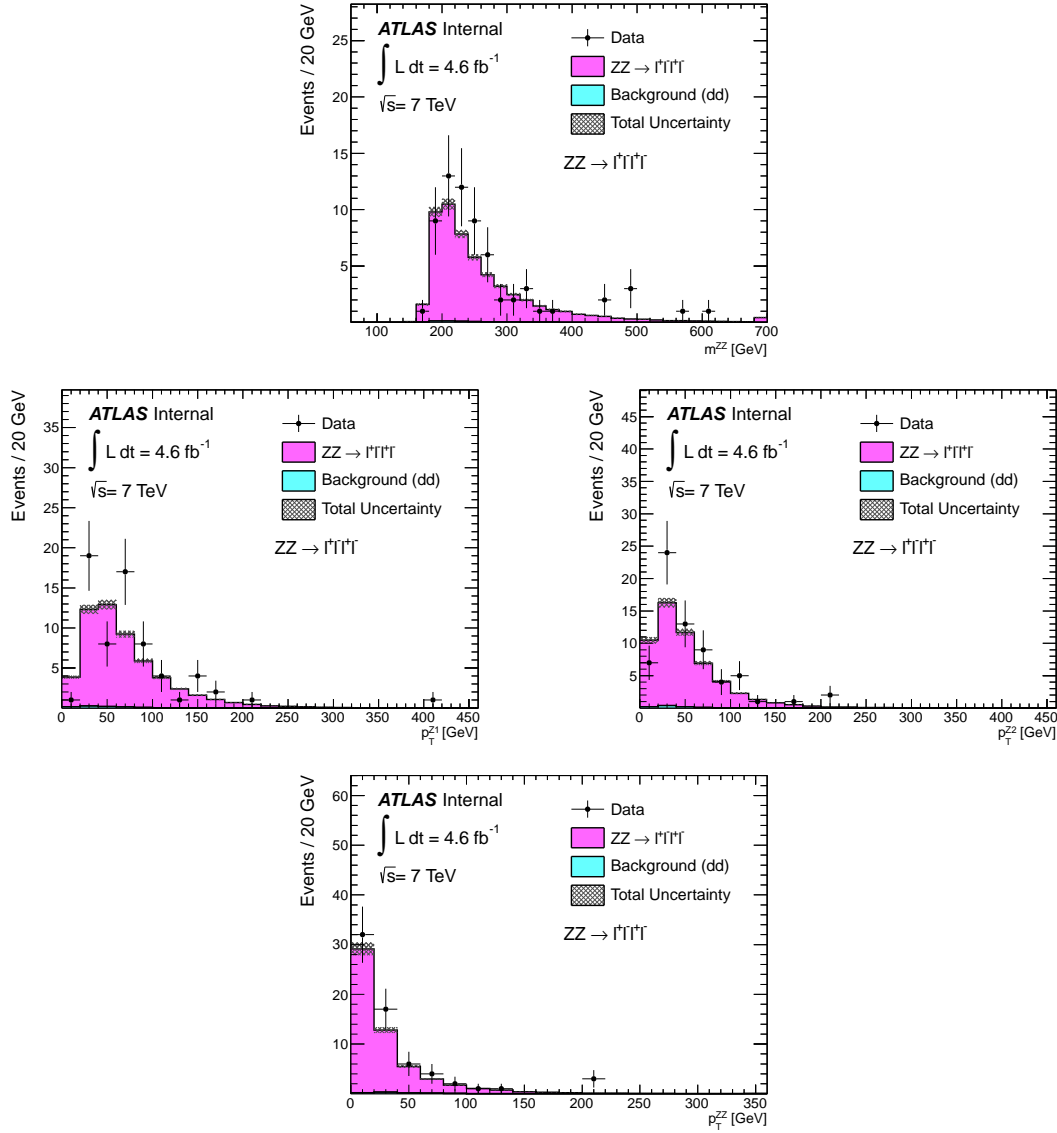
Figure 5.9: Kinematic distributions for $ZZ \to \ell^- \ell^+ \ell^- \ell^+$ candidates in all four-lepton channels applying the on-shell (ZZ) selection. The top plot shows the M^{ZZ}, in the middle row the $p_\mathrm{T}^{leading\ Z}$ (left) and $p_\mathrm{T}^{subleading\ Z}$ (right) and finally on the bottom the p_T^{ZZ} are shown.

5.8 Cross Section Results

The combined (*eeee*, *eeμμ* and *μμμμ*) cross section has been calculated using a minimum log-likelihood approch, taking into account Poisson statistics and systematic uncertainties. The decay channels are merged before maximizing the profile likelihood function with respect to the cross section σ.

5.8.1 Fiducial and Total Cross Section

The profile likelihood function for the fiducial cross section is the product of a Poisson probability distribution (P) and Gaussian distribution function for each of the nuisance parameters (C_{ZZ}, A_{ZZ}, N^{bkg}, $\mathcal{L}$) affected by a systematic uncertainty.

The Poisson function for the number of observed events N^{obs} is

$$P(\sigma, C_{ZZ}, N^{bkg}; N^{obs}) = \frac{e^{-(s(\sigma,C_{ZZ})+N^{bkg})} \cdot \left(s(\sigma, C_{ZZ}) + N^{bkg}\right)^{N^{obs}}}{N^{obs}!}, \qquad (5.18)$$

where the number of signal events is a function of the cross section, the background N^{bkg} and other quantities such as the integrated luminosity and correction factors.

For the fiducial cross sections, the number of signal events is

$$s(\sigma^{\text{fid}}_{ZZ \to \ell^-\ell^+\ell^-\ell^+}, C_{ZZ}) = \sigma^{\text{fid}}_{ZZ \to \ell^-\ell^+\ell^-\ell^+} \times C_{ZZ} \times \mathcal{L} \qquad (5.19)$$

while for the total cross section:

$$s(\sigma^{\text{tot}}_{ZZ}, C_{ZZ}) = \sigma^{\text{tot}}_{ZZ} \times C_{ZZ} \times A_{ZZ} \times \text{BR}_{\text{comb}}(ZZ \to \ell^-\ell^+\ell^-\ell^+) \times \mathcal{L} \qquad (5.20)$$

The A_{ZZ} in the latter formula accounts for the total volume of the measurement and $\text{BR}_{\text{comb}}(ZZ \to \ell^-\ell^+\ell^-\ell^+)$ is the specific channel combined branching ratio discussed in section 5.2.

The measured fiducial cross sections with associated statistical and systematic uncertainties for ZZ and ZZ^* selection are reported in Equations 5.21 and 5.22 respectively.

$$\sigma^{\text{fid}}_{ZZ \to \ell^-\ell^+\ell^-\ell^+} = 25.4^{+3.3}_{-3.0}(\text{stat.})^{+1.2}_{-1.0}(\text{syst.}) \pm 1.0(\text{lumi.})(\text{fb}) \qquad (5.21)$$

$$\sigma^{\text{fid}}_{ZZ^* \to \ell^-\ell^+\ell^-\ell^+} = 29.8^{+3.8}_{-3.5}(\text{stat.})^{+1.7}_{-1.5}(\text{syst.}) \pm 1.2(\text{lumi.})(\text{fb}) \qquad (5.22)$$

The total cross section for ZZ production results

$$\sigma^{\text{tot}}_{ZZ} = 7.0^{+0.9}_{-0.8}(\text{stat.})^{+0.4}_{-0.3}(\text{syst.}) \pm 0.3(\text{lumi.})(\text{pb})$$

5.9   Summary

A measurement of the $ZZ \to \ell^-\ell^+\ell^-\ell^+$ production cross-section with the AT-LAS detector in LHC proton- proton collisions at $\sqrt{s} = 7$ TeV has been performed using electrons and muons in the final state. In a dataset with an integrated luminosity of 4.64 fb^{-1} a total of 66 ZZ and 84 ZZ^* candidates were observed with a background expectation of $0.9 \pm 1.1(stat) \pm 0.7(syst)$ and $9.1 \pm 2.3 \pm 1.3$. The Standard Model expectation for the number of signal events is $53.4 \pm 0.3 \pm 2.2$ for the ZZ and $64.4 \pm 0.4 \pm 4.6$ for the ZZ^* case.

The fiducial cross-sections were determined to be

$$\sigma^{\text{fid}}_{ZZ \to \ell^-\ell^+\ell^-\ell^+} = 25.4^{+3.3}_{-3.0}(\text{stat.})^{+1.2}_{-1.0}(\text{syst.}) \pm 1.0(\text{lumi.})(\text{fb})$$

$$\sigma^{\text{fid}}_{ZZ^* \to \ell^-\ell^+\ell^-\ell^+} = 29.8^{+3.8}_{-3.5}(\text{stat.})^{+1.7}_{-1.5}(\text{syst.}) \pm 1.2(\text{lumi.})(\text{fb})$$

In the ZZ selection with both Z on-shell the total cross section was determined to be

$$\sigma^{\text{tot}}_{\text{ZZ}} = 7.0^{+0.9}_{-0.8}(\text{stat.})^{+0.4}_{-0.3}(\text{syst.}) \pm 0.3(\text{lumi.})(\text{pb})$$

The result is consistent with the NLO Standard Model prediction of $5.89^{+0.22}_{-0.18}$ pb, calculated with Z bosons with a mass between 66 and 116 GeV.

Recently ATLAS published [67] the ZZ cross section combining the above $ZZ \to \ell^-\ell^+\ell^-\ell^+$ channel with the $ZZ \to \ell^-\ell^+\nu\bar{\nu}$ channel. The obtained total cross section value is $6.7^{+0.7}_{-0.7}(\text{stat.})^{+0.4}_{-0.3}(\text{syst.}) \pm 0.3(\text{lumi.})(\text{pb})$. The comparison with theoretical predictions and other measurements are shown in Fig. 5.10.
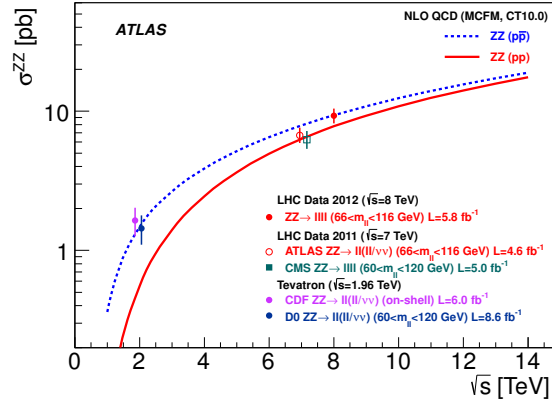
Figure 5.10: LHC and Tevatron measurements compared with theoretical predictions of the total ZZ production cross section in pp and $p\bar{p}$ collisions as a function of centre of mass energy $\sqrt{s}$.

Chapter 6

Unfolding of Differential Distributions

6.1 Introduction

In this chapter the "Unfolding" procedure applied on three differential distributions $(\Delta\phi(l, l), p_T^Z$ and $M_{4l})$ of the ZZ selection is presented. This procedure, also referred as "Inverse Problems" or "Unsmearing" concerns the correction of distorted distributions. Distortion of distributions occurs when the values of a variable are subject to additional random flactuations due to the limited resolution of the measuring device. In section 6.2 the general unfolding problem is formulated, the adopted methodology for the ZZ case follows in section 6.3 and finally the unfolding results are presented in section 6.4.

6.2 Formulation of the Unfolding Problem

In high energy physics experiments the main goal is to determine the true underlying value of any measured observable. In any experiment, the distribution of a measured observable differs from that of the corresponding "true" physical quantities due to detector effects, such as limited acceptance, reduced efficiency, and finite resolution. From a mathematical point of view [68, 69], given some observable kinematical quantity x distributed according to $f(x)$, its probability density function (p.d.f.), one typically measures a different variable y distributed according to a different p.d.f $g(y)$. The relation between $f(x)$, to be determined in an experiment and the measured distribution $g(y)$ is given by the integral equation:

$$g(y) = \int A(y, x) f(x) \mathrm{d}x, \qquad (6.1)$$

where the resolution function $A(y, x)$ describes the detector effects on the measurement. The problem to determine $f(x)$ (true distribution) from the measured distribution $g(y)$ is called "*Unfolding*". Frequently one does not know the full analytic parameterizations of $g(y)$ and $A(y, x)$, but instead one has discretized samplings of the distributions in the form of histograms. Treating each bin of a histogram as a vector or matrix element, the convolution Eq 6.1 can be represented in matrix form,

$$\mathbf{A}\mathbf{x} = \mathbf{y} \tag{6.2}$$

which can be solved for $\mathbf{x}$, given the vector $\mathbf{y}$. The vector $\mathbf{y}$ with n elements represents the data histogram of measured quantities y, and the distribution $f(x)$ is represented by a histogram of the vector $\mathbf{x}$ with m elements. The transformation matrix from $\mathbf{x}$ to $\mathbf{y}$ is represented by the $n \times m$ response matrix $\mathbf{A}$. The elements of the response matrix a_{ij} can be thought of as the probability for a true value x_j to be measured as a value y_i.

While analytic parameterization of $\mathbf{A}$ is not typically available, one can generally model these detector effects using Monte Carlo (MC) simulations of the underlying physics and a model of the detecting device, whereby the interactions of predicted particles with the matter content of the detector are simulated. Given the response matrix, the underlying true distribution from a measured spectrum can be determined inverting the smearing effects of the measured data to produce directly a measured true distribution, i.e. look for a solution of the form $\mathbf{x} = \mathbf{A}^{-1}\mathbf{y}$. By unfolding the distributions one provides a result ahich can directly be compared with those of other experiments as well as with theoretical predictions which may be developed in the future.

There are many unfolding procedures [68, 69, 70, 71, 72] one can use to determine the true underlying distribution of the measured data. In the following only the simple "Bin-by-Bin" and the "Bayesian" methods are briefly described. For a complete discussion one can refer to the above literature.

6.2.1   Bin-by-Bin Unfolding

Bin-by-Bin is the simplest unfolding technique. For each bin in the observed vector, $\mathbf{y}$, a correction factor, c_i is calculated from a control sample (typically from Monte Carlo simulation) that describes the ratio of observed to true events. For example, given a simulated sample of observed $\mathbf{y^{sim}}$ and true $\mathbf{x^{sim}}$ measurements, the correction factors are calculated as simply:

$$c_i = y_i^{sim}/x_i^{sim}$$

For an observed data sample $\mathbf{y^{data}}$, the final, unfolded result is taken simply to be:

$$x_i^{data} = y_i^{data}/c_i$$

This technique is conceptually very simple, avoids complicated error calculations and bin-to-bin correlations, and requires little computation. However, since there are no explicit bin-to-bin migration corrections, this method can be safely used if the bin-purity exceeds 80%, such that the majority of reconstructed events remain within the bin in which they were generated. In fact, if the bin purities are low, the unfolded result is highly biased by the control sample used to produce the bin-by-bin corrections. In other words, with the Bin-by-Bin method, completely different results depending on the MC sample used can be found.

While the bin-by-bin unfolding technique is used in this analyses as a cross-check unfolding method, the nominal values are coming from the Bayesian unfolding technique, briefly described in the following.

6.2.2 Bayesian Unfolding

Bayesian unfolding [72] is an iterative unfolding algorithm that uses Bayes theorem to perform unfolding, treating the response matrix as a description of the probability of observed data given the true distribution.

Mathematically, the Bayesian unfolding algorithm attempts to determine the probability distribution of true events given the observed data and the response matrix, stated as:

$$P(\mathbf{x} \mid \mathbf{y}, \mathbf{A}, I) \tag{6.3}$$

where, as before, $\mathbf{x}$ is the true distribution, $\mathbf{y}$ is the observed data, $\mathbf{A}$ is the response matrix, and the new variable, I, is the underlying assumptions of the analysis, which are usually left implicit.

By use of Bayes theorem, we may rewrite Eq. 6.3 as

$$P(\mathbf{x} \mid \mathbf{y}, \mathbf{A}, I) \propto P(\mathbf{y} \mid \mathbf{x}, \mathbf{A}, I) \cdot P(\mathbf{x} \mid I) \tag{6.4}$$

where the first term on the right is the likelihood of the observed data, and the second term is the prior on the underlying truth distribution.

A difficulty arises from this equation in that the unfolded value will be strongly influenced by the the underlying prior distribution. In particular, if a Monte Carlo model is used to produce a prior, as is typically the case, the unfolded value will be biased towards the truth distribution of the Monte Carlo used. Further, this method naïvely can suffer from problems related to regularized matrix inversion:

namely, oscillations due to amplified statistical errors. To solve both of these problems, Bayesian unfolding uses an iterative smoothing approach, which allows the number of iterations to be used a regularization parameter.

The first iteration consists of solving Eq. 6.4 above using the supplied Monte Carlo truth distribution as the prior distribution. For subsequent iterations, the result from the previous iteration is used as the prior. The more iterations that are run, the less the bias from the Monte Carlo truth distribution becomes. However, at the same time, as the bias decreases, the statistical uncertainty increases, as statistical fluctuations are amplified due to the positive feedback nature of the system. Thus, the number of iterations serves to balance the strength of the bias with the size of the oscillations. In general, the number of iterations taken is small (see section 6.4.3), as otherwise the statistical errors become very large.

The main advantages in using this technique are listed in the following:

- It is implemented in the RooUnfold package, which simplifies integration with ROOT based analysis.

- It contains only one parameter, the number of iterations, which is easily understood and readily optimized, because good solutions occupy a relatively small phase in this parameter.

- It can take into account of any kind of smearing and migration from the true values to the observed ones.

- It provides the correlation matrix of the results.

- The algorithm is very fast, which makes uncertainty calculations via toy Monte Carlo and pseudo-experiments computationally feasible.

- The prior distribution does not negatively impact the ability of the algorithm to correctly unfold rapidly falling distributions.

For these reasons, Bayesian unfolding has been chosen as the nominal procedure for the final result of this analysis.

6.3   Specific Adopted Methodology

The "unfolding" methodology used in this analysis is described here. In order to transform the measured distribution $\mathbf{d}$, with $\mathbf{y}$ as the signal and $\mathbf{b}$ as the expected background contribution, to the unfolded distribution $\mathbf{x}$, the following three quantities via fully simulated Monte Carlo signal samples are defined:

- the response matrix **A**. The response matrix accounts for bin-to-bin migrations between the reconstructed and the truth distribution. It should be noted that it is only defined for events which are selected on reconstruction level and also fall in the fiducial volume defined on truth level.

- the correction factors $c_i = \frac{N_i^{reco}}{N_i^{truth}}|_{\text{in fid.}}$ for each bin i of the unfolded distribution, as the ratio of reconstructed events N_i^{reco} in bin i over the number of MC truth events N_i^{truth}. where all events are required to fall in the fiducial region defined in truth level. It should be noted that the bin i is defined here by the truth value of the unfolding variable. This correction factor accounts for acceptance and efficiency losses on the reconstruction level.

- the fiducial factors $f_i = \frac{N_i^{\text{in fid.}}}{N_i}|_{\text{is reco.}}$ for each bin i of the reconstructed distribution, as the ratio of events which fall in the fiducial region on truth level $N_i^{\text{in fid.}}$ over all events N_i, where all events are required to be reconstructed and selected in the same bin. It should be noted that the bin i is defined here by the reconstructed value of the unfolding variable. This correction factor is used to correct for those reconstructed events, which do not fall in the fiducial region and hence have no associated truth-value which can be used during the unfolding.
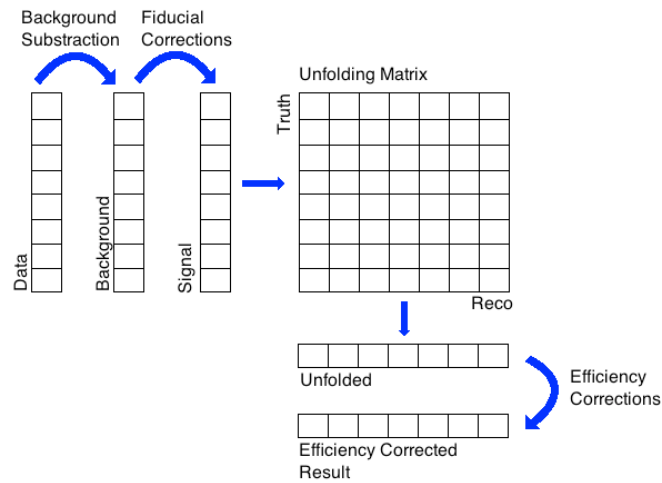
Figure 6.1: Principle method for unfolding in a distribution in a fiducial volume.

With these definitions, we have the equations:

$$y_i = (d_i - b_i) \cdot f_i$$

$$x_i = (A_{i,j}^{-1} y_i) \cdot c_i$$

which is schematically illustrated in Fig. 6.1. The central value of the unfolded distribution is based on the nominal MC simulation of the signal samples, including all detector corrections such as efficiencies, scales and resolutions. An array of event-information for a given signal Monte Carlo sample, is defined and called SIGNAL NTUPLE in the following. It contains value and event weights (MC truth weight, reconstruction or trigger efficiency...) of the quantity to be unfolded at both "truth" and "reconstruction" level.

The statistical uncertainty of the unfolded distribution is tested via Toy-Monte Carlo tests. Each measured data-entry d_i is Poisson fluctuated and the full nominal unfolding procedure is applied. This is repeated 200 times and the RMS of the resulting unfolded values x_i is taken as statistical uncertainty.

The systematic uncertainties are evaluated as follows: For each systematic uncertainty, i.e. each scale, efficiency or resolution variation, a new SIGNAL NTUPLE is produced for which the corresponding systematic variation has been applied. In a second step, the quantities $\mathbf{A}$, c_i and f_i are defined with the SIGNAL NTUPLE, each corresponding to one systematic variation. The measured data-distribution is then unfolded for all instances separately, leading to one distribution $\mathbf{x^{sys}}$ for each systematic uncertainties. The difference $\delta_i^{sys} = x_i - x_i^{sys}$ is defined as systematic uncertainty in each bin. The corresponding covariance matrix for bins i and j is defined via

$$Cov_{i,j} = \delta_i^{sys} \times \delta_j^{sys}.$$

The several covariance matrixes of all systematic uncertainties can be linearly added, which enables the definition of the global bin-by-bin correlation matrix $C_{i,j}$ via

$$C_{i,j} = \frac{Cov_{i,j}}{\sqrt{Cov_{i,i}}\sqrt{Cov_{j,j}}}.$$

Most systematic uncertainties are split up in an upwards and downwards variation of 1σ around their nominal values, e.g. once the Monte Carlo signal sample is processed with a jet energy scale $+1\sigma$ and once with a jet energy scale -1σ. These two variations clearly are fully correlated. In order to give a conservative estimate during the first round of this measurement, we take the larger value of δ_i^{sys} for both variations as symmetric error. The corresponding correlations are estimated via the Monte Carlo sample including the $+1\sigma$ variation.

6.4 $ZZ \to \ell^-\ell^+\ell^-\ell^+$ Unfolded Distributions

The differential cross sections present a more detailed comparison of theory to measurement, allowing a generic comparison of the kinematic distributions to new theories. Variables which are sensitive to new phenomena, such as p_T^Z, $\Delta\phi(l,l)$ M_{4l}, have been chosen to be unfolded with bin boundaries in order to maximize sensitivity to nTGCs. At the same time, the bin widths were chosen to be commensurate with the detector resolution.

Bin	Estimated Background	Expected Signal	Observed events
$0 < p_\mathrm{T}(Z) < 60$ GeV	$0.63 \pm 0.75 \pm 0.48$	$27.9 \pm 0.2 \pm 1.0 \pm 1.8$	28
$60 < p_\mathrm{T}(Z) < 100$ GeV	$0.20 \pm 0.24 \pm 0.15$	$14.6 \pm 0.2 \pm 0.6 \pm 1.0$	25
$100 < p_\mathrm{T}(Z) < 200$ GeV	$0.09 \pm 0.10 \pm 0.07$	$9.3 \pm 0.1 \pm 0.4 \pm 0.8$	11
$200 < p_\mathrm{T}(Z)$ GeV	$0.01 \pm 0.01 \pm 0.01$	$1.6 \pm 0.1 \pm 0.1 \pm 0.2$	2
$0 < \Delta\phi(\ell^+,\ell^-) < 0.5$ rad	$0.05 \pm 0.06 \pm 0.04$	$2.5 \pm 0.1 \pm 0.1 \pm 0.4$	4
$0.5 < \Delta\phi(\ell^+,\ell^-) < 1.0$ rad	$0.07 \pm 0.08 \pm 0.05$	$3.7 \pm 0.1 \pm 0.2 \pm 0.3$	8
$1.0 < \Delta\phi(\ell^+,\ell^-) < 1.7$ rad	$0.10 \pm 0.12 \pm 0.08$	$8.9 \pm 0.2 \pm 0.4 \pm 0.8$	11
$1.7 < \Delta\phi(\ell^+,\ell^-) < \pi$ rad	$0.70 \pm 0.84 \pm 0.54$	$38.3 \pm 0.4 \pm 1.4 \pm 2.6$	43
$0 < M_{4\ell} < 240$ GeV	$0.39 \pm 0.47 \pm 0.30$	$28.8 \pm 0.3 \pm 1.0 \pm 1.4$	35
$240 < M_{4\ell} < 300$ GeV	$0.18 \pm 0.21 \pm 0.14$	$12.8 \pm 0.2 \pm 0.5 \pm 0.9$	17
$300 < M_{4\ell} < 400$ GeV	$0.15 \pm 0.18 \pm 0.11$	$7.7 \pm 0.1 \pm 0.3 \pm 0.5$	7
$400 < M_{4\ell}$ GeV	$0.21 \pm 0.21 \pm 0.12$	$4.0 \pm 0.1 \pm 0.2 \pm 0.7$	7

Table 6.1: Data-driven backgrounds of $\ell^-\ell^+\ell^-\ell^+$, and expected signal in the ZZ selection, together with the observed data as a function of i) the p_T of the leading Z (top section), ii) the $\Delta\phi$ between the two leptons of the leading Z (middle section), and iii) of the mass of the $\ell^-\ell^+\ell^-\ell^+$ system (bottom section).

In the $ZZ \to \ell^-\ell^+\ell^-\ell^+$ selection the binning used is $[0, 60, 100, 200$ GeV] in the case of the p_T^Z while $[0, 0.5, 1.0, 1.7, \pi]$ is used for the $\Delta\phi(l,l)$ unfolding, where the Z is the one with the highest p_T (leading Z) and the two leptons are the ones forming the leading Z. The third variable chosen is the mass of the four leptons system, M_{4l}[1], in the following binning: $[0, 240, 300, 400$ GeV]. The expected signal yield, the observed events and the data-driven backgrounds, calculated as discussed

---

[1]the mass of the four leptons system is indicated, in a completely equivalent way, also as m^{ZZ}.

in the previous chapter, for the three binned distributions (p_T^Z, M_{4l} and $\Delta\phi(l,l)$) are shown in Tab. 6.1

6.4.1 Unfolding Results

The unfolded distributions are normalized within the given kinematic range to unity, i.e. we measure $(1/\sigma_{fid})d\sigma_{fid}/dX$ (where X is the unfolded variable). The normalization implies that detector corrections which are independent from the unfolding variable X have no impact on the final result. Hence, only shape-dependent systematic effects will impact the final result. In addition, the normalization requirement leads to an additional constraint which also impacts the bin-by-bin correlation for the statistical uncertainties. This can be most easily understood when considering only two bins. In order to keep the overall normalization constant, the upwards fluctuation of one bin, implies a downward fluctuation in the other bin. The unfolded distributions are shown in Fig. 6.2 using "natural" bin widths and the response matrices used in the unfolding in Fig. 6.3. The distributions are normalised to the fiducial cross-sections derived in the previous chapter. The measured values are compared with the predictions from the MC generators used to model the signal processes. The same distributions using a different bin choice are shown in Appendix C.

6.4.2 Unfolding MC closure tests

A closure test is perfomed to verify the correctness of the procedure applied. The signal MC (PowhegBox) is used to generate the response matrix and then the reconstruction level distribution from the same MC is unfolded. Figure 6.4 shows the results where the unfolded and truth distributions are found to match exactly.

The dependence of the unfolding from the MC used to calculate the response matrix is tested unfolding the same MC sample but using different MC samples to build the response matrix: the PowhegBox distribution is unfolded using a response matrix based on Sherpa and compared to the expected truth distribution. The results are presented in Fig. 6.5. The bias due to using Sherpa for the response matrix are at a maximum level of 4% depending on the bin and/or the variable considered. This is accounted for in the systematic uncertainty (see entries labelled as "MC generator" in tables of section 6.4.4).

6.4.3 Unfolding Procedure Stability

The stability of the unfolding procedure is tested by comparing the results of the Bayesian unfolding algorithm up to 10 iterations. The differences in terms
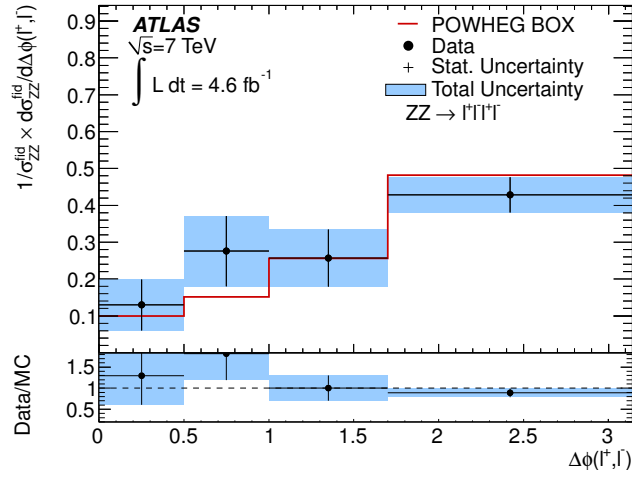
(a) Unfolded $\Delta\phi(\ell,\ell)$ distribution.
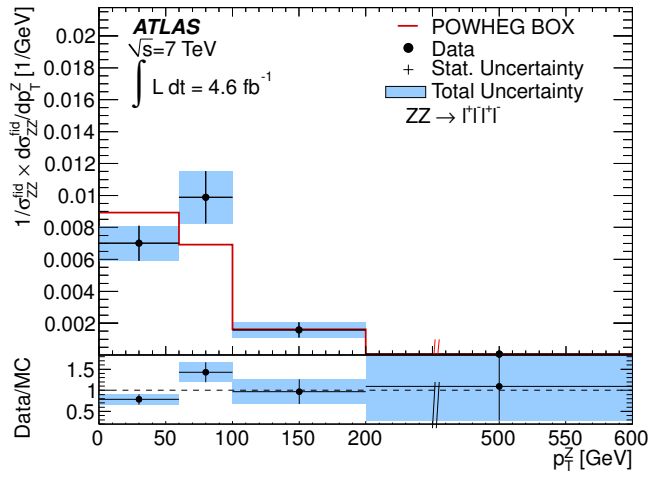
(b) Unfolded p_T^Z distribution.
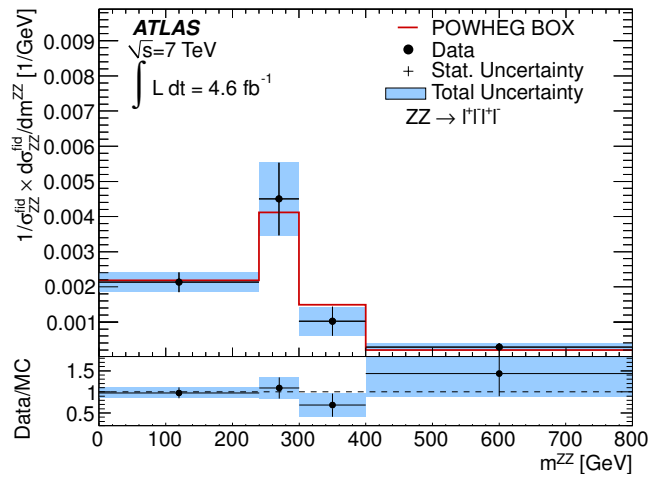
(c) Unfolded m^{ZZ} distribution.

Figure 6.2: Unfolded distributions for $ZZ \rightarrow \ell^-\ell^+\ell^-\ell^+$ selection.
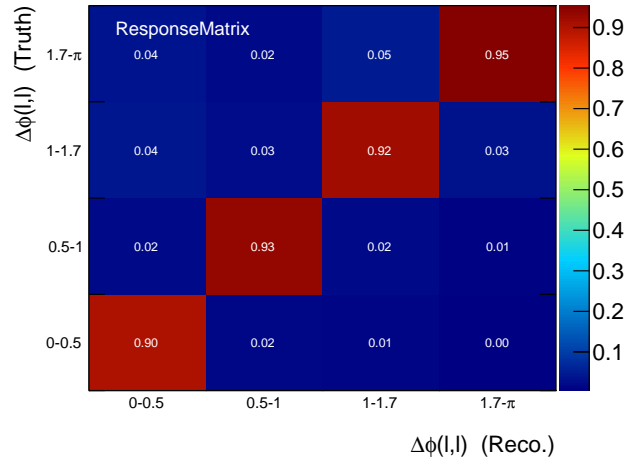
(a) Response matrix for $\Delta\phi(l, l)$ distribution.
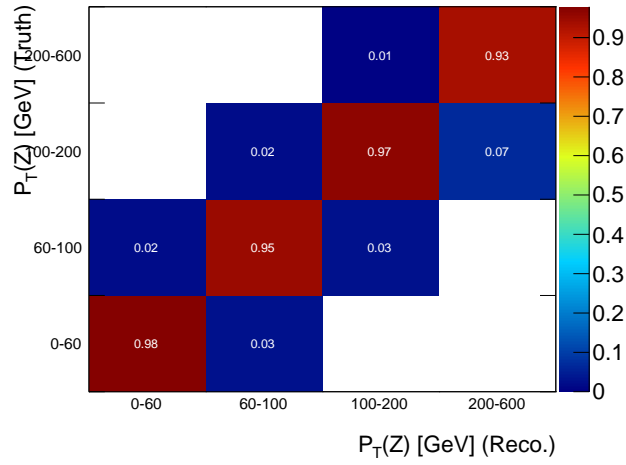
(b) Response matrix for p_T^Z distribution.
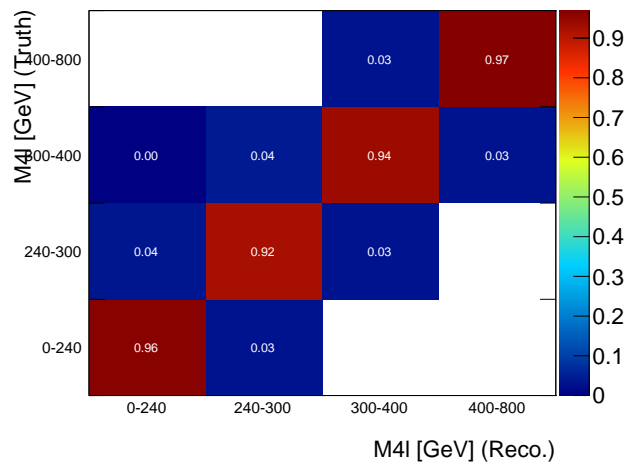
(c) Response matrix for $M_{4\ell}$ distribution.

Figure 6.3: Response matrices for $ZZ \to \ell^-\ell^+\ell^-\ell^+$ selection.
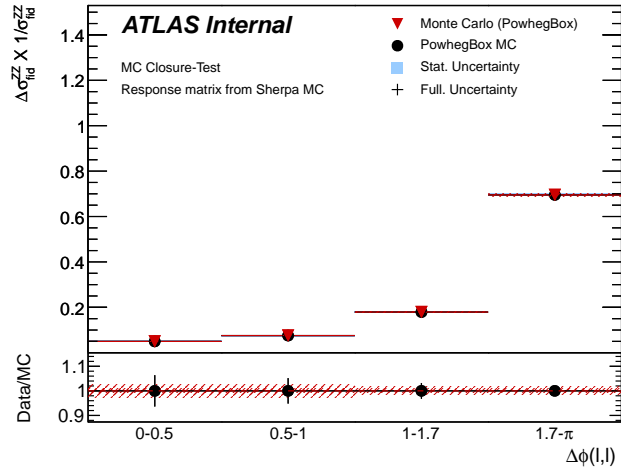
(a) Closure test for $\Delta\phi(l,l)$ distribution.
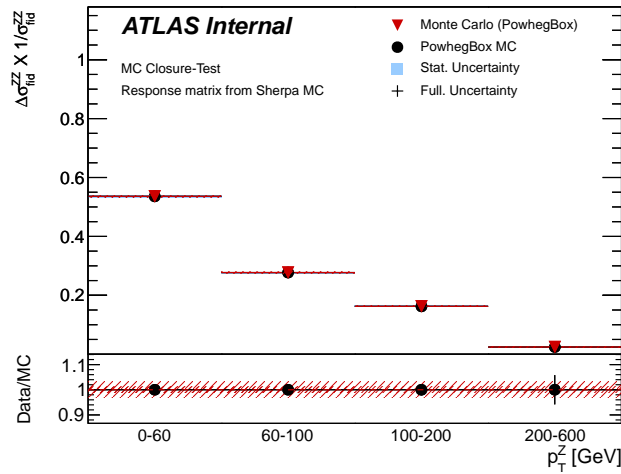
(b) Closure test for p_T^Z distribution.
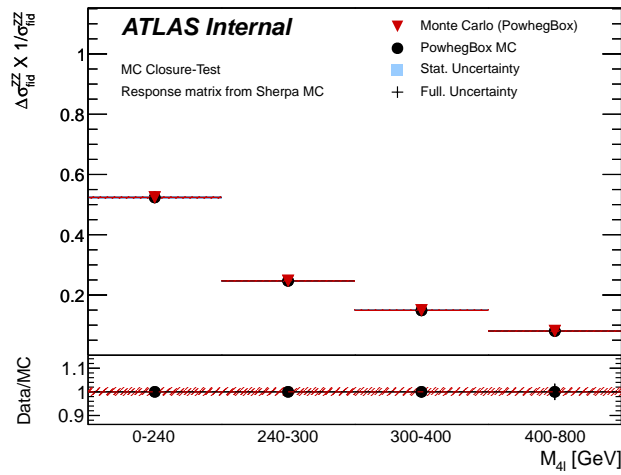
(c) Closure test for $M_{4\ell}$ distribution.

Figure 6.4: Closure test results. MC signal events are used here as "data".
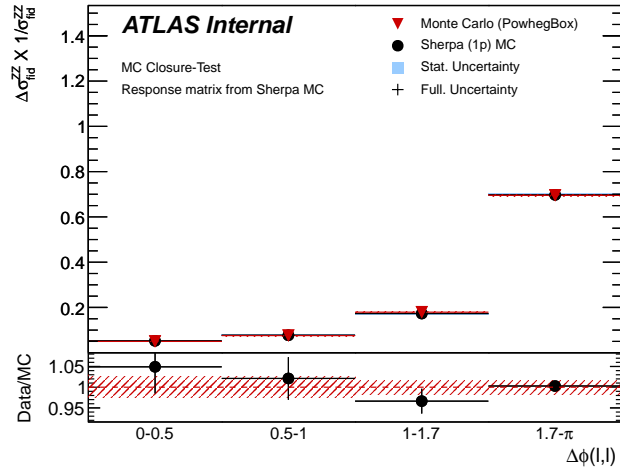
(a) Closure test for $\Delta\phi(l,l)$ distribution.
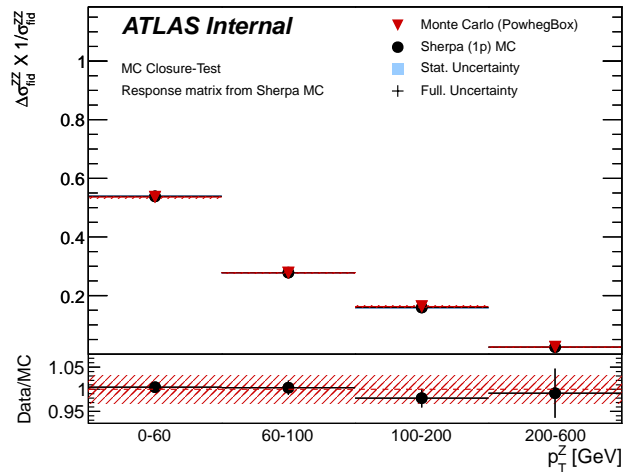
(b) Closure test for p_T^Z distribution.
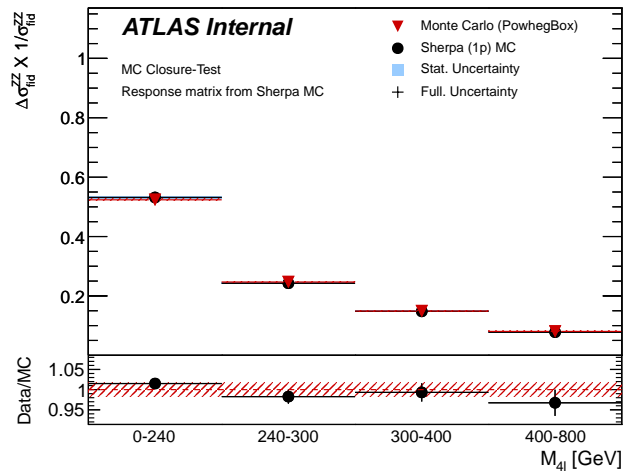
(c) Closure test for $M_{4\ell}$ distribution.

Figure 6.5: Closure test results for $ZZ \to \ell^-\ell^+\ell^-\ell^+$ unfolding MC signal events, used here as "data", with a response matrix from a different MC.

of percentage change in each bin with respect to one iteration and the next one are shown in top part of Fig. 6.6. The variation of the statistical uncertainties is shown in the bottom pad of the same figure. The number of iterations equal to 3 has been choosen as a compromise between reduction of bias and increase in statistical uncertainty. The difference with using 4 iterations is accounted in the systematic uncertainty and reported again in tables of section 6.4.4 labelled as "Unfolding".
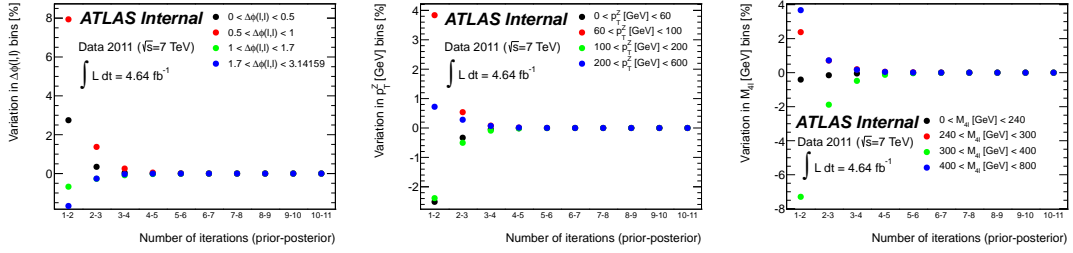
(a) Stability for $\Delta\phi(l,l)$ unfolding.

(b) Stability for p_T^Z unfolding.

(c) Stability for M_{4l} unfolding.
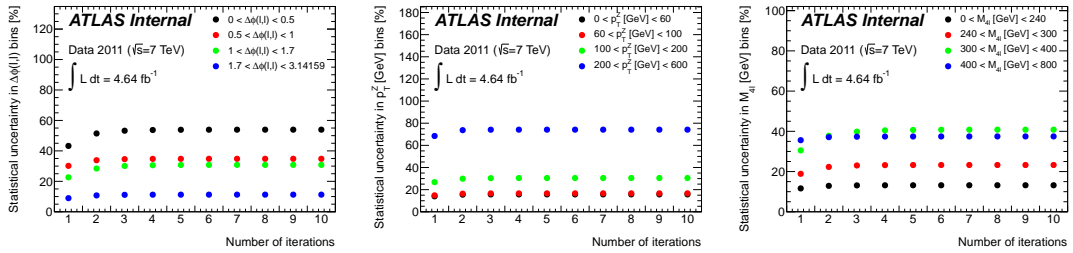
(d) Statistical uncert. for $\Delta\phi(l,l)$ unfolding.

(e) Statistical uncert. for p_T^Z unfolding.

(f) Statistical uncert. for M_{4l} unfolding.

Figure 6.6: Statbility and statistical uncertainty of the Bayesian unfolding in each bin as a function of the number of iterations.

6.4.4 Systematic Uncertainties

The systematic uncertainties on the unfolded distributions are reported in Tables 6.2, 6.3, 6.4. Since we measure normalized distributions, only the shape-dependent systematic effects are accounted for in these tables. The correlation matrices for systematics uncertainties are shown in Fig. 6.7.

Bins	(0, 60)	(60, 100)	(100 , 200)	(200 , 600)
$1/\sigma \; d\sigma/dp_T^Z$	0.42	0.39	0.16	0.03
	Uncertainties [%]			
Stat Unc.	15.68	16.61	30.39	74.13
Stat Unc.(MC)	0.52	0.59	1.04	2.49
Sys Unc.	1.13	0.77	2.54	3.25
Bkg Unc.	0.21	0.15	0.15	0.20
MC generator	0.59	0.28	2.08	1.19
Unfolding	0.05	0.08	0.09	0.07
Electron energy resolution	0.03	0.02	0.15	0.17
Electron energy scale	0.77	0.35	0.92	1.44
Electron id. efficiency	0.14	0.09	0.13	0.11
Electron isol. efficiency	0.07	0.03	0.08	0.14
Electron rec. efficiency	0.03	<0.01	0.02	0.15
Muon momentum resolution (MS)	0.02	0.08	0.11	0.25
Muon momentum resolution (ID)	0.05	0.05	0.13	0.82
Muon momentum scale	0.21	0.10	0.33	0.22
Muon isol. efficiency	0.05	0.03	0.07	<0.01
Muon rec. efficiency	0.04	0.02	0.07	0.04
Trig. efficiency	0.01	0.02	<0.01	0.04
Backgrounds	0.21	0.15	0.15	0.20

Table 6.2: Summary of statistical and systematic uncertainties represented as a percentage for the unfolded p_T^Z spectrum. Only shape-dependent systematic uncertainties are listed.

Bins	(0.00 , 0.50)	(0.50 , 1.00)	(1.00 , 1.70)	(1.70 , 3.14)
$1/\sigma \ d\sigma/d\Delta\phi$	0.07	0.14	0.18	0.61
	Uncertainties [%]			
Stat Unc.	53.24	34.58	30.09	11.14
Stat Unc.(MC)	2.76	2.21	1.41	0.52
Sys Unc.	5.10	3.28	3.87	0.56
Bkg Unc.	<0.01	0.14	0.12	0.07
MC generator	4.14	2.33	3.55	0.08
Unfolding	0.04	0.26	0.09	0.04
Electron energy resolution	0.26	0.25	0.05	0.04
Electron energy scale	0.55	0.46	0.47	0.09
Electron id. efficiency	0.11	0.04	<0.01	0.02
Electron isol. efficiency	0.07	<0.01	0.02	<0.01
Electron rec. efficiency	0.08	0.07	0.03	0.03
Muon momentum resolution (MS)	0.32	0.08	0.15	<0.01
Muon momentum resolution (ID)	0.82	0.08	0.08	0.05
Muon momentum scale	0.19	0.22	0.35	0.13
Muon isol. efficiency	<0.01	0.03	0.03	0.02
Muon rec. efficiency	0.04	0.07	0.02	0.02
Trig. efficiency	0.10	0.02	0.03	<0.01
Backgrounds	<0.01	0.14	0.12	0.07

Table 6.3: Summary of statistical and systematic uncertainties represented as a percentage for the unfolded $\Delta\phi(\ell,\ell)$ spectrum. Only shape-dependent systematic uncertainties are listed.

Bins	(0 , 240)	(240, 300)	(300 , 400)	(400 , 800)
$1/\sigma \; d\sigma/dM_{4l}$	0.52	0.27	0.10	0.11
	Uncertainties [%]			
Stat Unc.	13.12	23.03	39.85	37.34
Stat Unc.(MC)	0.44	0.79	1.21	1.46
Sys Unc.	2.00	2.15	1.65	3.70
Bkg Unc.	0.07	0.10	0.17	0.38
MC generator	1.61	1.57	0.39	3.13
Unfolding	0.05	0.20	0.48	0.17
Electron energy resolution	0.02	0.06	0.21	0.14
Electron energy scale	0.97	1.05	0.74	1.22
Electron id. efficiency	0.09	0.05	0.03	0.26
Electron isol. efficiency	0.03	0.02	<0.01	0.08
Electron rec. efficiency	0.06	<0.01	0.05	0.22
Muon momentum resolution (MS)	0.03	0.08	0.20	0.24
Muon momentum resolution (ID)	0.06	0.14	0.24	0.16
Muon momentum scale	0.47	0.62	0.41	0.27
Muon isol. efficiency	0.02	0.03	0.05	0.02
Muon rec. efficiency	0.03	0.01	0.05	0.07
Trig. efficiency	<0.01	<0.01	0.02	<0.01
Backgrounds	0.07	0.10	0.17	0.38

Table 6.4: Summary of statistical and systematic uncertainties represented as a percentage for the unfolded M_{4l} spectrum. Only shape-dependent systematic uncertainties are listed.
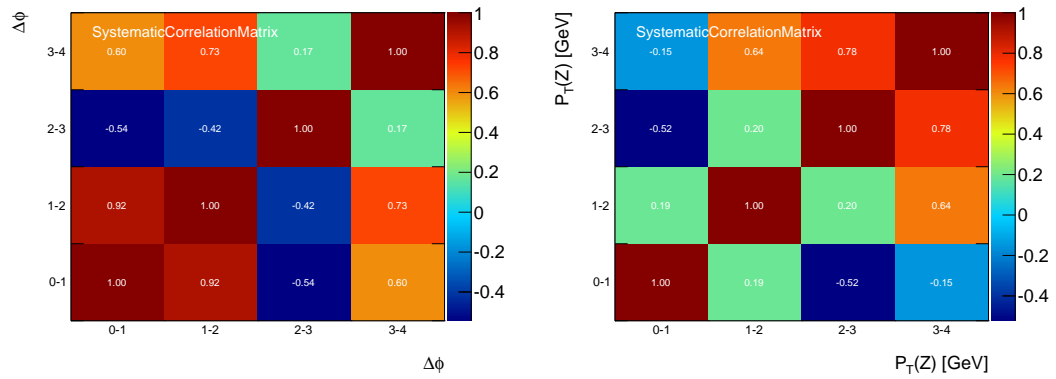
(a) Correlation matrices for $\Delta\phi(\ell,\ell)$ distribution.

(b) Correlation matrices for p_T^Z distribution.
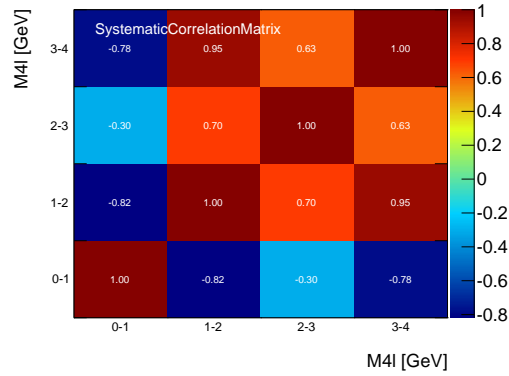
(c) Correlation matrices for M_{4l} distribution.

Figure 6.7: Correlation matrices for detector systematic uncertainties for $ZZ \to \ell^-\ell^+\ell^-\ell^+$.

6.5   Summary

In this chapter the unfolding of diffirential distributions for $ZZ \to \ell^- \ell^+ \ell^- \ell^+$ selection has been presented. The transverse momentum of the leading Z (p_T^Z), the angular difference between the two leptons forming the leading Z ($\Delta\phi(l, l)$), and the mass of the four leptons system (M_{4l}), were unfolded back to the underlying distributions using a Bayesian iterative algorithm, within the fiducial region. The uncertainty on the unfolded distributions is dominated by the statistical uncertainty, which is about 30% in most bins while the systematic uncertainty is no more than 5% in any bin.

The distributions reported in Fig. 6.2 are consistent with Standard Model prediction in each case.

Chapter 7

Limits on nTGC at ATLAS

7.1   Introduction to nTGC

In this chapter, a search for anomalous trilinear $ZZ\gamma^*$ and ZZZ couplings is presented. As alredy discussed in section 2.2 of **Chapter 2** and following the framework of Ref. [9], anomalous nTGCs for on-shell ZZ production can be parameterized by two CP-violating (f_4^V) and two CP-conserving (f_5^V) complex parameters (where $V = Z, \gamma$) which are zero in the Standard Model. Partial-wave unitarity is ensured by using a form-factor parameterization that causes the coupling to vanish at high parton center-of-mass energy $\sqrt{\hat{s}}$: $f_i^V = f_{i0}^V/(1 + \hat{s}/\Lambda^2)^n$. Here, Λ is the energy scale at which physics beyond the Standard Model will be directly observable, f_{i0}^V are the low-energy approximations of the couplings and n is the form-factor power. Values $n = 3$ and $\Lambda = 2$ TeV has been chosen for all cases. These values ensure that the limits are within the values provided by unitarity at LHC energies. Limits are also calculated for the case of not imposing a form factor parametrization ($\Lambda = \infty$).

7.2   nTGC Signature

The signature of anomalous neutral triple gauge couplings is enhanced cross section at high energies ($\hat{s}$) and at large scattering angles. Thus, observables which are proportional to the invariant mass of the diboson system and the gauge boson transverse momentum are particularly sensitive to contributions from anomalous couplings to the scattering amplitude. In ATLAS previous analysis with 1 fb^{-1}, limits on anomalous gauge boson couplings were determined using the ZZ cross section alone [34]. Using the 2011 data sample ($\sim$5 fb^{-1}) the limits on anomalous nTGCs presented in this thesis are determined using the observed and expected numbers of $ZZ \to \ell^-\ell^+\ell^-\ell^+$ events binned in p_T^Z (leading Z transverse momen-

	Expected background	Expected ZZ signal	Observed events
$ZZ \to \ell\ell\ell'\ell'$			
$0 < p_{\mathrm{T}}^Z < 60$ GeV	$0.6 \pm 0.8 \pm 0.5$	$27.9 \pm 0.2 \pm 2.0$	28
$60 < p_{\mathrm{T}}^Z < 100$ GeV	$0.2 \pm 0.2 \pm 0.2$	$14.6 \pm 0.2 \pm 1.2$	25
$100 < p_{\mathrm{T}}^Z < 200$ GeV	$0.1 \pm 0.1 \pm 0.1$	$9.3 \pm 0.1 \pm 0.9$	11
$p_{\mathrm{T}}^Z > 200$ GeV	$0.01 \pm 0.01 \pm 0.01$	$1.6 \pm 0.1 \pm 0.3$	2

Table 7.1: Total background, expected signal, and observed events as a function of the p_{T} of the leading Z for the $ZZ \to \ell^-\ell^+\ell^-\ell^+$ channel. For the expected signal and background events, the first uncertainty is statistical and the second is systematic.

tum), as reported in Tab. 7.1.

Figure 7.1 shows a comparison of the Z transverse momentum for standard model ZZ MC production (pink) and for samples, generated using SHERPA [16], including anomolous triple gauge couplings nTGC values close to the previous limits obtained by ATLAS. The same plot including also the oserved binned data distribution of Tab. 7.1 is shown in Fig. 7.2.
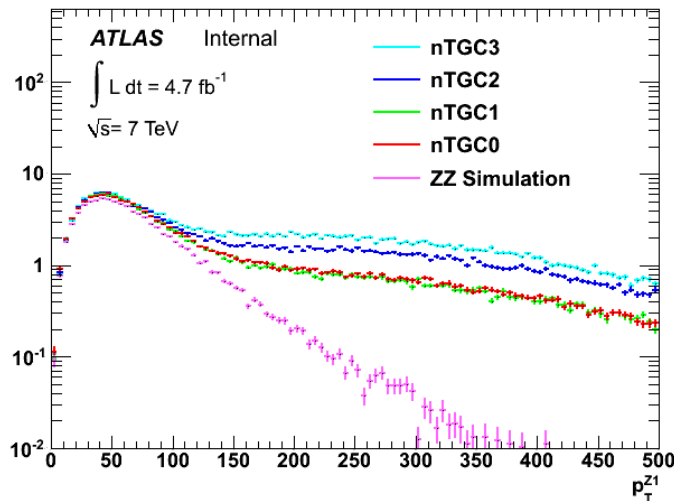
Figure 7.1: Z-boson transverse momentum for standard model ZZ (pink) and for samples including anomalous triple gauge couplings. The nTGC coupling parameters are set at values near the edge of the exclusion set in the 1 fb^{-1} analysis [34].

The dependency of the couplings on the expected number of events in each p_T^Z bin is parameterized using fully simulated events, generated with SHERPA [16],
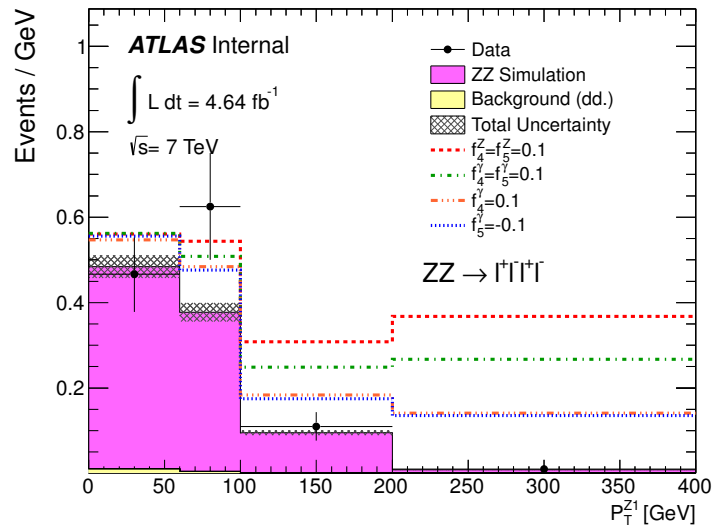
Figure 7.2: Leading Z p_T for 4 different aTGC samples set at values near the edge of the exclusion set in the 1 fb^{-1} analysis. The signal and background are also included in the plot.

subsequently reweighted using the Baur-Rainwater [9, 73] and BHO [74] MC generators, with the procedure described in the next section.

7.2.1   Matrix Element Reweighting Procedure

The matrix elements containing information on TGCs have been extracted from the next-to-leading order matrix elements from the BHO MC generator for $2 \to 5$ events and the Baur-Rainwater MC generator for $2 \to 4$ events [9, 74, 73] and introduced in a framework [75] that enables a calculation of the amplitude given the four vectors and PDG codes of the incoming partons and outgoing particles from the hard process.

In this way the reweighting framework works as an afterburner on existing MC events and can in principle be applied to any ZZ MC events as long as parton information from hard scattering is available. In the present analysis, the effects of anomalous contributions are studied by reweighting SHERPA MC events.

For ZZ production there are 4 anomalous couplings (f_i^V, $V = Z, \gamma^*$ and $i = 1, 2$). Since they enter linearly in the Lagrangian, they will appear quadratically

in the amplitude and the differential cross section can be written in bilinear form

$$
\begin{aligned}
\mathrm{d}\sigma_{\mathrm{SM+TGC}} \;=\;\; & F_{00} + f_4^\gamma F_{01} + f_4^Z F_{02} + f_5^\gamma F_{03} + f_5^Z F_{04} \\
+\;\; & \left(f_4^\gamma\right)^2 F_{11} + f_4^\gamma f_4^Z F_{12} + f_4^\gamma f_5^\gamma F_{13} + f_4^\gamma f_5^Z F_{14} \\
+\;\; & \left(f_4^Z\right)^2 F_{22} + f_4^Z f_5^\gamma F_{23} + f_4^Z f_5^Z F_{24} \\
+\;\; & \left(f_5^\gamma\right)^2 F_{33} + f_5^\gamma f_5^Z F_{34} \\
+\;\; & \left(f_5^Z\right)^2 F_{44}
\end{aligned}
\tag{7.1}
$$

where F_{ij} are coefficients out of which (F_{00}) corresponds to the SM operator contribution and the rest consist of operator contributions associated with the anomalous couplings.

Using this expansion, an event originating from SM sample can be reweighted to a TGC point by assigning the weight

$$
\mathrm{weight} = \frac{\mathrm{d}\sigma_{\mathrm{SM+TGC}}}{\mathrm{d}\sigma_{\mathrm{SM}}}
\tag{7.2}
$$

In practice, we reweight using a sample generated at a given TGC point to any other set of TGC values in order to cover the high p_T^Z tail of the phase space with better MC statistics.

For a specific sample of events the only thing that differs in the calculation of two different weights are the TGCs. The F_{ij}'s are completely specified by the kinematics of the participating particles and thus unaffected by a change of anomalous coupling. A recalculation of F_{ij} for different anomalous couplings is redundant.

A priori, there are 25 different coefficients. However, using the symmetry property of the coefficients ($F_{ij} = F_{ji}$), it is seen that only $25-10 = 15$ are independent. By using Eq. 7.1 it is possible to write down 15 equations that uniquely determine the coefficients F_{ij}.

To illustrate the procedure, consider the simplified situation where only one coupling constant exists. In this case, there are 3 coefficients to be determined as can be seen from the expression for the cross section

$$
\mathrm{d}\sigma_{\mathrm{SM+TGC}} = F_0 + f F_1 + f^2 F_2
\tag{7.3}
$$

where the notation has been slightly simplified (f is one of the four TGCs and $F_0 = \mathrm{d}\sigma_{\mathrm{SM}}$).

Using three different values of f, e.g $f = \{0, 1, -1\}$, three independent equations are written down (in matrix form)

$$
\begin{pmatrix} \mathrm{d}\sigma_1 \\ \mathrm{d}\sigma_2 \\ \mathrm{d}\sigma_3 \end{pmatrix} = \begin{bmatrix} 1 & 0 & 0 \\ 1 & 1 & 1 \\ 1 & -1 & 1 \end{bmatrix} \begin{pmatrix} F_0 \\ F_1 \\ F_2 \end{pmatrix}
\tag{7.4}
$$

Denoting the matrix containing the coupling values $\hat{A}$, the cross sections $\mathrm{d}\vec{\sigma}$ and the coefficients $\vec{F}$, the equations are easily manipulated to give the coefficients

$$\mathrm{d}\vec{\sigma} = \hat{A}\vec{F} \qquad \Rightarrow \qquad \vec{F} = \hat{A}^{-1}\mathrm{d}\vec{\sigma} \tag{7.5}$$

Clearly, $\hat{A}$ must be invertible. This is the case when the couplings are chosen such that the three equations in Eq. 7.4 are independent. When considering all four couplings at the same time, the matrix $\hat{A}$ is 15×15 and $\mathrm{d}\vec{\sigma}$ and $\vec{F}$ are 15-dimensional vectors.

We then calculate the yield coefficients for the given TGC parameters for our observable. We do that taking into account all the applied corrections in each event. This way we end up with 15 coefficients that can be translated into the yield coefficients multiplying the number of expected events by

$$F_{ij}/F_{00} \cdot N_{\text{expected}}. \tag{7.6}$$

Limits on the anomalous couplings are setted using both the total event yield and the differential yield, so both yield coefficients are reported.

Y_{SM}	$Y_{f_4^\gamma}$	$Y_{f_4^Z}$	$Y_{f_5^\gamma}$	$Y_{f_5^Z}$
53.41 ± 0.17	0.5 ± 0.2	-0.06 ± 0.4	5.6 ± 0.3	5.3 ± 0.5
	$Y_{f_4^\gamma f_4^\gamma}$	$Y_{f_4^\gamma f_4^Z}$	$Y_{f_4^\gamma f_5^\gamma}$	$Y_{f_4^\gamma f_5^Z}$
	3153.1 ± 20.0	2944.8 ± 22.2	-5.6 ± 7.9	-0.5 ± 4.4
	$Y_{f_4^Z f_4^Z}$	$Y_{f_4^Z f_5^\gamma}$	$Y_{f_4^Z f_5^Z}$	
	4518.7 ± 38.7	-0.5 ± 4.4	-2.4 ± 14.3	
	$Y_{f_5^\gamma f_5^\gamma}$	$Y_{f_5^\gamma f_5^Z}$		
	2904.7 ± 17.1	2709.6 ± 19.3		
	$Y_{f_5^Z f_5^Z}$			
	4161.6 ± 34.1			

Table 7.2: Yield coefficients for form factor $\Lambda = 2$ TeV and $n = 3$ for $ZZ \rightarrow \ell^-\ell^+\ell^-\ell^+$ calculated for the total number of events.

Tables 7.2 and 7.3 show the yield coefficients for the total number of events in the $ZZ \rightarrow \ell^-\ell^+\ell^-\ell^+$ channel and for each p_T. They were derived from a non-SM sample with TGC parameters set to $f_4^\gamma = 0.0$, $f_5^\gamma = -0.1$, $f_4^Z = 0.0$ and $f_5^Z = 0.0$.

	Y_{SM}	$Y_{f_4^\gamma}$	$Y_{f_4^Z}$	$Y_{f_5^\gamma}$	$Y_{f_5^Z}$
$0 < p_T^Z < 60$	27.93 ± 0.03	-0.02 ± 0.06	0.02 ± 0.12	-0.04 ± 0.08	1.7 ± 0.2
$60 < p_T^Z < 100$	14.63 ± 0.03	0.1 ± 0.1	0.3 ± 0.2	1.0 ± 0.1	0.5 ± 0.2
$100 < p_T^Z < 200$	9.28 ± 0.06	0.2 ± 0.1	-0.1 ± 0.3	3.5 ± 0.2	2.9 ± 0.4
$200 < p_T^Z$	1.55 ± 0.03	0.2 ± 0.1	-0.3 ± 0.2	1.4 ± 0.1	0.3 ± 0.3

	$Y_{f_4^\gamma f_4^\gamma}$	$Y_{f_4^\gamma f_4^Z}$	$Y_{f_4^\gamma f_5^\gamma}$	$Y_{f_4^\gamma f_5^Z}$
$0 < p_T^Z < 60$	46.5 ± 1.3	46.4 ± 1.1	-0.06 ± 0.2	-0.10 ± 0.1
$60 < p_T^Z < 100$	117.5 ± 2.6	114.0 ± 2.3	0.3 ± 0.5	0.4 ± 0.3
$100 < p_T^Z < 200$	726.6 ± 7.9	681.9 ± 7.4	3.0 ± 3.3	0.4 ± 1.5
$200 < p_T^Z$	2828.3 ± 10.9	2628.1 ± 18.2	-11.2 ± 9.0	-1.6 ± 5.1

	$Y_{f_4^Z f_4^Z}$	$Y_{f_4^Z f_5^\gamma}$	$Y_{f_4^Z f_5^Z}$
$0 < p_T^Z < 60$	74.3 ± 1.8	-0.1 ± 0.1	-0.3 ± 0.3
$60 < p_T^Z < 100$	177.6 ± 3.6	0.4 ± 0.3	0.7 ± 0.7
$100 < p_T^Z < 200$	1048.8 ± 12.4	0.4 ± 1.5	-0.6 ± 4.3
$200 < p_T^Z$	4022.7 ± 35.7	-1.6 ± 5.1	-2.9 ± 17.0

	$Y_{f_5^\gamma f_5^\gamma}$	$Y_{f_5^\gamma f_5^Z}$
$0 < p_T^Z < 60$	31.5 ± 1.1	31.6 ± 1.0
$60 < p_T^Z < 100$	87.1 ± 2.2	84.7 ± 2.1
$100 < p_T^Z < 200$	624.1 ± 6.4	585.7 ± 6.3
$200 < p_T^Z$	2702.1 ± 4.6	2509.0 ± 14.1

	$Y_{f_5^Z f_5^Z}$
$0 < p_T^Z < 60$	50.8 ± 1.6
$60 < p_T^Z < 100$	132.5 ± 3.3
$100 < p_T^Z < 200$	899.8 ± 10.9
$200 < p_T^Z$	3847.5 ± 29.4

Table 7.3: Yield coefficients for $\Lambda = 2$ TeV and $n = 3$ for $ZZ \to \ell^- \ell^+ \ell^- \ell^+$ calculated in each bin of p_T^Z.

7.2.2 nTGC Limits Extraction

Limits on the nTGC paramters are set using a maximum profile likelihood ratio following a frequentist limit approach [76]. The 95% C.L. interval for each anomalous coupling are determined separately with the other couplings set to their SM values. The full likelihood function for the TGC determination is a product of the Poisson probability distribution (P), with Gaussian terms (G) representing each of the nuisance parameters, and m is the number of bins. Since we have nuisance parameters for both signal and background, $\vec{\beta} = \{\beta_1, \beta_2, \ldots, \beta_{2m}\}$ are nuisance parameters which express the fractional uncertainty as:

$$\text{true } N_{\text{sig}}^i = N_{\text{sig}}^i \cdot (1 + \beta_i) \tag{7.7}$$

$$\text{true } N_{\text{bkg}}^i = N_{\text{bkg}}^i \cdot (1 + \beta_{i+m}) \tag{7.8}$$

The full likelihood function is given as:

$$L(\vec{x}, \vec{\beta}) = \prod_{i=1}^{m} P(N_{\text{data}}^i, \mu^i(\vec{x}, \vec{\beta})) \times \frac{1}{(2\pi)^m} e^{-\frac{1}{2}(\vec{\beta} \cdot C^{-1} \cdot \vec{\beta})}, \tag{7.9}$$

where

$$\mu^i(\vec{x}, \vec{\beta}) = N_{\text{sig}}^i(\vec{x})(1 + \beta_i) + N_{\text{bkg}}^i(1 + \beta_{i+m}). \tag{7.10}$$

and

$$N_{\text{sig}} = (Y_{\text{SM}} + Y_{f_i^V} \cdot f_i^V + Y_{f_i^V f_i^V} \cdot (f_i^V)^2) \cdot \mathcal{L} \cdot C_{ZZ}. \tag{7.11}$$

where the number of signal N_{sig} is expressed as a function of nTGC parameters using the reweighting procedure described in the previous section. The statistic ratio test $\text{R}(x)$ is constructed by taking the ratio of the profile maximum likelihood at a test nTGC parameter value $x = f_i^V$ to the full maximum likelihood. That is

$$R(x) = \frac{L(n|x, \hat{\hat{\beta}})}{L(n|\hat{x}, \hat{\beta})}. \tag{7.12}$$

where $\hat{\hat{\beta}}$ is the best estimator of β that maximizes the numerator for the fixed test value of x, and $\hat{x}$ and $\hat{\beta}$ are the values of x and β which maximize the denominator.

The observed value of the test statistic, $\text{R}_{obs}(x)$, is computed using the observed data n_{obs}. The same ratio is calculated for a large number of pseudo experiments for each test value of x, and compared with the observed $\text{R}_{obs}(x)$. A point is rejected if more than 95% of the pseudo-experiments have a larger profile likelihood ratio value than the one observed in data. In each pseudo-experiment, the number of "observed" data events in each bin is randomly sampled from a Poisson distribution with mean equal to the number of data N_{sig}^i and background N_{bkg}^i events in each bin which are allowed to flucuate gussianly within their uncertainties.

To find the expected sensitivity, the SM expectations for the signal and background were used to generate a large number of toy MC observed data sets. In this case, due to slow computation, the 95% confidence interval is calculated using the best fit value $\pm$ the errors computed by setting the delta log-likelihood to 1.92. The plots showing the expected limit results of the pseudo-experiments are shown in Fig. 7.3 using a form factor $\Lambda = 2$ TeV and in Fig. 7.4 without imposing it. In this plots the expected limits are computed also using the M_{4l} binned distributions which is shown to have less sensitivity to nTGC.

The obtained limits on the four couplings parameters are given in Tab. 7.4. Only the p_T^Z binned case is reported since again gives the best constraints.

		Coupling	f_4^γ	f_4^Z	f_5^γ	f_5^Z
No Form Factor	1 bin	expected	$[-0.039, 0.039] \pm 0.008$	$[-0.033, 0.033] \pm 0.007$	$[-0.039, 0.039] \pm 0.008$	$[-0.034, 0.033] \pm 0.007$
		observed	$[-0.051, 0.051]$	$[-0.043, 0.044]$	$[-0.053, 0.052]$	$[-0.045, 0.044]$
	4 Z p_T bins	expected	$[-0.017, 0.017] \pm 0.005$	$[-0.015, 0.015] \pm 0.004$	$[-0.017, 0.017] \pm 0.005$	$[-0.015, 0.015] \pm 0.004$
		observed	$[-0.020, 0.020]$	$[-0.017, 0.017]$	$[-0.020, 0.020]$	$[-0.017, 0.017]$
Form Factor	1 bin	expected	$[-0.076, 0.076] \pm 0.015$	$[-0.063, 0.063] \pm 0.014$	$[-0.080, 0.078] \pm 0.016$	$[-0.067, 0.065] \pm 0.014$
		observed	$[-0.101, 0.100]$	$[-0.084, 0.084]$	$[-0.106, 0.104]$	$[-0.088, 0.087]$
	4 Z p_T bins	expected	$[-0.038, 0.038] \pm 0.010$	$[-0.031, 0.032] \pm 0.008$	$[-0.039, 0.038] \pm 0.010$	$[-0.032, 0.032] \pm 0.008$
		observed	$[-0.044, 0.044]$	$[-0.037, 0.037]$	$[-0.045, 0.045]$	$[-0.037, 0.038]$

Table 7.4: One dimensional 95% CL limits on the anomalous gauge boson couplings in the $ZZ \to \ell^-\ell^+\ell^-\ell^+$ channel, where the limit for each coupling assumes the other couplings fixed at their SM value. Both the expected and observed limits are shown.

(a) f_γ^4

(b) f_Z^4

(c) f_γ^5

(d) f_Z^5
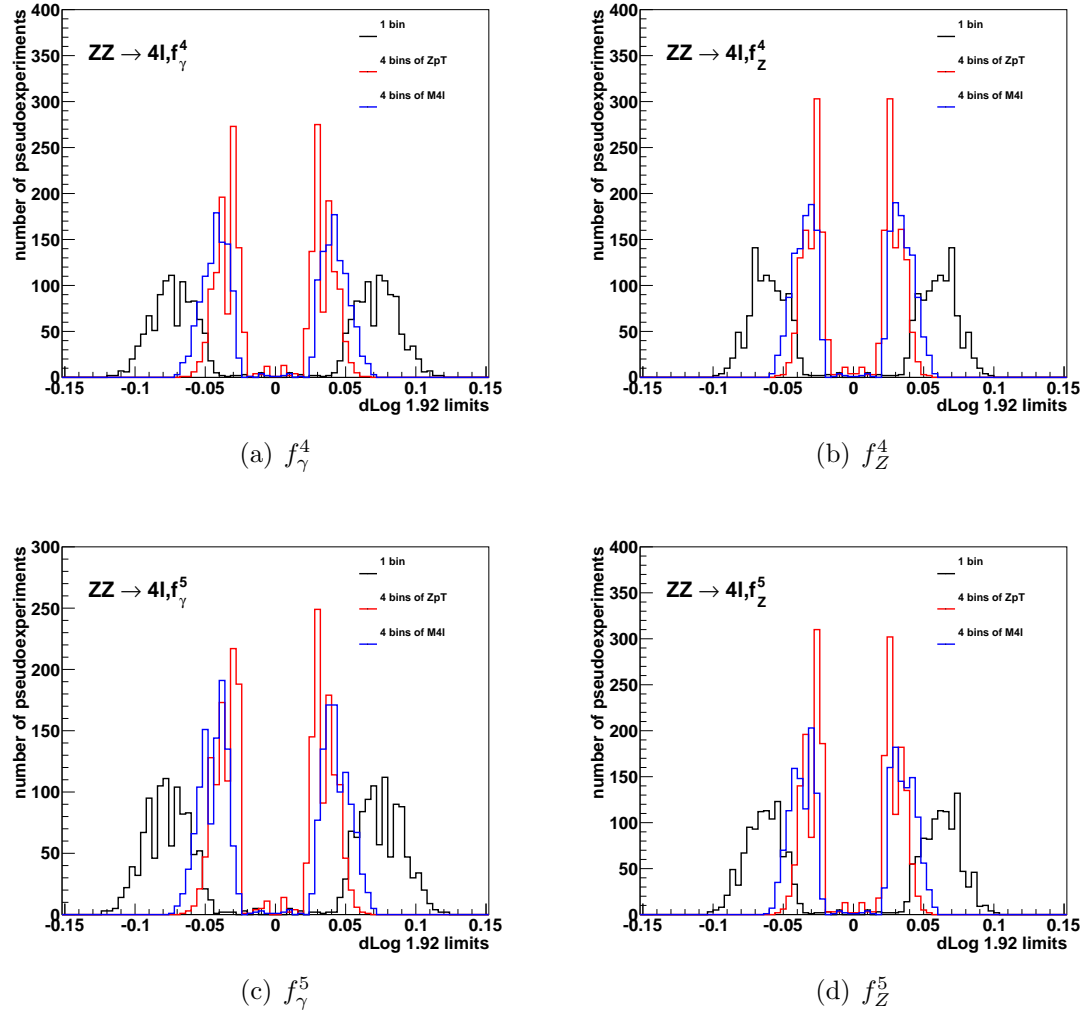
Figure 7.3: 95% confidence intervals corresponding to limits extracted by setting delta log-likelihood = 1.92 in 1000 toy experiments for nTGC parameters. The distribution of widths extracted for different observables are compared for one versus several bins. A form factor scale of $\Lambda = 2$ TeV and $n = 3$ has been used in the pseudo-experiments.

(a) f_γ^4

(b) f_Z^4

(c) f_γ^5

(d) f_Z^5
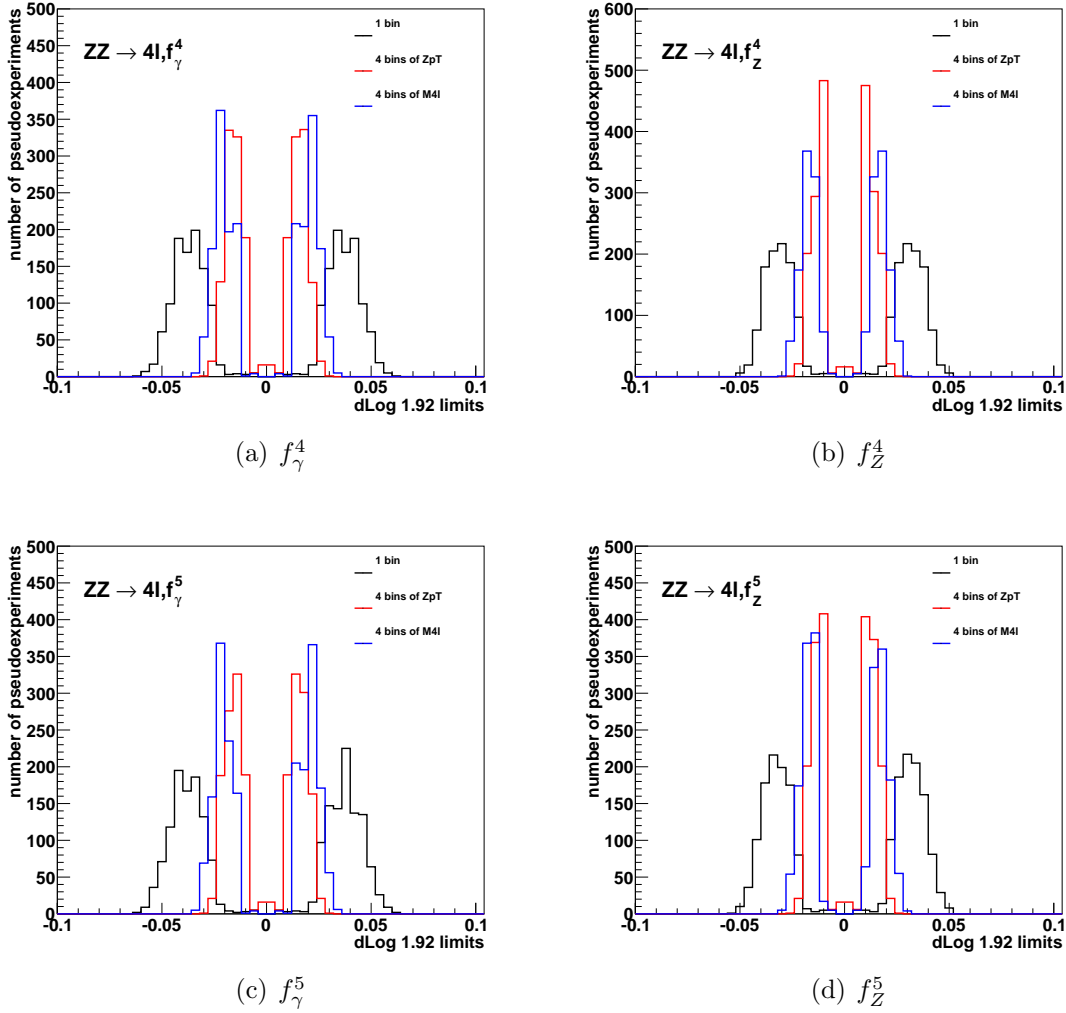
Figure 7.4: The 95% confidence interval widths corresponding to limits extracted by setting delta log-likelihood = 1.92 in 1000 toy experiments for nTGC parameters. The distribution of widths extracted from different observables are compared. No form factor scale has been used (i.e. $\Lambda = \infty$ or equivalently $n = 0$)

7.3 Summary

In this chapter the extraction procedure of nTGC limits has been presented. The event yields as a function of the leading Z transverse momentum p_T^Z of the $ZZ \to \ell^- \ell^+ \ell^- \ell^+$ selection is used to derive 95% confidence intervals for anomalous neutral triple gauge boson couplings by performing a maximum profile likelihood ratio. The limits on the ZZ anomalous triple gauge couplings derived are more than 5 times better than the ones derived in the previous ATLAS paper [34]. No deviation from the SM is observed.

In the ATLAS paper of recent pubblication [67] the same limits are derived combining both $ZZ \to \ell^- \ell^+ \ell^- \ell^+$ and $ZZ \to \ell^- \ell^+ \nu \bar{\nu}$ channels. The results compared with other experiments are shown in Fig. 7.5.
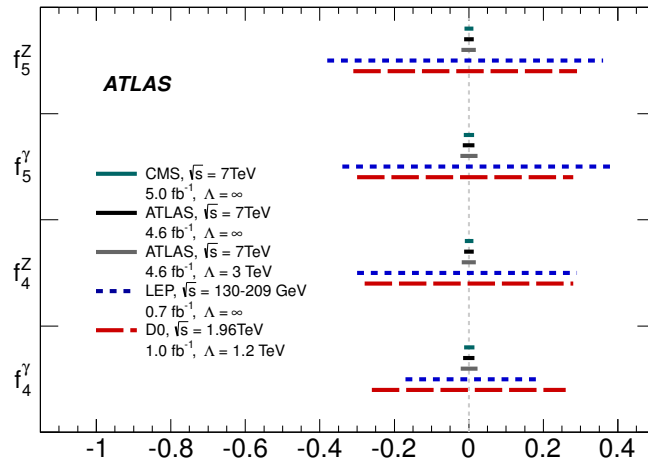
Figure 7.5: Anomalous nTGC 95% confidence intervals from LHC, LEP [36] and Tevatron [37] experiments. Integrated luminosities, centre-of-mass energy and cut-off Λ for each experiment are shown.

Conclusions

The work presented in this thesis is focused on the measurement of the $ZZ \to \ell^-\ell^+\ell^-\ell^+$ production cross-section with the ATLAS detector in LHC proton-proton collisions at $\sqrt{s} = 7$ TeV, performed using electrons and muons in the final state. In a dataset with an integrated luminosity of 4.64 fb^{-1} a total of 66 ZZ and 84 ZZ^* candidates are observed with a background expectation of $0.9 \pm 1.1 \pm 0.7$ and $9.1 \pm 2.3 \pm 1.3$. The Standard Model expectation for the number of signal events is $53.4 \pm 0.3 \pm 2.2$ for the ZZ and $64.4 \pm 0.4 \pm 4.6$ for the ZZ^* case.

The fiducial cross-sections are determined to be

$$\sigma^{\text{fid}}_{ZZ \to \ell^-\ell^+\ell^-\ell^+} = 25.4^{+3.3}_{-3.0}(\text{stat.})^{+1.2}_{-1.0}(\text{syst.}) \pm 1.0(\text{lumi.})(\text{fb})$$

$$\sigma^{\text{fid}}_{ZZ^* \to \ell^-\ell^+\ell^-\ell^+} = 29.8^{+3.8}_{-3.5}(\text{stat.})^{+1.7}_{-1.5}(\text{syst.}) \pm 1.2(\text{lumi.})(\text{fb})$$

In the ZZ selection with both Z on-shell the total cross section was determined to be

$$\sigma^{\text{tot}}_{\text{ZZ}} = 7.0^{+0.9}_{-0.8}(\text{stat.})^{+0.4}_{-0.3}(\text{syst.}) \pm 0.3(\text{lumi.})(\text{pb})$$

The result is consistent with the MCFM NLO Standard Model prediction of $5.89^{+0.22}_{-0.18}$ pb, calculated with Z bosons with a mass between 66 and 116 GeV.

Then, the transverse momentum of the leading Z (p_T^Z), the angular difference between the two leptons forming the leading Z ($\Delta\phi(l,l)$), and the mass of the four leptons system (M_{4l}), were unfolded back to the underlying distributions using a Bayesian iterative algorithm, within the fiducial region. The uncertainty on the unfolded distributions is dominated by the statistical uncertainty, which is about 30% in most bins while the systematic uncertainty is no more than 5% in any bin. The distributions reported are consistent with Standard Model and no deviation from the prediction has been observed in each case.

Finally, the extraction procedure of nTGC limits is presented. The event yields as a function of the leading Z transverse momentum p_T^Z of the $ZZ \to \ell^-\ell^+\ell^-\ell^+$ selection is used to derive 95% confidence intervals for anomalous neutral triple gauge boson couplings by performing a maximum profile likelihood ratio. The limits on the ZZ anomalous triple gauge couplings derived improve Tevatron and

LEP results and are more than 5 times better than the ones derived in the previous ATLAS measurement using 1 fb^{-1}. No deviation from the prediction of the SM is observed.

Appendix A

MC Background Tables

In the following tables are reported the simulated background processes used in the $ZZ \to \ell^-\ell^+\ell^-\ell^+$ analysis and described in section 4.2.3 of **Chapter 4**. The cross section values, generator names, generator level filter efficiencies and total number of events of each process are shown.

MCID	Process	Generator	events	k-factor	ϵ_{filter}	cross section [pb]
107650	ZeeNp0	ALPGEN/JIMMY	6368284	1.25	1.0	668.32
107651	ZeeNp1	ALPGEN/JIMMY	1334897	1.25	1.0	134.36
107652	ZeeNp2	ALPGEN/JIMMY	809999	1.25	1.0	40.54
107653	ZeeNp3	ALPGEN/JIMMY	220000	1.25	1.0	11.16
107654	ZeeNp4	ALPGEN/JIMMY	60000	1.25	1.0	2.88
107655	ZeeNp5	ALPGEN/JIMMY	20000	1.25	1.0	0.83
107660	Z$\mu\mu$Np0	ALPGEN/JIMMY	6615230	1.25	1.0	668.68
107661	Z$\mu\mu$Np1	ALPGEN/JIMMY	1334296	1.25	1.0	134.14
107662	Z$\mu\mu$Np2	ALPGEN/JIMMY	404947	1.25	1.0	40.33
107663	Z$\mu\mu$Np3	ALPGEN/JIMMY	110000	1.25	1.0	11.19
107664	Z$\mu\mu$Np4	ALPGEN/JIMMY	30000	1.25	1.0	2.75
107665	Z$\mu\mu$Np5	ALPGEN/JIMMY	10000	1.25	1.0	0.77
107670	Z$\tau\tau$Np0	ALPGEN/JIMMY	10613179	1.25	1.0	668.40
107671	Z$\tau\tau$Np1	ALPGEN/JIMMY	1999491	1.25	1.0	134.81
107672	Z$\tau\tau$Np2	ALPGEN/JIMMY	404950	1.25	1.0	40.36
107673	Z$\tau\tau$Np3	ALPGEN/JIMMY	509847	1.25	1.0	11.25
107674	Z$\tau\tau$Np4	ALPGEN/JIMMY	29999	1.25	1.0	2.79
107675	Z$\tau\tau$Np5	ALPGEN/JIMMY	45000	1.25	1.0	0.77
116250	ZeeNp0 M10to40 pt20	ALPGEN/JIMMY	994949	1.22	1.0	3051.6
116251	ZeeNp1 M10to40 pt20	ALPGEN/JIMMY	299998	1.22	1.0	87.87
116252	ZeeNp2 M10to40 pt20	ALPGEN/JIMMY	499997	1.22	1.0	41.40
116253	ZeeNp3 M10to40 pt20	ALPGEN/JIMMY	149998	1.22	1.0	8.38
116254	ZeeNp4 M10to40 pt20	ALPGEN/JIMMY	40000	1.22	1.0	1.85
116255	ZeeNp5 M10to40 pt20	ALPGEN/JIMMY	10000	1.22	1.0	0.46
116260	Z$\mu\mu$Np0 M10to40 pt20	ALPGEN/JIMMY	999849	1.22	1.0	3051.6
116261	Z$\mu\mu$Np1 M10to40 pt20	ALPGEN/JIMMY	300000	1.22	1.0	84.87
116262	Z$\mu\mu$Np2 M10to40 pt20	ALPGEN/JIMMY	999994	1.22	1.0	41.45
116263	Z$\mu\mu$Np3 M10to40 pt20	ALPGEN/JIMMY	150000	1.22	1.0	8.38
116264	Z$\mu\mu$Np4 M10to40 pt20	ALPGEN/JIMMY	39999	1.22	1.0	1.85
116265	Z$\mu\mu$Np5 M10to40 pt20	ALPGEN/JIMMY	10000	1.22	1.0	0.46
116270	Z$\tau\tau$Np0 M10to40 pt20	ALPGEN/JIMMY	999649	1.22	1.0	3055.1
116271	Z$\tau\tau$Np1 M10to40 pt20	ALPGEN/JIMMY	299999	1.22	1.0	84.93
116272	Z$\tau\tau$Np2 M10to40 pt20	ALPGEN/JIMMY	498899	1.22	1.0	41.47
116273	Z$\tau\tau$Np3 M10to40 pt20	ALPGEN/JIMMY	150000	1.22	1.0	8.36
116274	Z$\tau\tau$Np4 M10to40 pt20	ALPGEN/JIMMY	39999	1.22	1.0	1.85
116275	Z$\tau\tau$Np5 M10to40 pt20	ALPGEN/JIMMY	10000	1.22	1.0	0.46

Table A.1: MC samples/processes used to model Z+X, including Z+jets and Drell-Yan samples. The corresponding cross sections, generator names, generator level filter efficiencies and total numbers of events are shown in this table. NpX (X=0...5) in the process name refers to the number of additional partons in the final state.

MCID	Process	Generator	events	k-factor	ϵ_{filter}	cross section [pb]
107680	W$e\nu$Np0	ALPGEN	3358884	1.2	1.0	6921.6
107681	W$e\nu$Np1	ALPGEN	2499645	1.2	1.0	1304.3
107682	W$e\nu$Np2	ALPGEN	3768632	1.2	1.0	378.29
107683	W$e\nu$Np3	ALPGEN	1008947	1.2	1.0	101.43
107684	W$e\nu$Np4	ALPGEN	250000	1.2	1.0	25.87
107685	W$e\nu$Np5	ALPGEN	69999	1.2	1.0	7.0
107690	W$\mu\nu$Np0	ALPGEN	3462942	1.2	1.0	6919.6
107691	W$\mu\nu$Np1	ALPGEN	2498593	1.2	1.0	1304.2
107692	W$\mu\nu$Np2	ALPGEN	3768737	1.2	1.0	377.83
107693	W$\mu\nu$Np3	ALPGEN	1008446	1.2	1.0	101.88
107694	W$\mu\nu$Np4	ALPGEN	254950	1.2	1.0	25.75
107695	W$\mu\nu$Np5	ALPGEN	70000	1.2	1.0	6.92
107700	W$\tau\nu$Np0	ALPGEN	3418296	1.2	1.0	6918.6
107701	W$\tau\nu$Np1	ALPGEN	2499194	1.2	1.0	1303.2
107702	W$\tau\nu$Np2	ALPGEN	3750986	1.2	1.0	378.18
107703	W$\tau\nu$Np3	ALPGEN	1009946	1.2	1.0	101.51
107704	W$\tau\nu$Np4	ALPGEN	249998	1.2	1.0	25.64
107705	W$\tau\nu$Np5	ALPGEN	65000	1.2	1.0	7.04

Table A.2: MC samples/processes used to model W+jets. The corresponding cross sections, generator names, generator level filter efficiencies and total numbers of events are shown in this table. NpX (X=0...5) in the process name refers to the number of additional partons in the final state.

MCID	Process	Generator	events	k-factor	ϵ_{filter}	cross section [pb]
105200	$t\bar{t}$	MC@NLO	14983835	1.0	0.55551	164.57
117360	t-channel$\rightarrow$e	MC@NLO	994897	1.0	1.0	6.94
117361	t-channel$\rightarrow \mu$	MC@NLO	999295	1.0	1.0	6.83
117362	t-channel$\rightarrow \tau$	MC@NLO	999948	1.0	1.0	7.26
117363	s-channel$\rightarrow$e	MC@NLO	199899	1.0	1.0	0.498
117364	s-channel$\rightarrow \mu$	MC@NLO	199850	1.0	1.0	0.498
117365	s-channel$\rightarrow \tau$	MC@NLO	190000	1.0	1.0	0.498
105500	Wt	MC@NLO	994897	1.0	1.0	15.74
105757	bbcc μ10μ10X	PYTHIAB	296599	1.0	1.0	2830.3
105758	bbcc μ10e10X	PYTHIAB	795695	1.0	1.0	4017.1
105759	bbcc e10e10X	PYTHIAB	2920985	1.0	1.0	1693.0

Table A.3: MC samples/processes used to model top (including $t\bar{t}$ and single top) and dijet backgrounds. The corresponding cross sections, generator names, generator level filter efficiencies and total numbers of events are shown in the table.

MCID	Process	Generator	events	k-factor	ϵ_{filter}	cross section [pb]
105985	WW	HERWIG	50000	1.52	0.38863	29.592
105986	ZZ	HERWIG	50000	1.41	0.21152	4.6
105987	WZ	HERWIG	50000	1.58	1.0	3.432
117410	γWNp0	ALPGEN	210000	1.432	1.0	213.06
117411	γWNp1	ALPGEN	265000	1.432	1.0	52.199
117412	γWNp2	ALPGEN	175000	1.432	1.0	17.259
117413	γWNp3	ALPGEN	264999	1.432	1.0	5.3361
117414	γWNp4	ALPGEN	64999	1.432	1.0	1.3762
117415	γWNp5	ALPGEN	20000	1.432	1.0	0.3382
128850	γ^{*}W$(\ell\nu ee)$	PYTHIA,MADGRAPH	294999	1.0	1.0	4.80130
128851	γ^{*}W$(\ell\nu\mu\mu)$	PYTHIA,MADGRAPH	149900	1.0	1.0	1.45360
128852	γ^{*}W$(\ell\nu\tau\tau)$	PYTHIA,MADGRAPH	50000	1.0	1.0	0.21330
108323	γZ(ee)	PYTHIA,MADGRAPH	50000	1.41	1.0	9.63
108324	γZ$(\mu\mu)$	PYTHIA,MADGRAPH	50000	1.41	1.0	9.63
108325	γZ$(\tau\tau)$	PYTHIA,MADGRAPH	50000	1.41	0.15	9.41
105940	W^{+}Z$\to$lνqq	MC@NLO	25000	1.0	1.0	1.6889
105941	W^{+}Z$\to$lνll	MC@NLO	25000	1.0	1.0	0.15924
105942	W^{+}Z$\to$qqll	MC@NLO	24950	1.0	1.0	0.49836
106024	W^{+}Z$\to \tau\nu$ll	MC@NLO	25000	1.0	1.0	0.07962
106025	W^{+}Z$\to$l$\nu\tau\tau$	MC@NLO	25000	1.0	1.0	0.07962
106026	W^{+}Z$\to \tau\nu\tau\tau$	MC@NLO	24950	1.0	1.0	0.03981
106027	W^{-}Z$\to \tau\nu$ll	MC@NLO	25000	1.0	1.0	0.04302
106028	W^{-}Z$\to$l$\nu\tau\tau$	MC@NLO	25000	1.0	1.0	0.04302
106029	W^{-}Z$\to \tau\nu\tau\tau$	MC@NLO	25000	1.0	1.0	0.02151
105970	W^{-}Z$\to$lνqq	MC@NLO	25000	1.0	1.0	0.91264
105971	W^{-}Z$\to$lνll	MC@NLO	100000	1.0	1.0	0.08605
105972	W^{-}Z$\to$qqll	MC@NLO	100000	1.0	1.0	0.2693
113190	W^{+}Z$\to$qq$\tau\tau$	MC@NLO	25000	1.0	1.0	0.24918
113191	W^{-}Z$\to$qq$\tau\tau$	MC@NLO	25000	1.0	1.0	0.13465
105921	qq$\to$W^{+}W$^{-}\to$ee$\nu\nu$	MC@NLO	199949	1.0	1.0	0.503
105922	qq$\to$W^{+}W$^{-}\to$e$\mu\nu\nu$	MC@NLO	200000	1.0	1.0	0.503
105923	qq$\to$W^{+}W$^{-}\to$e$\tau\nu\nu$	MC@NLO	200000	1.0	1.0	0.503
105924	qq$\to$W^{+}W$^{-}\to \mu\mu\nu\nu$	MC@NLO	199000	1.0	1.0	0.503
105925	qq$\to$W^{+}W$^{-}\to \mu$e$\nu\nu$	MC@NLO	199949	1.0	1.0	0.503
105926	qq$\to$W^{+}W$^{-}\to \mu\tau\nu\nu$	MC@NLO	200000	1.0	1.0	0.503
105927	qq$\to$W^{+}W$^{-}\to \tau\tau\nu\nu$	MC@NLO	199678	1.0	1.0	0.503
105928	qq$\to$W^{+}W$^{-}\to \tau$e$\nu\nu$	MC@NLO	199950	1.0	1.0	0.503
105929	qq$\to$W^{+}W$^{-}\to \tau\mu\nu\nu$	MC@NLO	200000	1.0	1.0	0.503
106011	gg$\to$W^{+}W$^{-}\to$ee$\nu\nu$	gg2ww	10000	1.0	0.99	0.0145
106012	gg$\to$W^{+}W$^{-}\to$e$\mu\nu\nu$	gg2ww	10000	1.0	0.99	0.0145
106013	gg$\to$W^{+}W$^{-}\to$e$\tau\nu\nu$	gg2ww	10000	1.0	0.92	0.0145
106014	gg$\to$W^{+}W$^{-}\to \mu\mu\nu\nu$	gg2ww	9999	1.0	0.99	0.0145
106015	gg$\to$W^{+}W$^{-}\to \mu$e$\nu\nu$	gg2ww	10000	1.0	0.99	0.0145
106016	gg$\to$W^{+}W$^{-}\to \mu\tau\nu\nu$	gg2ww	10000	1.0	0.93	0.0145
106017	gg$\to$W^{+}W$^{-}\to \tau\tau\nu\nu$	gg2ww	10000	1.0	0.33	0.0145
106018	gg$\to$W^{+}W$^{-}\to \tau$e$\nu\nu$	gg2ww	10000	1.0	0.92	0.0145
106019	gg$\to$W^{+}W$^{-}\to \tau\mu\nu\nu$	gg2ww	10000	1.0	0.93	0.0145

Table A.4: MC samples/processes used to model diboson backgrounds, including WW, $W\gamma$ and $Z\gamma$. The corresponding cross sections, generator names, generator level filter efficiencies and total numbers of events are shown in the table.

Appendix B

$ZZ \to \ell^- \ell^+ \ell^- \ell^+$ Kinematic Distributions per Channel

Figures B.1, B.3 and B.5 show distributions of $M^{\text{leading Z}}$, $M^{\text{subleading Z}}$, $p_{\text{T}}^{\text{leading Z}}$, $p_{\text{T}}^{\text{subleading Z}}$, p_{T}^{ZZ}, and M^{ZZ} for the final $ZZ \to \ell^- \ell^+ \ell^- \ell^+$ candidates in the $e^+ e^- e^+ e^-$ $\mu^+ \mu^- \mu^+ \mu^-$ and $e^+ e^- \mu^+ \mu^-$ final-states, respectively, for the selection allowing one Z to be off-shell ($m^{Z2} > 20$ GeV). Figures B.2, B.4 and B.6 show the same distributions for events passing the ZZ selection (66 GeV $< m^{Z2} < 116$ GeV), again for the $e^+ e^- e^+ e^-$ $\mu^+ \mu^- \mu^+ \mu^-$ and $e^+ e^- \mu^+ \mu^-$ final-states, respectively.

In all plots, the points are data and the stacked histograms shows the signal and background prediction from simulation, normalized to the luminosity of the data. The gray band indicates the combined statistical and systematic uncertainty on the signal prediction.
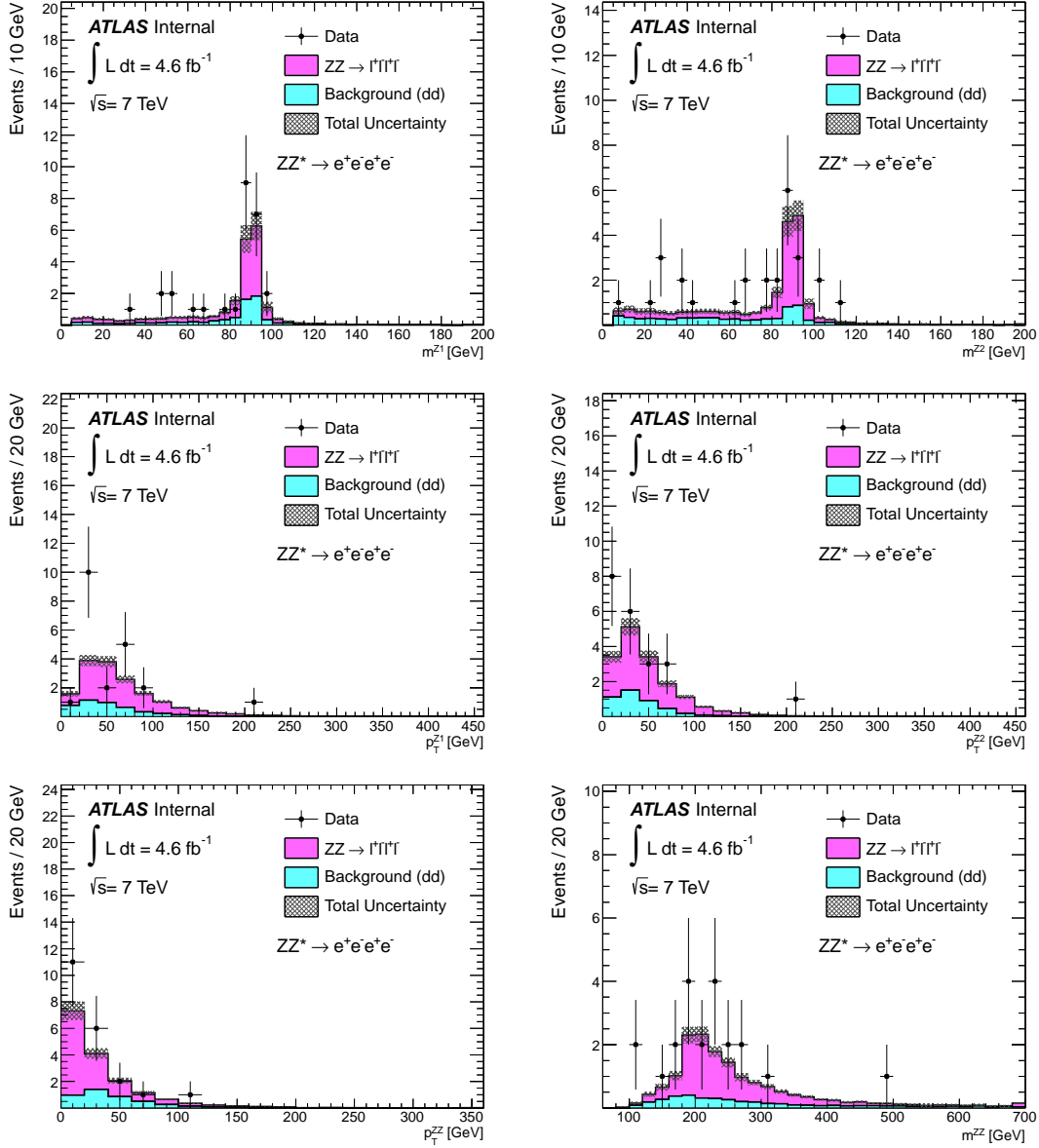
Figure B.1: Kinematic distributions for $ZZ \to \ell^-\ell^+\ell^-\ell^+$ candidates in the $e^+e^-e^+e^-$ final-state, allowing one Z to be off shell (ZZ^* selection). The top row shows $M^{leading\ Z}$ (left) and $M^{subleading\ Z}$ (right), without any cut on the distribution being plotted. The second row shows $p_T^{leading\ Z}$ (middle left) and $p_T^{subleading\ Z}$ (right) and finally the third row p_T^{ZZ} (left) and M^{ZZ} (right).

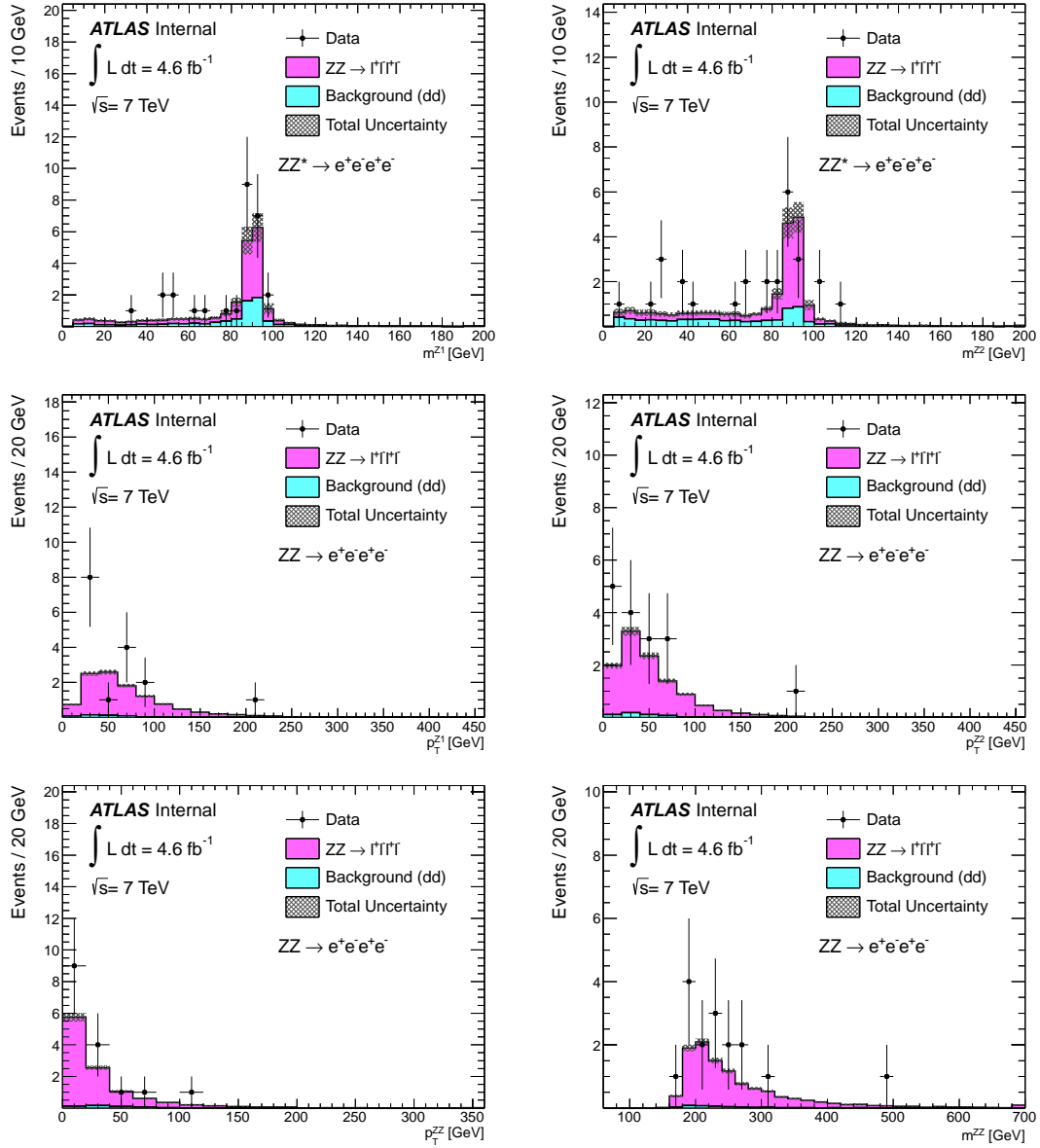**Figure B.2:** Kinematic distributions for $ZZ \to \ell^-\ell^+\ell^-\ell^+$ candidates in the $e^+e^-e^+e^-$ final state, applying the on-shell (ZZ) selection. The top row shows $M^{leading\ Z}$ (left) and $M^{subleading\ Z}$ (right), without any cut on the distribution being plotted. The second row shows $p_T^{leading\ Z}$ (middle left) and $p_T^{subleading\ Z}$ (right) and finally the third row p_T^{ZZ} (left) and M^{ZZ} (right).
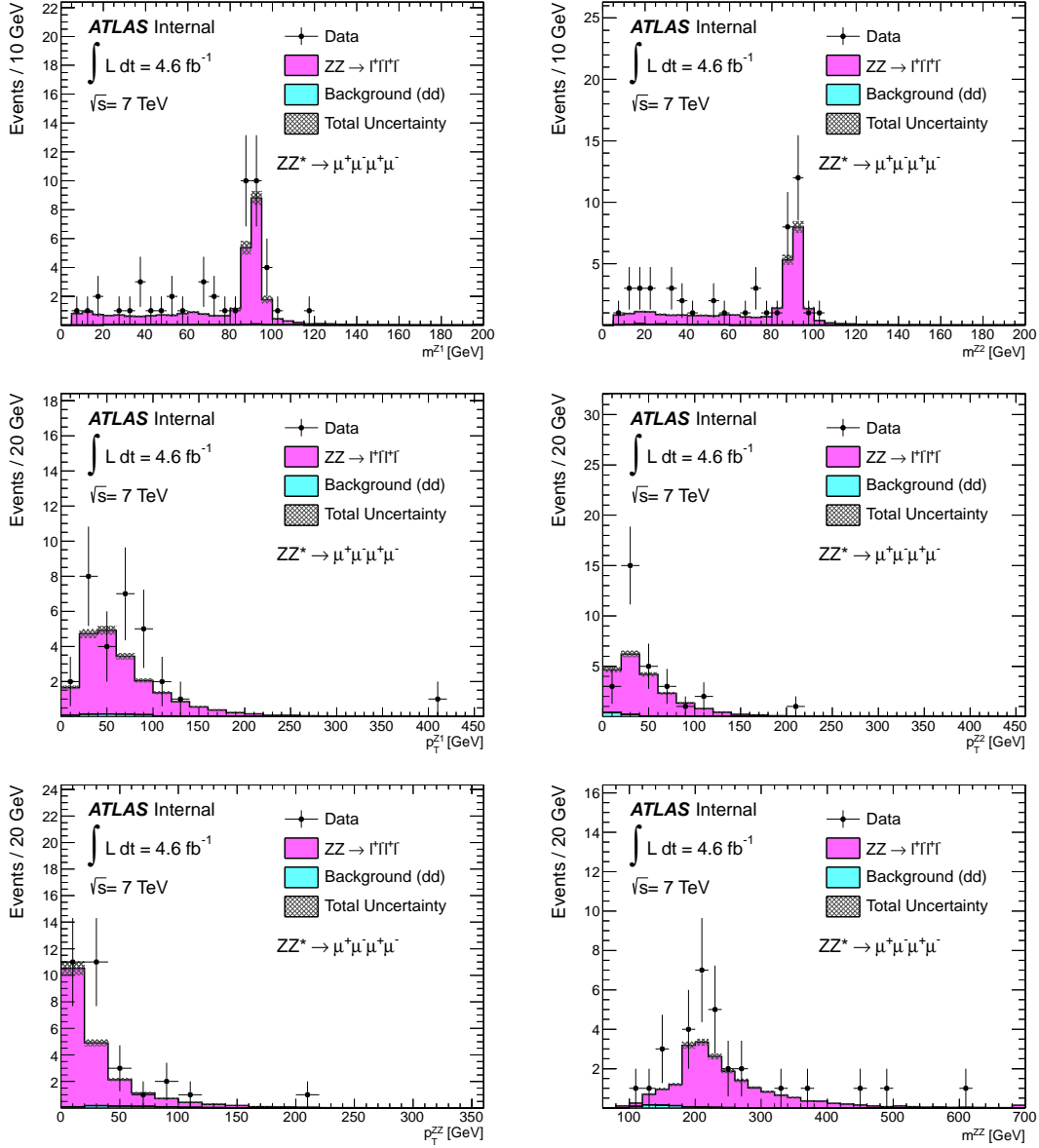
Figure B.3: Kinematic distributions for $ZZ \to \ell^-\ell^+\ell^-\ell^+$ candidates in the $\mu^+\mu^-\mu^+\mu^-$ final-state, allowing one Z to be off shell (ZZ^* selection). The top row shows $M^{leading\ Z}$ (left) and $M^{subleading\ Z}$ (right), without any cut on the distribution being plotted. The second row shows $p_T^{leading\ Z}$ (middle left) and $p_T^{subleading\ Z}$ (right) and finally the third row p_T^{ZZ} (left) and M^{ZZ} (right).
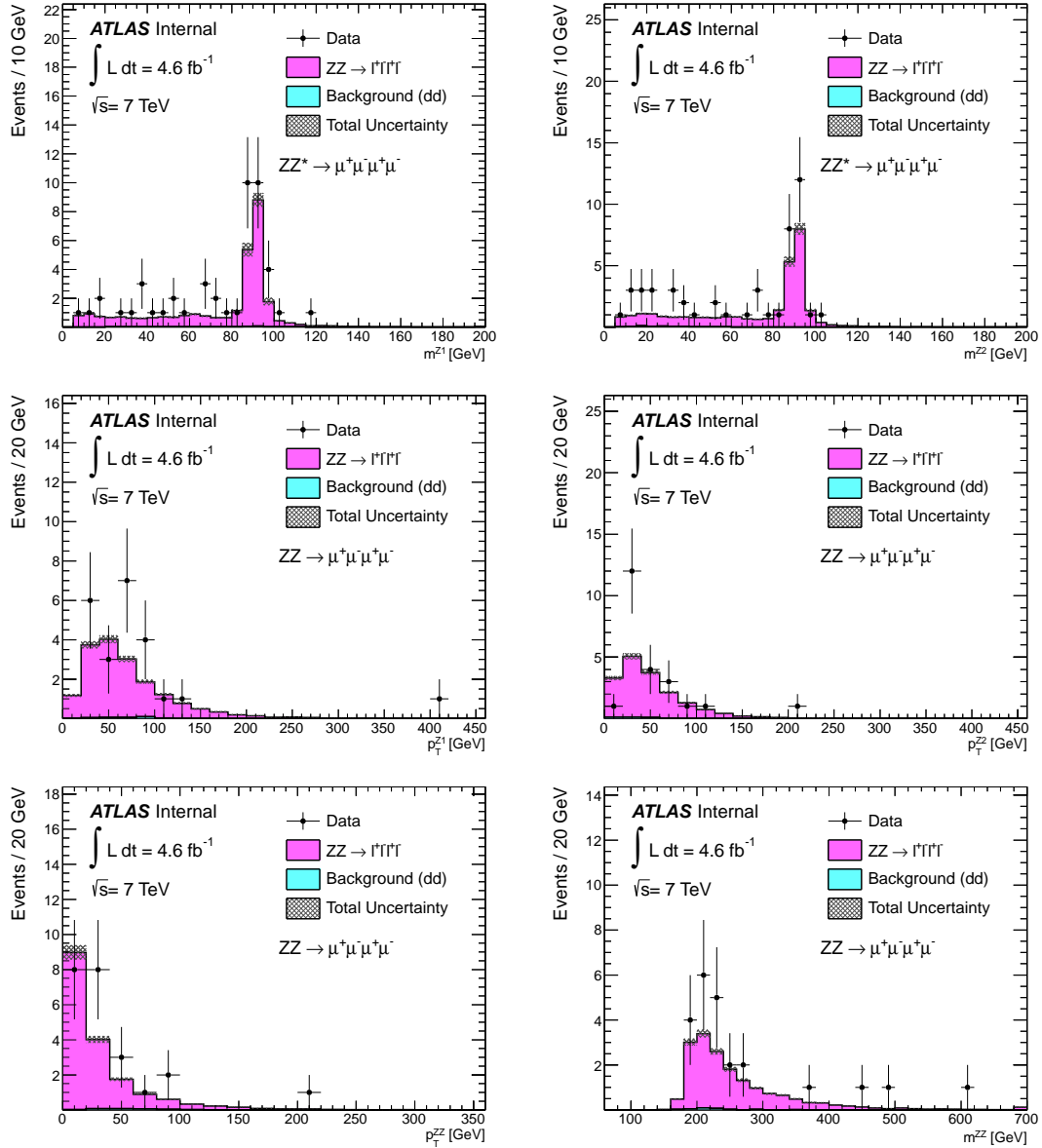
Figure B.4: Kinematic distributions for $ZZ \to \ell^-\ell^+\ell^-\ell^+$ candidates in the $\mu^+\mu^-\mu^+\mu^-$ final state, applying the on-shell (ZZ) selection. The top row shows $M^{leading\ Z}$ (left) and $M^{subleading\ Z}$ (right), without any cut on the distribution being plotted. The second row shows $p_T^{leading\ Z}$ (middle left) and $p_T^{subleading\ Z}$ (right) and finally the third row p_T^{ZZ} (left) and M^{ZZ} (right).

Figure B.5: Kinematic distributions for $ZZ \to \ell^-\ell^+\ell^-\ell^+$ candidates in the $e^+e^-\mu^+\mu^-$ final-state, allowing one Z to be off shell (ZZ^*selection). The top row shows $M^{leading\ Z}$ (left) and $M^{subleading\ Z}$ (right), without any cut on the distribution being plotted. The second row shows $p_T^{leading\ Z}$ (middle left) and $p_T^{subleading\ Z}$ (right) and finally the third row p_T^{ZZ} (left) and M^{ZZ} (right).

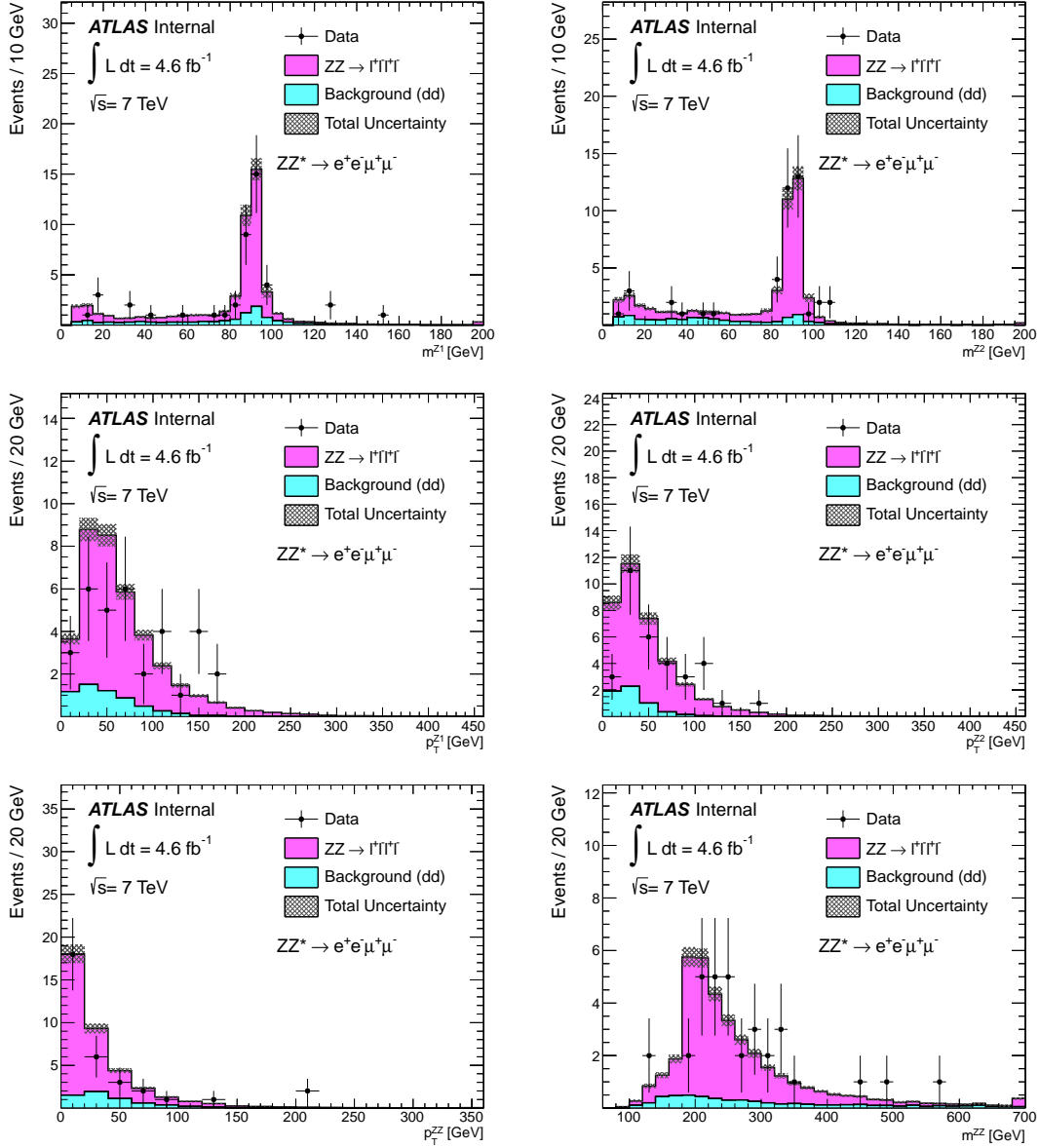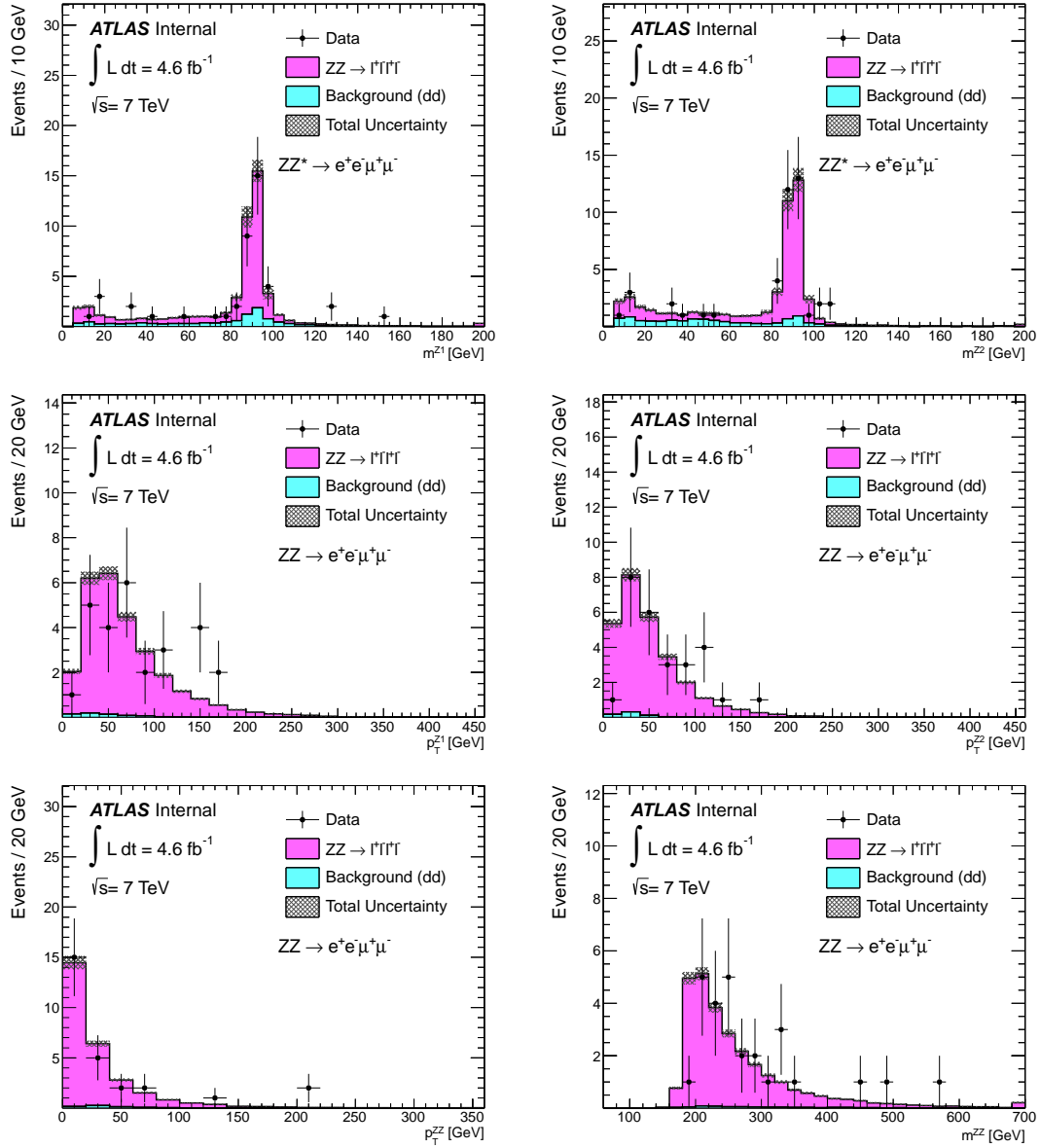**Figure B.6:** Kinematic distributions for $ZZ \to \ell^- \ell^+ \ell^- \ell^+$ candidates in the $e^+ e^- \mu^+ \mu^-$ final state, applying the on-shell (ZZ) selection. The top row shows $M^{leading\ Z}$ (left) and $M^{subleading\ Z}$ (right), without any cut on the distribution being plotted. The second row shows $p_T^{leading\ Z}$ (middle left) and $p_T^{subleading\ Z}$ (right) and finally the third row p_T^{ZZ} (left) and M^{ZZ} (right).

Appendix C

$ZZ \to \ell^-\ell^+\ell^-\ell^+$ Unfolded Distributions with Different Binning

To increase the resolution of the information the data provide in the high momentum, high mass area, the last bin of the p_T^Z and $M_{4\ell}$ distributions of Fig. 6.2 in **Chapter 6**, has been split in two bins: $[0-60, 60-100, 100-200, 200-300, > 300$ GeV$]$ $[0-240, 240-300, 300-400, 400-600, > 600$ GeV$]$ respectively. The last bin has a much bigger systematics (from PDF uncerntaity) and a lower statistics than the one just before. The result of this binning in p_T^Z and $M_{4\ell}$ are shown in Fig. C.1. Figure C.2 shows the normalized and unfolded distributions of the $ZZ \to \ell^-\ell^+\ell^-\ell^+$ channel.

(a) Unfolded p_T^Z distribution.

(b) Unfolded $M_{4\ell}$ distribution.

Figure C.1: Unfolded distributions for $ZZ \to \ell^-\ell^+\ell^-\ell^+$.

(a) Normalized and unfolded $\Delta\phi(\ell, \ell)$ distribution.

(b) Normalized and unfolded p_T^Z distribution.

(c) Normalized and unfolded m^{ZZ} distribution.

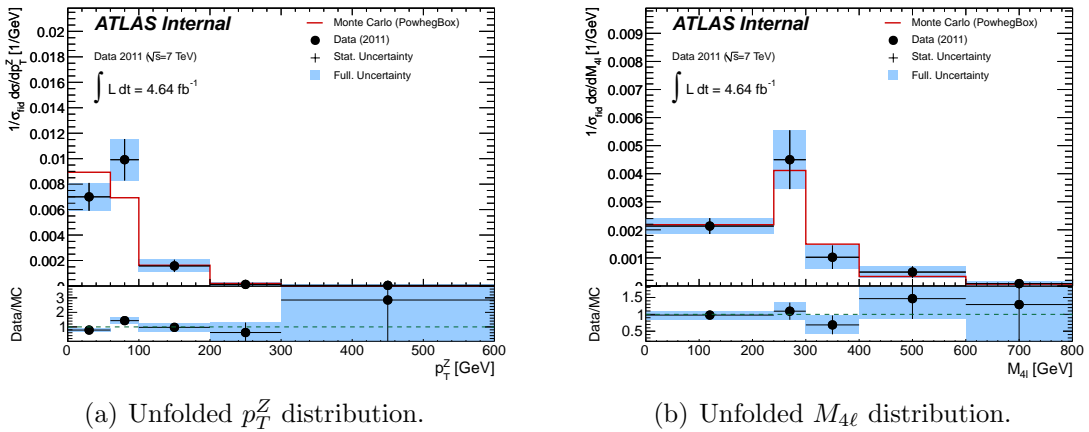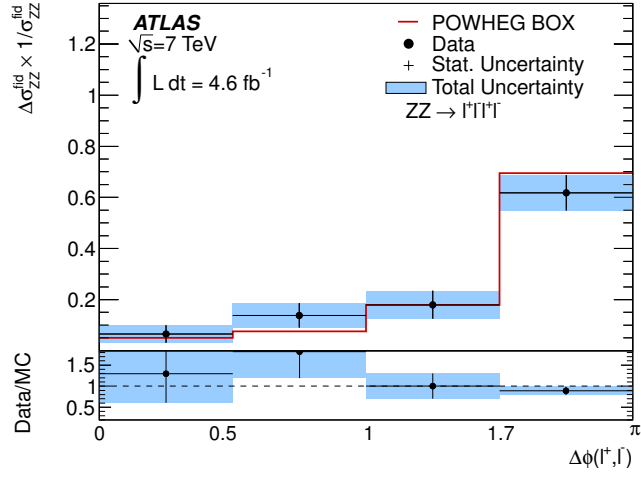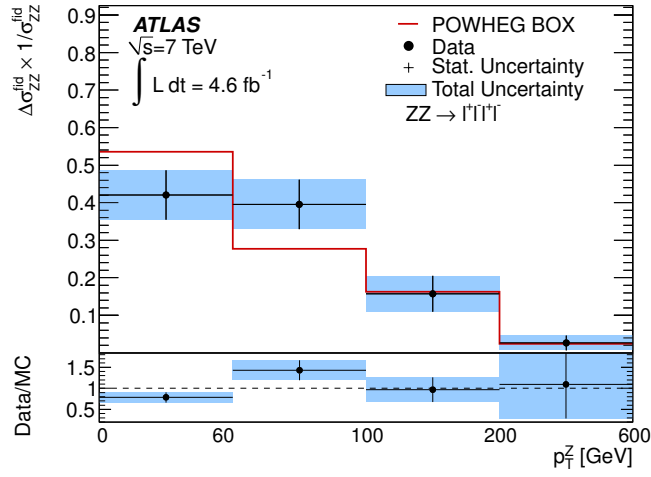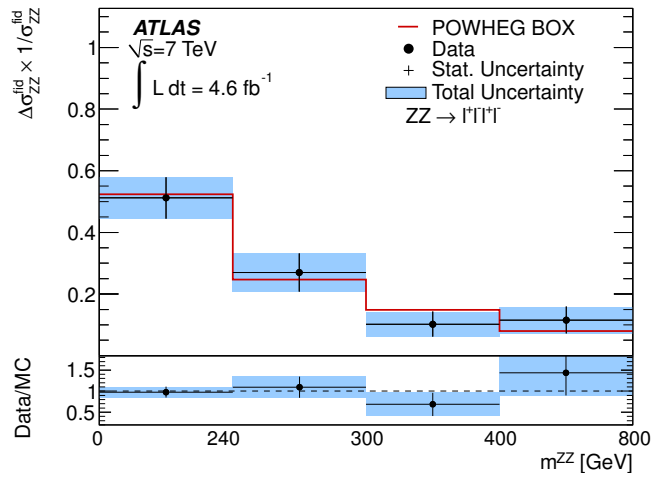**Figure C.2:** Normalized and unfolded distributions for $ZZ \to \ell^- \ell^+ \ell^- \ell^+$.

Bibliography

[1] J. Beringer et al. (Particle Data Group), Phys. Rev. D86, 010001 (2012)

[2] A. Pich. The standard model of electroweak interactions. Spires, hep-ph(0502010v1), 2007.

[3] S. F. Novaes. Standard Model: An Intoduction. IFT-P, hep-ph/0001283v1, 2000.

[4] T. Morii, C.S. Lim, S.N. MuKherjee. The Physics of the Standard Model and Beyond, 2004.

[5] M. A. T. Emmy Noether. Invariant Variation Problems. Physics/0503066, 1918.

[6] *Observation of a new particle in the search for the Standard Model Higgs boson with the ATLAS detector at the LHC* Phys. Lett. B 716 (2012) 1-29

[7] *Observation of a new boson at a mass of 125 GeV with the CMS experiment at the LHC* Phys. Lett. B 716 (2012) 30-61

[8] G.J. Gounaris, J. Layssac, F.M. Renard. *New and Standard Physics contributions to anoumalous Z and γ self-couplings* hep-ph/0003143v1 (2000).

[9] U. Baur and D. L. Rainwater, *Probing neutral gauge boson self interactions in ZZ production at hadron colliders*, Phys. Rev. D 62 (2000) 113011, [hep-ph/0011016].

[10] T. Sjostrand et al., *Pythia 6.4 physics and manual*, JHEP 0605 (2006) 026, [hep-ph/0603175].

[11] S. Alioli, P. Nason, C. Oleari and E. Re, *A general framework for implementing NLO calculations in shower Monte Carlo programs: the PowhegBox*, JHEP 1006 (2010) 043, [arXiv:1002.2581].

[12] S. Frixione and B. R. Webber, *Matching NLO QCD computations and parton shower simulations*, JHEP 0206 (2002) 029 [hep-ph/0204244].

[13] G. Corcella et al., *Herwig 6.5*, JHEP 0101 (2001) 010.

[14] J. M. Butterworth, J. R. Forshaw and M. H. Seymour, *Multiparton interactions in photoproduction at HERA*, Z. Phys. C 72 (1996) 637, [hep-ph/9601371].

[15] J. M. Campbell and R. K. Ellis, *An update on vector boson pair production at hadron colliders*, Phys. Rev. D60, 113006 (1999) [hep-ph/9905386].

[16] T. Gleisberg et al., *Event generation with Sherpa 1.1*, JHEP 0902 (2009) 007, [arXiv:0811.4622].

[17] T. Binoth, N. Kauer and P. Mertsch, *Gluon-induced QCD corrections to $pp \rightarrow ZZ \rightarrow l\bar{l}'l\bar{l}'$*, arXiv:0807.0024.

[18] H.L. Lai et al., E. Phys. J. C12, 375 (2000); J. Pumplin et al., JHEP 0207, 012 (2002); P.M. Nadolsky et al., Phys. Rev. D 78, 013004 (2008) [arXiv:0802.0007].

[19] H. L. Lai, M. Guzzi, J. Huston, Z. Li, P. M. Nadolsky, J. Pumplin and C. P. Yuan, arXiv:1007.2241 [hep-ph].

[20] A.D. Martin, W.J. Stirling, R.S. Thorne and G. Watt, Phys. Lett. B 652, 292 (2007); arXiv:0901.0002 (2009);

[21] F. D. Aaron et al. [H1 Collaboration and ZEUS Collaboration], JHEP 1001 (2010) 109 [arXiv:0911.0884 [hep-ex]].

[22] S. Alekhin, J. Blumlein, S. Klein and S. Moch, Phys. Rev. D 81, 014032 (2010) [arXiv:0908.2766 [hep-ph]].

[23] J. Ohnemus and J. F. Owens, *An Order $\alpha(s)$ calculation of hadronic ZZ production*, Phys. Rev. D43 (1991) 3626-3639.

[24] L. J. Dixon, Z. Kunszt and A. Signer, *Vector boson pair production in hadronic collisions at order $\alpha(s)$: Lepton correlations and anomalous couplings*, Phys. Rev. D60 (1999) 114037 [hep-ph/9907305].

[25] D. A. Dicus, C. Kao and W. Repko, *Gluon production of gauge bosons*, Phys.Rev. D36 (1987) 1570.

[26] J. M. Campbell, R. Keith Ellis and C. Williams, *Vector boson pair production at the LHC*, JHEP 07 (2011) 018, [arXiv:1105.0020].

[27] L3 Collaboration, M. Acciarri et al., *Study of Z Boson Pair Production in e^+e^- collisions at LEP at $\sqrt{s} = 189$ GeV*, Phys. Lett. B465 (1999) 363-375, arXiv:hep-ex/9909043.

[28] OPAL Collaboration, G. Abbiendi et al., *Study of Z pair production and anomalous couplings in e^+e^- collisions at $\sqrt{s}$ between 190 GeV and 209 GeV*, Eur. Phys. J. C32 (2003) 303-322, arXiv:hep-ex/0310013.

[29] ALEPH Collaboration, R. Barate et al., *Measurement of the $e^+e^- \to ZZ$ production cross section at centre-of-mass energies of 183 GeV and 189 GeV*, Phys. Lett. B469 (1999) 287-302, arXiv:hep-ex/9911003.

[30] DELPHI Collaboration, J. Abdallah et al., *ZZ production in e^+e^- interactions at $\sqrt{s} = 183$ GeV to 209 GeV*, Eur. Phys. J. C30 (2003) 447-466, arXiv:hep-ex/0307050.

[31] D0 Collaboration, V. M. Abazov et al., *Measurement of the ZZ production cross section in p-pbar collisions at $\sqrt{s} = 1.96$ TeV*, arXiv:1104.3078 [hep-ex].

[32] D0 Collaboration, V. M. Abazov et al., *Search for ZZ and $Z\gamma^*$ production in p-$\bar{p}$ collisions at sqrt(s) = 1.96 TeV and limits on anomalous ZZZ and $ZZ\gamma^*$ couplings*, Phys. Rev. Lett. 100 (2008) 131801, arXiv:0712.0599 [hep-ex].

[33] CDF Collaboration, T. Aaltonen et al., *First Measurement of ZZ Production in ppbar Collisions at sqrt(s)=1.96 TeV*, hep-ex/0801.4806.

[34] ATLAS Collaboration, *Measurement of the ZZ Production Cross Section and Limits on Anomalous Neutral Triple Gauge Couplings in Proton-Proton Collisions at $\sqrt{s} = 7$ TeV with the ATLAS Detector*, Phys. Rev. Lett. 108 (2012) 041804, arXiv:hep-ex/1110.5016.

[35] C. Collaboration, *Measurement of the WW, WZ and ZZ cross sections at CMS*, CMS Physics Analysis Summary CMS-PAS-EWK-11-010 , https://cdsweb.cern.ch/record/1370067.

[36] The LEP collaborations ALEPH, DELPHI, L3, OPAL, and the LEP Electroweak Working Group, *A Combination of preliminary electroweak measurements and constraints on the standard model*, hep-ex/0612034.

[37] D0 collaboration, *Search for ZZ and $Z\gamma^*$ production in $p\bar{p}$ collisions at $\sqrt{s} = 1.96$ TeV and limits on anomalous ZZZ and $ZZ\gamma^*$ couplings*, Phys. Rev. Lett. 100 (2008) 131801, [arXiv:0712.0599].

[38] CERN, LHC Design Report Volume I: The LHC Main Ring, CERN-2004-003-V-1. (2004).

[39] LEP design report. CERN-LEP, 1, 1984.

[40] ATLAS Collaboration, and G. Aad et al., *The ATLAS Experiments at the CERN Large Hadron Collider*, JINST 3:S08003 (2008).

[41] ALEPH, DELPHI, L3 and OPAL Collaboration, Phys. Lett. B565 (2003) 61.

[42] B.W.Lee at al Phys. Rev. Lett 38 (1977) 883; M.Quiros, *Constaints on the Higgs boson properties from the effective potential*, hep-ph/9703412; A. Ghinculov and T. Binothe, Acta Phys. Polon. B30 (1999) 99.

[43] The LEP Collaboration ALEPH, DELPHI, L3 and OPAL, the LEP Electroweak Working Group, the SLD Electroweak and Heavy Flavour Groups, *A combination of preliminary electroweak measurements and contraints on the Standard Model*, hep-ex/0312023; Updates numbers from the LEP Electroweak Working Groups: http://lepewwg.web.cern.ch/LEPEWWG. The LEP Collaborations ALEPH, DELPHI, L3 and OPAL, the LEP Electroweak Working Gropus, *Precision Electroweak Measurements and Constrains on the Standard Model*, arXiv:0712.0929[hep-ex], December 2007.

[44] A. Djouadi et al., Phys. rept. 457 1-216, 2008, LPT-Orsay-05-17 *The Anatomy of Electroweak Symmetry Breaking, Tome II*, aXiv:0503172[hep-ph].

[45] A. Djouadi et al., Phys. rept. 459 1-241, 2008, LPT-Orsay-05-18 *The Anatomy of Electroweak Symmetry Breaking, Tome II*, aXiv:0503173[hep-ph].

[46] See for instance: G.Altarelli, F.Feruglio and I.Masina, JHEP 0011 (2000) 040.

[47] G.R. Farrar and P.Fayet, Phys. Lett. B76 (1978) 575.

[48] J.R.Ellis, J.S.Hagelin, D.V.Nanopoulos, K.A.Olive and M.Srednicki, Nucl. Phys. B238 (1984) 453.

[49] ATLAS Collaboration. Atlas detector and physics performance : Technical Design Report, 1. (Technical Design Report ATLAS ; 14), 1999.

[50] ATLAS Collaboration. Atlas detector and physics performance : Technical Design Report, 2. (Technical Design Report ATLAS ; 15), 1999.

[51] S.van der Meer, CERN-ISR-PO-68-31, 1968.

[52] *Luminosity determination using the ATLAS detector*, ATL-ATLAS-CONF-2010-060, July 20, 2010.

[53] *Improved Luminosity Determination in pp Collisions at $\sqrt{s} = 7$ TeV using the ATLAS Detector at the LHC*, ATL-ATLAS-CONF-2012-080, July 07, 2012.

[54] ATLAS Collaboration, *ATLAS, High Level Trigger, Data Acquisition and Controls*, CERN/LHCC/2003-022, Geveva, CERN 2003.

[55] *Updated Luminosity Determination in pp Collisions at $\sqrt{s} = 7$ TeV using the ATLAS Detector*, Tech. Rep. ATLAS-CONF-2011-011, CERN, Geneva, Mar, 2011.

[56] ATLAS collaboration, *The ATLAS simulation infrastructure*, Eur. Phys. J. C 70 (2010) 823, [arXiv:1005.4568].

[57] S. Agostinelli et al., *Geant4 - a simulation Toolkit*, Nucl. Instrum. Meth. A 506 (2003) 250.

[58] M. L. Mangano et al., Alpgen, *a generator for hard multiparton processes in hadronic collisions*, JHEP 0307 (2003) [hep-ph/0206293].

[59] J. Alwall et al., *MadGraph/MadEvent v4: The new web generation*, JHEP 09 (2007) 028, [arXiv:0706.2334].

[60] *http://phys-ds.physics.lsa.umich.edu/docushare/dsweb/Get/Document-2010/g6.ps.*

[61] J. Butterworth, E. Dobson, U. Klein, B. Mellado Garcia, T. Nunnemann, J. Qian, D. Rebuzzi, R. Tanaka, *Single boson and diboson production cross sections in pp collisions at $\sqrt{s} = 7$ TeV*, ATLAS Internal Communication ATL-COM-PHYS-2010-695 (2010) .

[62] ATLAS collaboration, *Measurement of the $W \to l\nu$ and $Z/\gamma^* \to ll$ production cross sections in proton-proton collisions at $\sqrt{s} = 7$ TeV with the ATLAS detector*, JHEP 1012 (2010) 060, [arXiv:1010.2130].

[63] R. Fruhwirth, *Track fitting with non-gaussian noise*, Comput. Phys. Commun. 100 (1997), no. 1-2 1.

[64] ATLAS collaboration, *Electron performance measurements with the ATLAS detector using the 2010 LHC proton-proton collision data.* (The measurements reported here have been extended to the 2011 dataset.), Eur. Phys. J. C 72 (2012) 1909, [arXiv:1110.3174]

[65] *https://twiki.cern.ch/twiki/bin/view/AtlasProtected/ MCPAnalysisGuidelinesEPS2011.*

[66] *Search for the Standard Model Higgs boson in the decay channel $H \to ZZ^{(*)} \to 4\ell$ with 4.8 fb^{-1} of pp collisions at $\sqrt{s} = 7$ TeV,* Tech. Rep. ATL-COM-PHYS-2011-1715, CERN, Geneva, Jan-11,2012. https://cdsweb.cern.ch/record/1408784.

[67] ATLAS Collaboration, *Measurement of ZZ production in pp collisions at $\sqrt{s} = 7$ TeV and limits on anomalous ZZZ and ZZγ couplings with the ATLAS detector* CERN-PH-EP-2012-318.

[68] G. Cowan, *Statistical Data Analysis* OXFORD UNIVERSIY PRESS, 1998.

[69] V. Blobel, *An Unfolding Method For High Energy Physics Experiments,* arXiv:0208.022 [hep-ex].

[70] A. Hocker and V. Kartvelishvili, *SVD Approach to Data Unfolding,* arXiv:9509.307 [hep-ph].

[71] B. Malaescu, *An Iterative, Dynamically Stabilized Method of Data Unfolding,* arXiv:0907.3791 [physics.data-an].

[72] G. D'Agostini, *Improved Iterative Bayesian Unfolding,* arXiv:1010.0632 [physics.data-an].

[73] U. Baur, T. Han, J. Ohnemus, *WZ production at hadron colliders: Effects of non-standard WWZ couplings and QCD corrections,* Phys.Rev. D. 51 (1995) 3381, [hep-ph/9410266].

[74] U. Baur, T. Han and J. Ohnemus,*QCD corrections and anomalous couplings in Zγ production at hadron colliders,* Phys.Rev. D57 (1998) 2823, [hep-ph/9710416].

[75] G. Bella, *Weighting Diboson Monte Carlo events in hadron colliders,* arXiv:0803.3307.

[76] G. Cowan, K. Cranmer, E. Gross, and O. Vitells, *Asymptotic Formulae for Likelihood-Based Tests of New Physics,* Eur. Phys. J. C 71 (2011) 1554, arXiv:hep-ph/1007.1727v2.